

Copyright  
by  
Christine Marie Egnatuk  
2012

**The Dissertation Committee for Christine Marie Egnatuk Certifies that this is the approved version of the following dissertation:**

**Radioargon Production at The University of Texas at Austin**

**Committee:**

---

Steven R. Biegalski, Supervisor

---

Sheldon Landsberger

---

Kendra M.F. Biegalski

---

Judah Friese

---

Erich Schneider

**Radioargon Production at The University of Texas at Austin**

**by**

**Christine Marie Egnatuk, B.A., M.S.E.**

**Dissertation**

Presented to the Faculty of the Graduate School of

The University of Texas at Austin

in Partial Fulfillment

of the Requirements

for the Degree of

**Doctor of Philosophy**

**The University of Texas at Austin**

**August 2012**

## **Dedication**

For Natalie.

## **Acknowledgements**

I would like to thank a number of people that helped me complete this project. First, I wish to thank my adviser, Steve Biegalski. Thank you for providing support, knowledge, and the occasional push in the right direction. Thank you to the NETL staff for the long hours necessary to complete some of the experimental work and for help correcting my mistakes when things took a wrong turn. I would also like to thank Tony Day at PNNL for walking me through the Swagelok catalog and helping build my first gas transfer system.

I am grateful for my funding through the Nuclear Nonproliferation International Safeguards Graduate Fellowship Program sponsored by the Department of Energy and the National Nuclear Security Administration.

Lastly, I would like to thank my family and friends for providing support, understanding, and cookies. The encouraging texts and e-mails during the hard times and the happy phone calls during the good times made my transition back to student life seamless.

## Radioargon Production at The University of Texas at Austin

Christine Marie Egnatuk, degree sought Ph.D.

The University of Texas at Austin, 2012

Supervisor: Steven R. Biegalski

The interest in the detection of radioargon isotopes— $^{37}\text{Ar}$ ,  $^{39}\text{Ar}$ , and  $^{42}\text{Ar}$ —is increasing important for on-site inspections within the Comprehensive Nuclear-Test-Ban Treaty verification regime. In an underground nuclear explosion  $^{37}\text{Ar}$  is produced by  $^{40}\text{Ca}(n,\alpha)^{37}\text{Ar}$  reaction in surrounding soil and rock. With a half-life of 35 days,  $^{37}\text{Ar}$  provides a signal useful for confirming the location of an underground nuclear event. The development of detector systems is underway. This work produced radioargon isotopes by three methods for the development and testing of radioargon detection systems.

The irradiation of argon gas at natural enrichment in the 3L facility within the Mark II TRIGA reactor facility at The University of Texas at Austin provides a source of  $^{37}\text{Ar}$  for the calibration of the ULBPC in development at PNNL. The  $^{41}\text{Ar}$  activity is measured by the gamma activity using an HPGe detector after the sample is removed from the core. Using the  $^{41}\text{Ar}/^{37}\text{Ar}$  production ratio and the  $^{41}\text{Ar}$  activity, the amount of  $^{37}\text{Ar}$  created is calculated. The  $^{41}\text{Ar}$  decays quickly (half-life of 109.34 minutes) leaving a radioactive sample of high purity  $^{37}\text{Ar}$  and only trace levels of  $^{39}\text{Ar}$ .

The second method was the irradiation of a calcium-containing compound. This option is not the best match for the TRIGA reactor type due to the thermal neutron flux. Therefore, the use of the Cd-lined 3L irradiation canister minimized the thermal activation of impurities while still allowing the majority of the  $^{40}\text{Ca}(n,\alpha)^{37}\text{Ar}$  reactions occur.

The third and last irradiation technique was a large volume, in-core gas facility developed at The University of Texas at Austin MARK II TRIGA reactor to produce a sample of  $^{42}\text{Ar}$  with an activity above 1 mBq. The method requires a large volume, 1.4 L, of natural argon gas (99.6003%  $^{40}\text{Ar}$ ) at about 1 atm and three-12 hour irradiation periods. The production of  $^{42}\text{Ar}$  requires a double capture to be produced from the stable  $^{40}\text{Ar}$  isotope. This method produced 940 kBq of  $^{39}\text{Ar}$ , 3.08 MBq  $^{37}\text{Ar}$ , 114 GBq  $^{41}\text{Ar}$ , and 0.311 Bq  $^{42}\text{Ar}$  at the end of the final irradiation period.

## Table of Contents

List of Tables .....	xi
List of Figures .....	xiii
<b>CHAPTER 1: INTRODUCTION .....</b>	<b>1</b>
1.1 Background .....	4
1.2 Literature Review .....	15
1.2.1 Calibration of ULBPC .....	16
1.2.2 Production of $^{37}\text{Ar}$ by irradiation of calcium-containing compounds .....	17
1.2.3 Detection of radioargon isotopes .....	18
1.2.4 Radioargon Dating .....	19
1.2.5 Applications .....	20
<b>CHAPTER 2: THEORY .....</b>	<b>22</b>
2.1 Radioargon Production in Nuclear Explosions .....	22
2.2 Activation and Decay .....	28
2.3 Radioargon Production in Reactor Facility .....	31
2.3.1 Production of $^{37}\text{Ar}$ .....	31
2.3.1.1 Irradiation of natural argon .....	31
2.3.1.2 Irradiation of calcium .....	33
2.4 Production of Radioargon in a Reactor .....	39
2.4.1 Decay of $^{42}\text{K}$ and $^{42}\text{Ar}$ .....	43
2.4.2 Other Methods of $^{42}\text{K}$ production .....	44

2.5 Argon cross-sections .....	45
<b>CHAPTER 3: REACTOR MODEL.....</b>	<b>51</b>
3.1 MCNPX .....	53
3.2 Characterization of the 3L irradiation facility .....	56
3.2.1 Co-Al wires.....	56
3.3 Modeled Production Experiments.....	58
<b>CHAPTER 4: <sup>37</sup>AR PRODUCTION.....</b>	<b>59</b>
4.1 Irradiation of Natural Argon .....	59
4.1.1 Experimental set-up .....	61
4.1.2 Procedure .....	66
4.1.3 Results.....	69
4.2 Irradiation of calcium-containing compounds .....	72
4.2.1 Experimental set-up .....	75
4.2.2 Method .....	77
4.2.3 Procedure .....	78
4.2.4 Production.....	79
4.2.5 Results.....	82

<b>CHAPTER 5: LARGE VOLUME IRRADIATION PROCEDURE.....</b>	<b>85</b>
5.1 Experimental Set-up.....	86
5.2 Procedure .....	96
5.3 Model .....	102
5.4 Production Possibilities.....	105
<b>CHAPTER 6: CONCLUSION .....</b>	<b>109</b>
<b>Appendix A: Double-Ended Shipping Cylinder .....</b>	<b>113</b>
<b>APPENDIX B: KNF 4-STAGE TRANSFER PUMP .....</b>	<b>114</b>
<b>APPENDIX C: CHECK VALVE.....</b>	<b>117</b>
<b>APPENDIX D: UT TRIGA MCNPX REACTOR MODEL .....</b>	<b>118</b>
<b>REFERENCES.....</b>	<b>141</b>

**VITA 145**

## List of Tables

Table 1.1. Noble gas and volatile radionuclides with potential interest for OSI inspections (atom.kaeri.kr).....	6
Table 1.2. The composition of the gas by percent volume after being removed from the CaO sample container (Abdurashitov <i>et al.</i> , 2006).....	18
Table 1.3. $^{37}\text{Ar}$ decay modes and released energy (Barsanov <i>et al.</i> , 2006). ....	19
Table 2.1. Activities of $^{37}\text{Ar}$ in Ci/kT resulting from source term calculation in various surrounding soil and rock concentrations (Lowrey, 2010, Egnatuk <i>et al.</i> , 2011).....	25
Table 2.2. The natural abundance of argon isotopes (Rosman & Taylor, 1997) and their thermal radiative capture cross-sections (Mughabghab <i>et al.</i> , 1981). ....	32
Table 2.3. Gamma-rays emitted during the beta decay of $^{42}\text{K}$ .....	44
Table 3.1. The irradiation of SRM 953 samples at different power levels. Each sample was counted for a live time of 43,200 seconds within a few days of irradiation.....	57
Table 4.1. The gas transfer system components labeled as indicated in the legend of Figure 4.5. 0 indicated off or closed. 1 indicated on or open. ....	69
Table 4.2. The percent abundance of calcium isotopes in naturally occurring Ca.	73
Table 4.3. The advantages and disadvantages of using the different calcium-containing compounds. ....	74
Table 4.4. CaO counting time. ....	80
Table 4.5. Calcium cross-sections used to estimate the $^{39}\text{Ar}$ and $^{37}\text{Ar}$ production activities. ....	83

Table 4.6. The estimated activities and the modeled activities in Bq.....	84
Table 5.1. The valve settings for each action with 0 indicating closed and 1 indicating open. For Ar (argon gas), TP (transfer pump) and V (vacuum), 0 means off and 1 means on.....	101
Table 5.2. The collapsed cross-section generated by the volume tally of the 1.4 L within the lead-lined 3L canister.....	103
Table 5.3. Comparison of radioargon activities in Bq throughout the irradiation and decay process. ....	105

## List of Figures

Figure 1.1. Radionuclide transport after an underground nuclear event.....	3
Figure 1.2. The measured anthropogenic $^{37}\text{Ar}$ activities in soils for different locations in Switzerland, France, Germany, and USA (Riedmann and Purtschert, 2011). .....	8
Figure 1.3. The naturally induced $^{37}\text{Ar}$ activity as a function of depth in the soil in Switzerland (47.26°N, 8.39° E, 570 m above sea level) with a 1.45% calcium-concentration in the soil (Purtschert & Riedmann, 2011).....	9
Figure 1.4. Switzerland data extrapolation of $^{37}\text{Ar}$ activity on a global scale at a 70 cm depth (Purtschert & Riedmann, 2011). .....	10
Figure 1.5. $^{37}\text{Ar}$ activity concentrations 72 hours after the March 2010 HFIR release (Fay & Biegalski, 2012).....	11
Figure 1.6. The noble gas activity at the surface after a 1 kT underground nuclear test (Haas <i>et al.</i> , 2010).....	12
Figure 1.7. The radioxenon and radioargon activities at the surface versus the days post-event (Carrigan, 2009). .....	13
Figure 1.8. The activity expected at the surface 80 days after a normalized 1 kT nuclear subsurface detonation in various rock types (Haas <i>et al.</i> , 2009). .....	14
Figure 1.9. ULBPC energy spectra (Aalseth <i>et al.</i> , 2010).....	16
Figure 2.1. The activation and decay of a radionuclide.....	28
Figure 2.2. The radiative capture cross-section of $^{36}\text{Ar}$ versus the energy of the incident neutron (Santamarina <i>et al.</i> , 2009).....	33

Figure 2.3. The (n, $\alpha$ ) cross-section for $^{40}\text{Ca}$ (Chadwick <i>et al.</i> , 2006; Chadwick <i>et al.</i> , 2011; Koning <i>et al.</i> , 2006; Shibata <i>et al.</i> , 2002; Shibata <i>et al.</i> , 2011; Zabrodskaya <i>et al.</i> , 2007).....	34
Figure 2.4. The $^{40}\text{Ca}(n,\alpha)^{37}\text{Ar}$ reaction cross-section data used by Riedmann and Purtschert (2011).....	35
Figure 2.5. The $^{42}\text{Ca}(n,\alpha)^{39}\text{Ar}$ reaction cross-sections (Chadwick <i>et al.</i> , 2006; Chadwick <i>et al.</i> , 2011; Koning <i>et al.</i> , 2006; Shibata <i>et al.</i> , 2002; Shibata <i>et al.</i> , 2011; Zabrodskaya <i>et al.</i> , 2007). ....	36
Figure 2.6. The $^{42}\text{Ca}(n,p)^{42}\text{K}$ reaction cross-sections (Chadwick <i>et al.</i> , 2006; Chadwick <i>et al.</i> , 2011; Koning <i>et al.</i> , 2006; Shibata <i>et al.</i> , 2002; Shibata <i>et al.</i> , 2011; Zabrodskaya <i>et al.</i> , 2007). ....	37
Figure 2.7. $^{43}\text{Ca}(n,p)^{43}\text{K}$ reaction cross-sections (Chadwick <i>et al.</i> , 2006; Chadwick <i>et al.</i> , 2011; Koning <i>et al.</i> , 2006; Shibata <i>et al.</i> , 2002; Shibata <i>et al.</i> , 2011; Zabrodskaya <i>et al.</i> , 2007).....	38
Figure 2.8. $^{46}\text{Ca}(n,\gamma)^{47}\text{Ca}$ reaction cross-section(Chadwick <i>et al.</i> , 2006; Chadwick <i>et al.</i> , 2011; Koning <i>et al.</i> , 2006; Shibata <i>et al.</i> , 2002; Shibata <i>et al.</i> , 2011; Zabrodskaya <i>et al.</i> , 2007).....	39
Figure 2.9. Radiative capture cross-section versus incident neutron energy for $^{41}\text{K}$ (Santamarina <i>et al.</i> , 2009).....	45
Figure 2.10. $^{36}\text{Ar}$ cross-sections from JEFF 3.1 (Koning <i>et al.</i> , 2006).....	46
Figure 2.11. JEFF 3.1 $^{37}\text{Ar}$ cross-sections (Koning <i>et al.</i> , 2006).....	47
Figure 2.12. JEFF $^{38}\text{Ar}$ cross-sections (Koning <i>et al.</i> , 2006).....	47
Figure 2.13. JEFF 3.1 $^{39}\text{Ar}$ cross-sections (Koning <i>et al.</i> , 2006).....	48
Figure 2.14. JEFF 3.1 $^{40}\text{Ar}$ cross-sections (Koning <i>et al.</i> , 2006).....	48

Figure 2.15. $^{41}\text{Ar}$ cross-section libraries. The first three are JEFF 3.1 (Koning <i>et al.</i> , 2006) and the last is from CINDER90.....	49
Figure 2.16. JEFF 3.1 $^{42}\text{Ar}$ cross-sections (Koning <i>et al.</i> , 2006).....	50
Figure 3.1. The University of Texas at Austin 1.1 MW TRIGA Mark II research reactor core during a pulse.....	51
Figure 3.2. The MARK II TRIGA reactor MCNPX model shown from above. The 3L irradiation facility used in this experiment is indicated.....	53
Figure 3.3. The flux profile of five different positions generated by the MCNPX model of the TRIGA core. ....	55
Figure 3.4. The 2200 m/s neutron flux in the lead-lined 3L. ....	57
Figure 4.1. Swagelok 43 series PFA Teflon plug valve. ....	62
Figure 4.2. Gas manifold used to transfer argon for small volume irradiation experiments.....	63
Figure 4.3. The diaphragm valve attached to the scientific grade natural argon gas canister. ....	64
Figure 4.4. The aluminum 3L irradiation canister. ....	64
Figure 4.5. The schematic of the gas transfer system for this experiment with numbered and labeled components.....	68
Figure 4.6. The $^{41}\text{Ar}$ to $^{37}\text{Ar}$ production ratio based on irradiation time. ....	70
Figure 4.7. The $^{41}\text{Ar}$ to $^{39}\text{Ar}$ production ratio based on irradiation time. ....	70
Figure 4.8. The $^{41}\text{Ar}$ to $^{42}\text{Ar}$ production ratio based on irradiation time. ....	71
Figure 4.9. The exposure rate due to the $^{41}\text{Ar}$ .....	72
Figure 4.10. The activity induced of isotopes of interest at different time steps assuming a position in the Cd-lined 3L facility at 500 kW. ....	75

Figure 4.11. The quartz ampoule filled with 2.0 g CaO is shown in the bottom picture. The ampoule and the placement of the neutron density flux monitoring wire is shown in the top picture. ....	76
Figure 4.12. The aluminum foil wrapped around the sample to ease the removal of the sample from the narrow 3L aluminum canister. ....	77
Figure 4.13. The positioning of the quartz ampoule after irradiation. The neutron density flux monitoring wire has been removed. ....	78
Figure 4.14. CaO spectra. ....	81
Figure 4.15. A longer count of the CaO sample after a longer decay period. ....	82
Figure 5.1. Gas Transfer System. ....	88
Figure 5.2. Swagelok diaphragm valves with double-sided female VCR fittings. ....	89
Figure 5.3. 3L irradiation canister made of 6061 aluminium with a lead liner for additional weight. ....	90
Figure 5.4. The top of the 3L irradiation canister. The two green Swagelok bellows valves are shown. The connection to the check valve is open during irradiation and filling, but closed while the vacuum or the transfer pump is on. The valve that connects to the transfer system is closed during irradiation and sealed with a small metal piece. ....	91
Figure 5.5. The exposure rate of the 6061 aluminum canister after three 12 hour irradiation periods separated by a 12 hour cooling period and an 84 hour decay period after the final irradiation. ....	93
Figure 5.6. The exposure rate from the lead liner post-irradiation. ....	94
Figure 5.7. Swagelok double-ended cylinder. ....	94
Figure 5.8. The connection from the Swagelok shipping cylinder to the transfer system. ....	95

Figure 5.9. Large volume gas transfer system schematic with each valve labeled.	100
Figure 5.10. The activity of the radioargon isotopes through the irradiation and decay periods.....	104
Figure 5.11. $^{37}\text{Ar}$ activity with 1.4L of enriched $^{36}\text{Ar}$ irradiated at 950 kW.....	106
Figure 5.12. The activation curve of $^{38}\text{Ar}(n,\gamma)^{39}\text{Ar}$ .....	106
Figure 5.13. The activity curve of $^{127}\text{Xe}$ .....	107
Figure 5.14. The $^{126}\text{Xe}(n,\gamma)^{127}\text{Xe}$ reaction cross-sections (Chadwick <i>et al.</i> , 2006; Chadwick <i>et al.</i> , 2011; Koning <i>et al.</i> , 2006; Shibata <i>et al.</i> , 2002; Shibata <i>et al.</i> , 2011; Zabrodszkaya <i>et al.</i> , 2007). .....	108

## CHAPTER 1: INTRODUCTION

As new countries move into the nuclear arms arena, the need for verifiable techniques for detecting clandestine nuclear activities is increasing. These techniques require differentiating between increasingly prevalent commercial nuclear activities and clandestine nuclear operations, which might include underground nuclear testing and explosions. At the forefront of global efforts to detect and discourage clandestine nuclear operations is the Comprehensive Nuclear Test-Ban Treaty (CTBT) Organization (Comprehensive 1996). Within the CTBT, a global network of monitoring stations situated in 123 countries around the world monitors for clandestine nuclear operations using various techniques. These stations have recently been used to analyze the release of nuclear materials following the Fukushima-Daiichi disaster, in which an earthquake off the coast of Japan created tsunami waves that disrupted the power supply for cooling the reactors (Stoehlker *et al.*, 2011).

The Comprehensive Nuclear-Test-Ban Treaty is an international agreement signed 183 nuclear-capable countries. The treaty will go into force when 44 designated nuclear-capable countries sign and ratify the treaty. India, Pakistan and North Korea are designated countries have yet to sign the treaty. .

The CTBT provides for On-Site Inspections (OSI) of suspected nuclear activity locations at the request of a member state. Within 96 hours of an inspection request, member countries are required to vote on the inspection request, and the OSI will only be allowed to proceed upon an affirmative vote of 30 or more member countries out of the 51 member states. An OSI is limited to searching an area no greater than 1,000 square

kilometers, and the country in question can exclude certain locations within the designated area.

Various techniques will be used in an OSI, including radionuclide monitoring techniques. Due to the radionuclides instability and decay according to half-lives, it is preferable to be able to consider radionuclides with longer half-lives. In addition, it is preferable to be able to consider radionuclides that have the ability to travel away from where they are created, due to the limited area covered by an OSI.

The use of radionuclide monitoring for nuclear event analysis is not new. Noble gases are often used due to their inert properties, and because they have been known to escape an underground cavity as shown in Figure 1.1. The radioactive noble gases are able to travel a great distance through the atmosphere (Bowyer *et al.*, 2002). Currently the predominant noble gas used for nuclear event analysis is radioxenon. The longest radioxenon isotope of interest is  $^{131m}\text{Xe}$ , which has an 11.934 day half-life. Other volatile radionuclides and noble gas radioisotopes are being proposed to help lengthen the period of time which a successful OSI can be conducted.

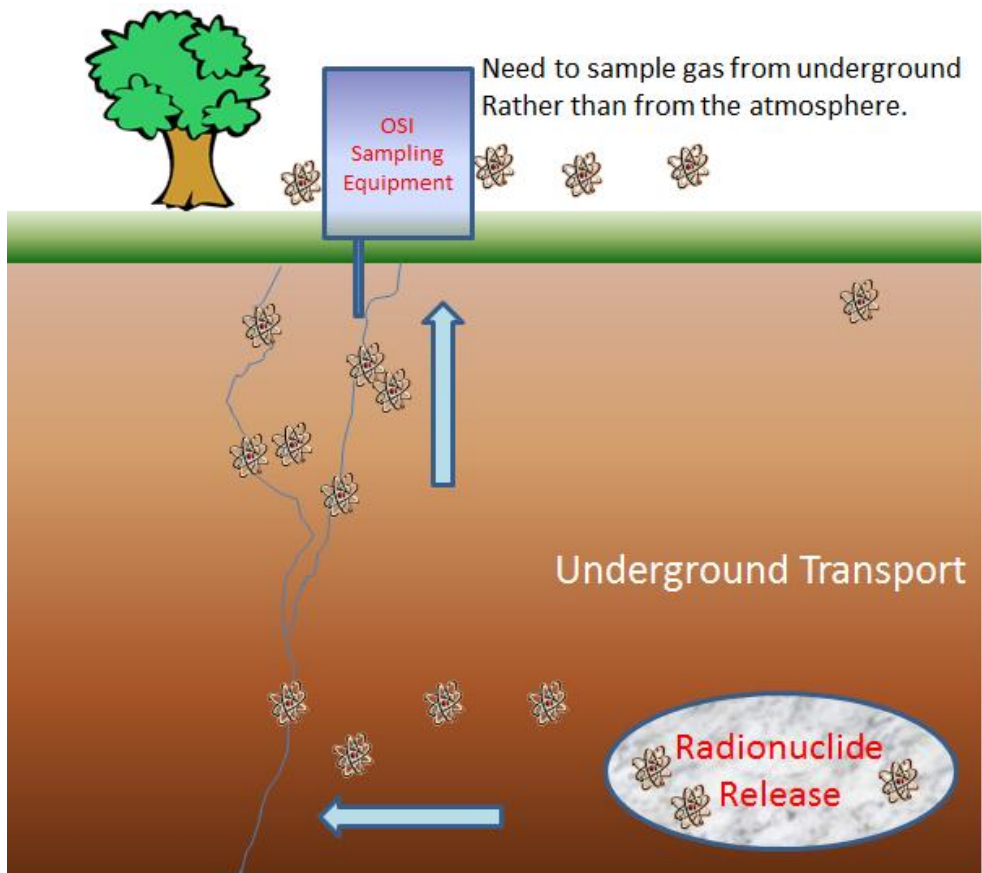


Figure 1.1. Radionuclide transport after an underground nuclear event.

Radioargon, specifically  $^{37}\text{Ar}$ , has been proposed as an addition to the list of radionuclides being monitored. The predominant production pathway for radioargon in an underground nuclear test is the activation of calcium in the soil. Naturally occurring calcium is 96.941%  $^{40}\text{Ca}$ . The  $(n,\alpha)$  reaction with  $^{40}\text{Ca}$  in soil produces  $^{37}\text{Ar}$ , which has a 35 day half-life.

This work aims to produce radioargon samples through the irradiation of natural argon gas and calcium-containing compounds. This experimental process was also modeled using MCNPX, a Monte Carlo nuclear transport code. The radioargon samples produced will be used to calibrate detectors designed to be used in association with

testing conducted as part of the enforcement of the CTBT. The production of other radionuclides with the developed techniques will also be examined.

## **1.1 Background**

Article IV of the CTBT covers the duties of the global verification regime to monitor the international community for compliance with the treaty. The verification regime is required to detect any nuclear explosions performed underground, underwater or in the atmosphere. There are six parts to the verification regime: International Monitoring System, International Data Centre, Global Communications Infrastructure, Consultation and Clarification, On-Site Inspections, and Confidence-building measures. Member states have the right to request an on-site inspection if they suspect there has been a nuclear incident, and the accused state cannot refuse the inspection. The search area is limited to 1,000 square kilometers. Because of this area limit, monitoring the air for noble gases and volatile radionuclides increases the likelihood that a nuclear event outside of the limited search area will be detected.

As the protocol for the OSI is being developed, the radionuclides that could readily escape an underground testing cavity are being considered as possible radionuclides of interest. Carrigan and Sun (2011) estimate that the earliest an OSI team would be in place is 10 days post-event. Therefore, the vented volatile radionuclides and gases would have dispersed. The path from an explosion cavity to the surface would be barometric pumping.

The current list of radionuclides of interest and their production pathways are shown in Table 1.1. The list excludes radionuclides with half-lives under 9 hours due to

the improbability of the OSI team being allowed into the region within the necessary time frame for detection. Of the nuclides on the list, the radioargon isotopes are the only non-fission products listed. Radioargon production pathways produce significantly different signatures for underground nuclear activation than for legitimate above-ground nuclear operations.

Table 1.1. Noble gas and volatile radionuclides with potential interest for OSI inspections (atom.kaeri.kr).

Isotope	Half-Life	<sup>239</sup> Pu Cumulative 1.0 MeV Fission Yield	Notes
<sup>125</sup> Xe	16.9 hours	2.36254E-18	Primarily created through <sup>124</sup> Xe(n,γ) <sup>125</sup> Xe reaction.
<sup>127</sup> Xe	36.4 days	2.91088E-14	Primarily created through <sup>126</sup> Xe(n,γ) <sup>127</sup> Xe reaction.
<sup>129m</sup> Xe	8.88 days	2.02573E-10	Primarily created through <sup>128</sup> Xe(n,γ) <sup>129m</sup> Xe reaction.
<sup>131m</sup> Xe	11.934 days	4.26083E-04	Longest lived radioxenon with good fission yield.
<sup>133m</sup> Xe	5.243 days	2.40920E-03	
<sup>133</sup> Xe	2.19 days	6.89019E-02	
<sup>135</sup> Xe	9.14 hours	7.43123E-02	
<sup>85</sup> Kr	3934.4 days	1.28871E-03	Hard to detect via classic gamma-ray spectroscopy. Documented environmental background.
<sup>37</sup> Ar	35.04 days	n/a	Produced primarily through <sup>40</sup> Ca(n,α) <sup>47</sup> Ar with secondary production through <sup>36</sup> Ar(n,γ) <sup>37</sup> Ar reaction.
<sup>39</sup> Ar	269 years	n/a	Produced primarily through <sup>38</sup> Ar(n,γ) <sup>39</sup> Ar with secondary production through <sup>42</sup> Ca(n,α) <sup>49</sup> Ar reaction.
<sup>42</sup> Ar	32.9 years	n/a	Produced from double neutron capture <sup>40</sup> Ar(n,γ) <sup>41</sup> Ar(n,γ) <sup>42</sup> Ar with secondary production from <sup>44</sup> Ca(n,γ) <sup>45</sup> Ca (n,α) <sup>42</sup> Ar. Low anticipated production.
<sup>131</sup> I	8.0270 days	3.86972E-02	Decays to <sup>131m</sup> Xe and <sup>131</sup> Xe (stable).
<sup>133</sup> I	20.8 hours	6.83020E-02	Decays to <sup>133m</sup> Xe and <sup>133</sup> Xe (stable).
<sup>134</sup> Cs	2.0648 years	1.01231E-05	Shielded radionuclide (no radioactive parent).
<sup>136</sup> Cs	13.16 d	1.28809E-03	Shielded radionuclide (no radioactive parent).
<sup>137</sup> Cs	30.07 years	6.50494E-02	High environmental background due to past fallout and reactor accidents.

The various radioargon production pathways, including anthropogenic, research, and commercial, must be considered before their use in nuclear event analysis can be fully exploited. Anthropogenic radioargon is produced through the activation of soil and air in the atmosphere and lithosphere through the induced cosmic ray neutron flux. Research reactors (Fay & Biegalski, 2012), beam line work, commercial nuclear power plants, and medical isotope production facilities will also contribute to the activation of the argon in the air.

In addition, a radioargon background map must be developed in order to identify inappropriate deviations. One of the first steps to develop a radioargon background map is the natural production rate of radioargon induced through the activation by the induced cosmic ray neutron flux. The naturally occurring  $^{37}\text{Ar}$  activities have been measured at differing altitudes, soil depths, and calcium soil concentrations (Riedmann & Purtschert, 2011). Radioargon concentration is based on the decreased production rate from cosmic ray neutrons with increased depth, radioactive decay, and diffusive transport of the radionuclide into the surrounding air. The data for various locations are shown in Figure 1.2. The measurements were between  $<3.2$  to  $120 \text{ mBq m}^{-3}$  air with minimum detection activities (MDA) of  $0.6$  -  $29.0 \text{ mBq m}^{-3}$  air.

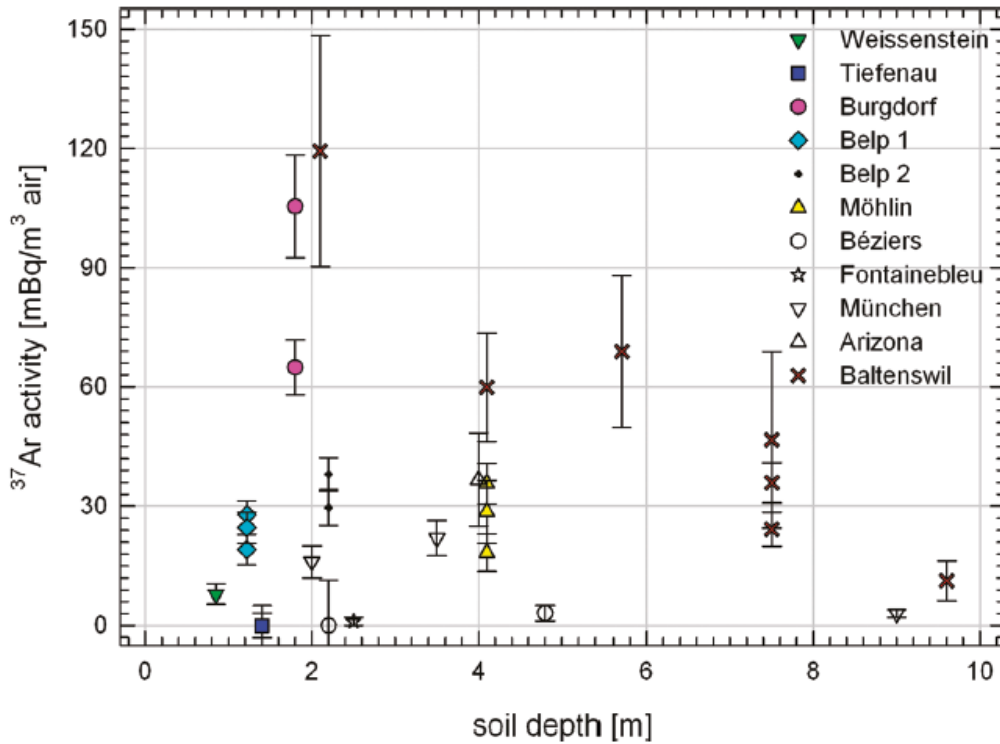


Figure 1.2. The measured anthropogenic <sup>37</sup>Ar activities in soils for different locations in Switzerland, France, Germany, and USA (Riedmann and Purtschert, 2011).

With differing latitudes and calcium composition in the soil materials, a global radioargon background will need to be considered. The anthropogenic <sup>37</sup>Ar activities as a function of depth in Switzerland are shown in Figure 1.3 (Riedmann & Purtschert, 2011). The highest induced activities are approximately 2 times higher than present in the atmosphere; the highest activities for <sup>37</sup>Ar are located in the soil at depths of 1.5 m to 2.5 m. Carrigan and Sun (2011) ran a simulation with the soil-gas and atmospheric-gas exchange. Barometric pumping skews the parabolic shape and will decrease the <sup>37</sup>Ar activity concentrations at the peak activity within the soil. This will mean the peak <sup>37</sup>Ar

background will be smaller than predicted by Riedmann and Purtschert (2011) during OSI sampling.

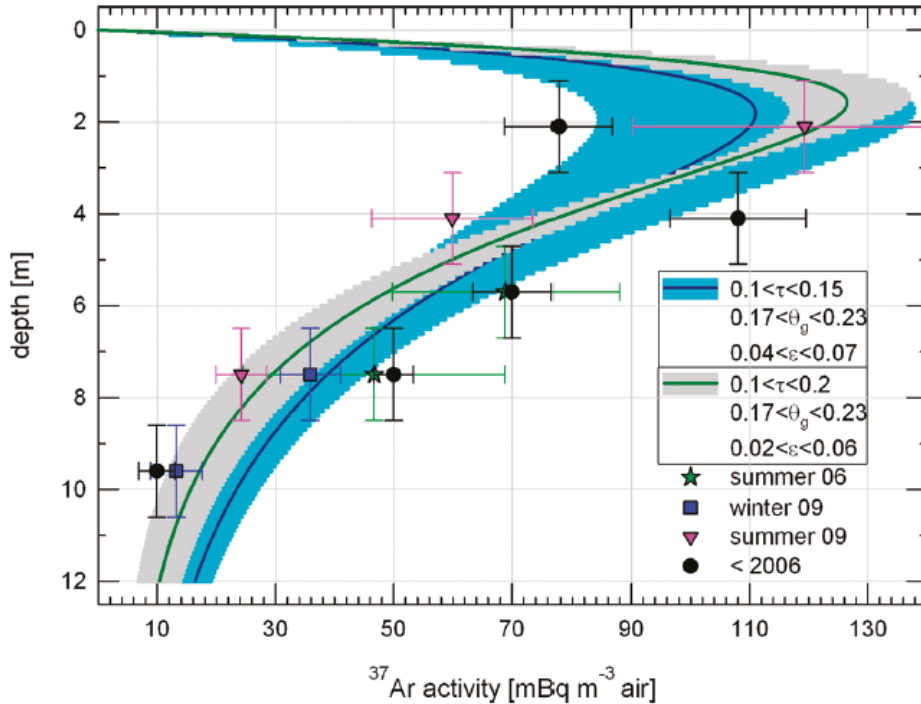


Figure 1.3. The naturally induced  $^{37}\text{Ar}$  activity as a function of depth in the soil in Switzerland ( $47.26^\circ\text{N}$ ,  $8.39^\circ\text{E}$ , 570 m above sea level) with a 1.45% calcium-concentration in the soil (Purtschert & Riedmann, 2011).

The estimated  $^{37}\text{Ar}$  at small soil depths around the world, shown in Figure 1.4, has been normalized based on the Purtschert and Riedmann (2011) data, shown in Figure 1.3. The data extrapolation considered the calcium concentration in the soil, the global coordinates, and the altitude. The highest  $^{37}\text{Ar}$  activities are calculated to be between the  $30^\circ$  to  $60^\circ$  latitude in the northern hemisphere and  $20^\circ$  to  $40^\circ$  latitude in the southern hemisphere (Purtschert & Riedmann, 2011).

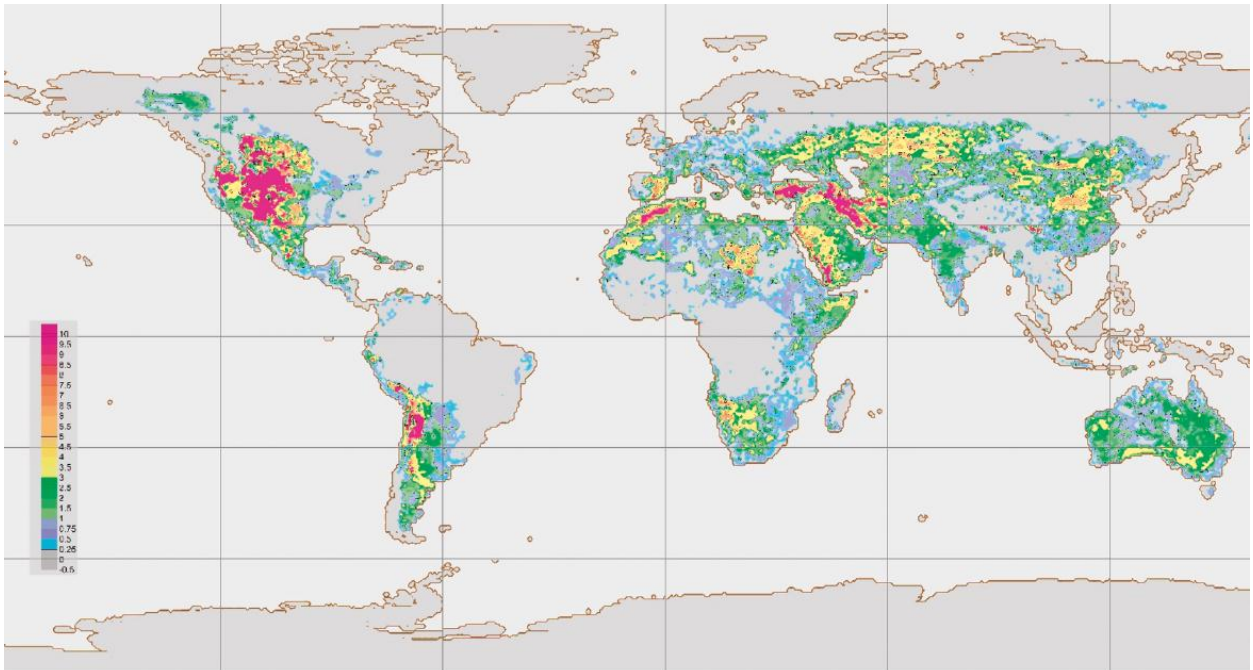


Figure 1.4. Switzerland data extrapolation of  $^{37}\text{Ar}$  activity on a global scale at a 70 cm depth (Purtschert & Riedmann, 2011).

The radioargon releases from a reactor facility could point in the direction of a clandestine nuclear operation. Long-term radioargon monitoring could also provide information about the reactor operating schedule. Since the majority of natural occurring argon is  $^{40}\text{Ar}$ , the  $^{41}\text{Ar}$ , in addition to  $^{37}\text{Ar}$ , monitoring could be useful.

The  $^{37}\text{Ar}$  released during the legitimate operation of commercial nuclear power reactors, research reactors, and beam line work must also be established. The released activity of  $^{37}\text{Ar}$  from the High Flux Isotope Reactor (HFIR) of the  $^{41}\text{Ar}/^{37}\text{Ar}$  production ratio based on the flux profile of the reactor was calculated to be approximately  $1.86 \times 10^{10} \text{Bq y}^{-1}$  (Fay & Biegalski, 2012). The transport of the  $^{37}\text{Ar}$ , shown in Figure 1.5, shows concentrations of  $0.1 \text{mBq m}^{-3}$  within tens of km from the reactor, which is far below the current detection limits and below the proposed laboratory detection system

(Aalseth *et al.*, 2011). Fay and Biegalski found that the release ratio was sensitive to decay time (2012).

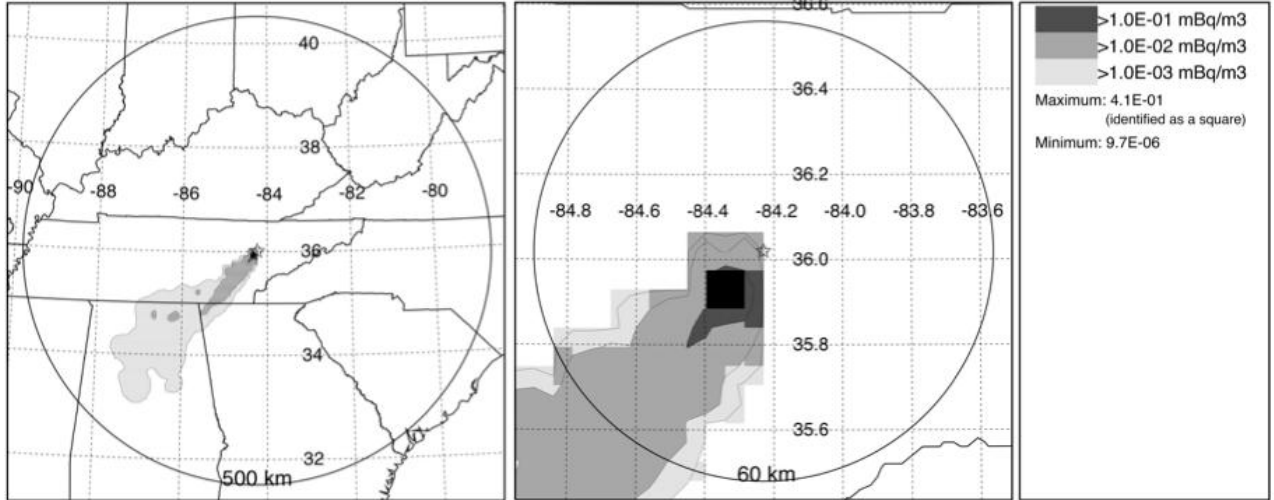


Figure 1.5.  $^{37}\text{Ar}$  activity concentrations 72 hours after the March 2010 HFIR release (Fay & Biegalski, 2012).

The OSI start is expected to be approximately 10 days or more after an initial event (Carrigan & Sun, 2011). The OSI team of researchers will assume the cavity-pressure induced seepage and vented debris and gases will be minimal or nonexistent. Therefore, the incorporation of testing for radioargon isotopes in the inspection process will help allow for a longer inspection window. Radioxenon, specifically  $^{133}\text{Xe}$  and  $^{131\text{m}}\text{Xe}$ , are used in conjunction with the SAUNA system, which has a detection limit of 2 mBq/SCM. The  $^{37}\text{Ar}$  signal is stronger than the radioxenon over fifty days after the initial underground nuclear test explosion (Aalseth *et al.*, 2010). As shown in Figure 1.6, the  $^{37}\text{Ar}$  signal will be detectable with a field detection system up to a year after a 1 kt nuclear event even in soil with a low percentage of calcium with the proposed detection limit of an  $^{37}\text{Ar}$  field system of 20 mBq/SCM (Haas *et al.*, 2010).

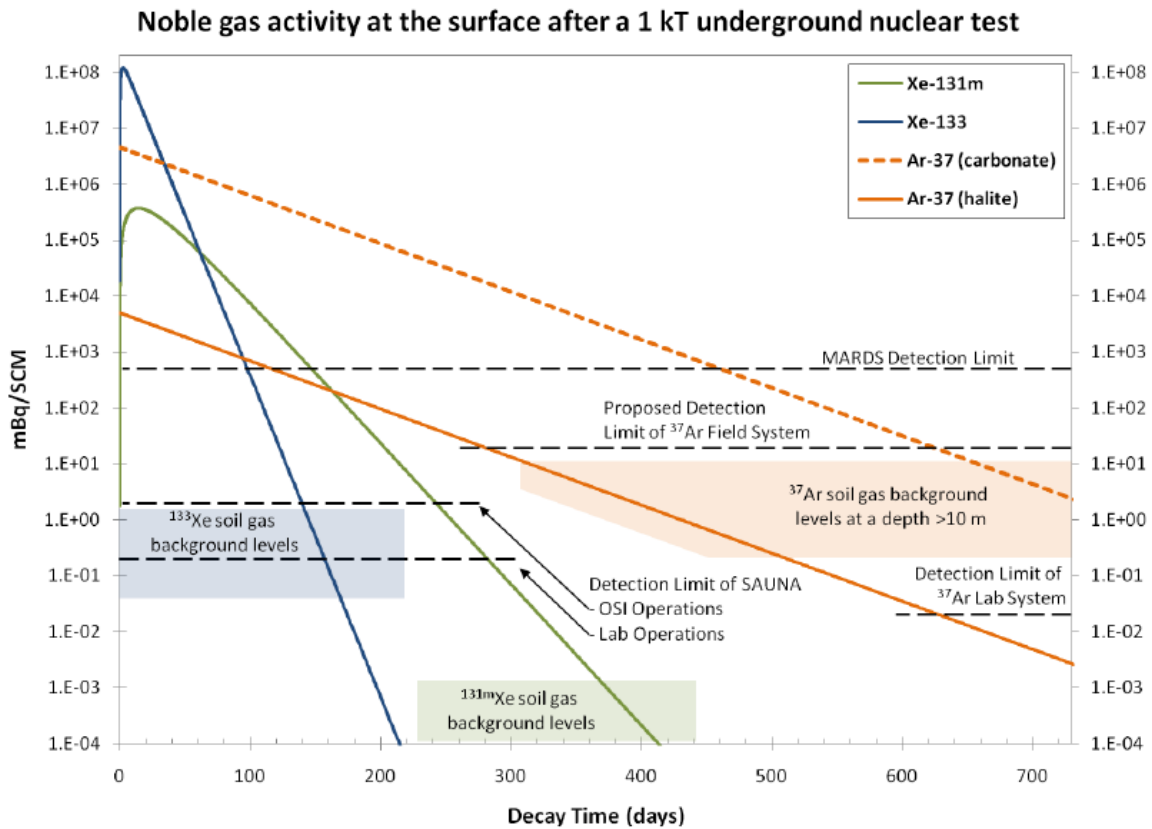


Figure 1.6. The noble gas activity at the surface after a 1 kT underground nuclear test (Haas *et al.*, 2010).

Carrigan (2009) also points out the window for surface detection of gases produced by subsurface nuclear detonation tests. Considering the MARDS (Movable Ar-37 Rapid Detection System) with a detection limit of <sup>37</sup>Ar 500 mBq/m<sup>3</sup>, the <sup>37</sup>Ar detection window opens 80 days after the detonation considering the barometric pumping of the gases in the cavity. The <sup>133</sup>Xe detection window 50 days after the event. The detection windows and radionuclide activities are shown in Figure 1.7.

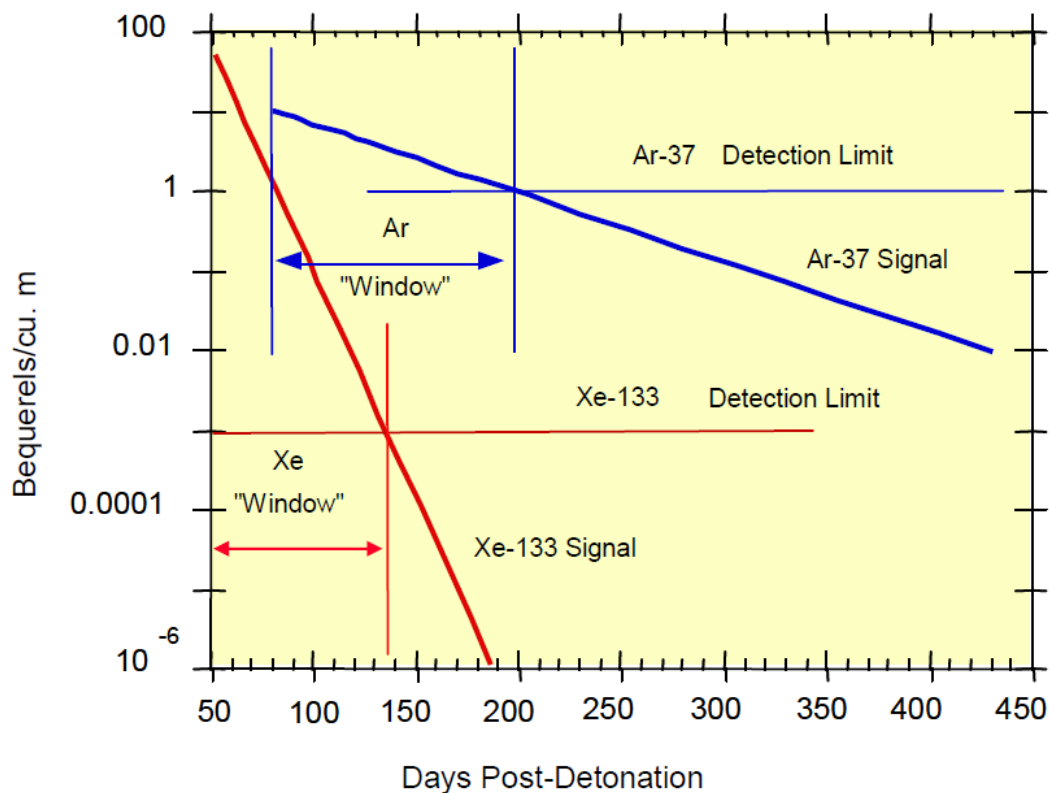


Figure 1.7. The radioxenon and radioargon activities at the surface versus the days post-event (Carrigan, 2009).

The time windows proposed by Carrigan (2009), shown in Figure 1.7, could be lengthened with the Pacific Northwest National Laboratory proposed detection limit reduction from the MARDS system (Haas *et al.*, 2009). In addition, Carrigan (2009) only considered a single value for the  $^{37}\text{Ar}$  induced activity implying that he only considered a single soil type. Calcium concentration varies by soil type, so it is necessary to include a wide range of soil types. Haas *et al.*, (2009) used an MCNPX computer simulation model to calculate the  $^{37}\text{Ar}$  activity at ground level 80 days after a normalized 1 kT test. The calculated activities for all of the soils, except for the calcium-poor halite, exceeded

Carrigan's estimation, shown in Figure 1.8 **Error! Reference source not found.** The higher activities and lowered detection limits will allow an earlier time frame for the possible detection of  $^{37}\text{Ar}$  and also allow the detection of  $^{37}\text{Ar}$  after the current prediction of 200 days post nuclear event.

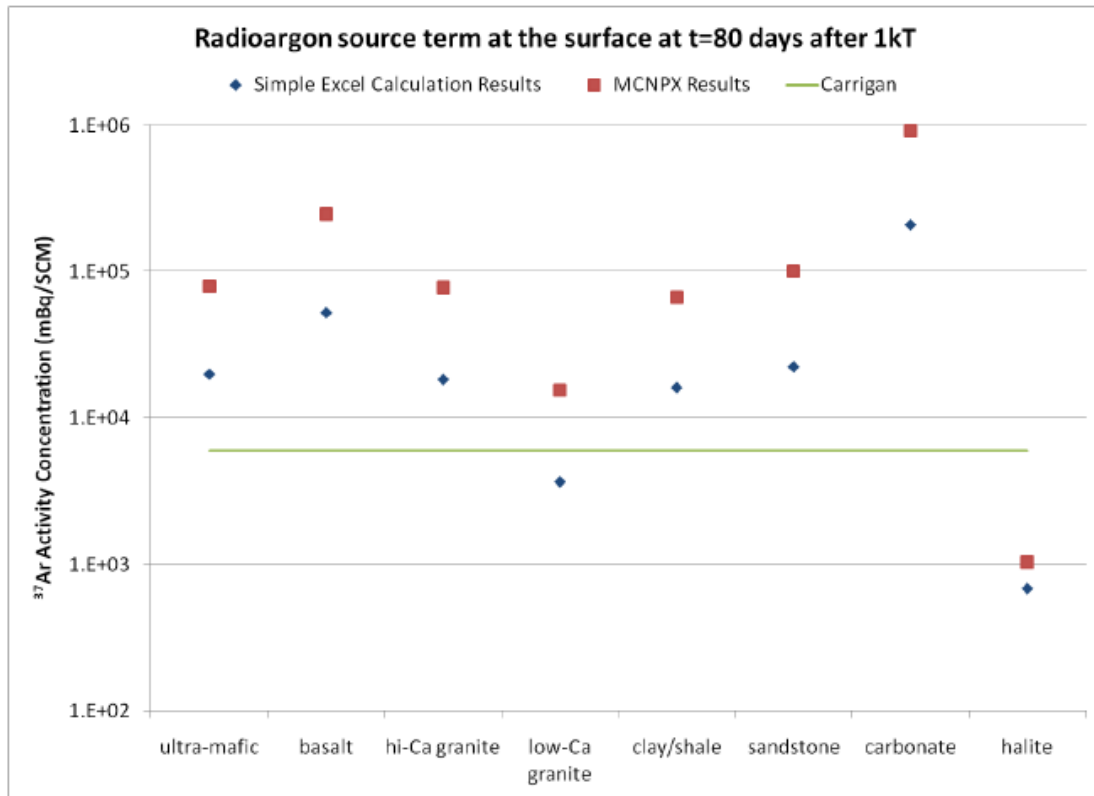


Figure 1.8. The activity expected at the surface 80 days after a normalized 1 kT nuclear subsurface detonation in various rock types (Haas *et al.*, 2009).

The current  $^{37}\text{Ar}$  Ultra Low Background Proportional Counter (ULBPC) developed at Pacific Northwest National Laboratory has a minimum detectable concentration of  $45.1 \text{ mBq m}^{-3}$  with a proposed  $0.2 \text{ mBq m}^{-3}$  for the laboratory system. In order to calibrate and produce a reliable detector, laboratory analysis of the system is required. Therefore the production of radioargon is a necessary step in the detector

verification process. The expectation for the amount of radioargon produced from a nuclear detonation must also be considered. Without the option of a nuclear test, radioargon samples produced through similar production pathways are necessary for system calibration, quality assessment and quality control exercises.

## 1.2 Literature Review

The production of  $^{37}\text{Ar}$  has been mainly used to calibrate detectors. A gaseous  $^{37}\text{Ar}$  source has been used as a check source for neutrino experiments (Abdurashitov *et al.*, 2002; Abdurashitov *et al.*, 2005; Barsanov *et al.*, 2006). The neutrinos are emitted when the  $^{37}\text{Ar}$  decays by electron capture to  $^{37}\text{Cl}$ . The  $^{37}\text{Ar}$  source is optimal because of the high-energy, almost monoenergetic neutrino (Formaggio *et al.*, 2012). The decay gives off an 811 keV neutrino at an intensity of 90.2% and an 813 keV neutrino with an intensity of 9.8%. In the past, the drawbacks of this target have been the expense and difficulty of creating a high quality source. The fast flux reactor necessary and the large scale processing of CaO with nitric acid are included in the major problems. However, this is still the preferred source type for neutrino experiments because there is not a gamma-ray given off—only internal bremsstrahlung. The other two commonly used neutrino sources,  $^{51}\text{Cr}$  and  $^{65}\text{Zn}$ , have gamma-rays at 320 keV and 1.1 MeV, respectively. Both  $^{51}\text{Cr}$  and  $^{65}\text{Zn}$  can be produced via a radiative capture reaction, which is much easier to accomplish using a thermal neutron spectrum research reactor.

The use of an ultra-low-background proportional counter (ULBPC) for verification regime of the CTBT is being calibrated using radioargon (Aalseth *et al.*, 2010). An energy spectrum is shown in Figure 1.9. The current ULBPC at Pacific

Northwest National Laboratory has a sensitivity level of  $45.1 \text{ mBq m}^{-3}$  (Aalseth *et al.*, 2010) with a projected laboratory system of  $0.2 \text{ mBq m}^{-3}$  in development. Therefore, additional testing and development is necessary. This will require additional radioargon samples of various activity concentrations.

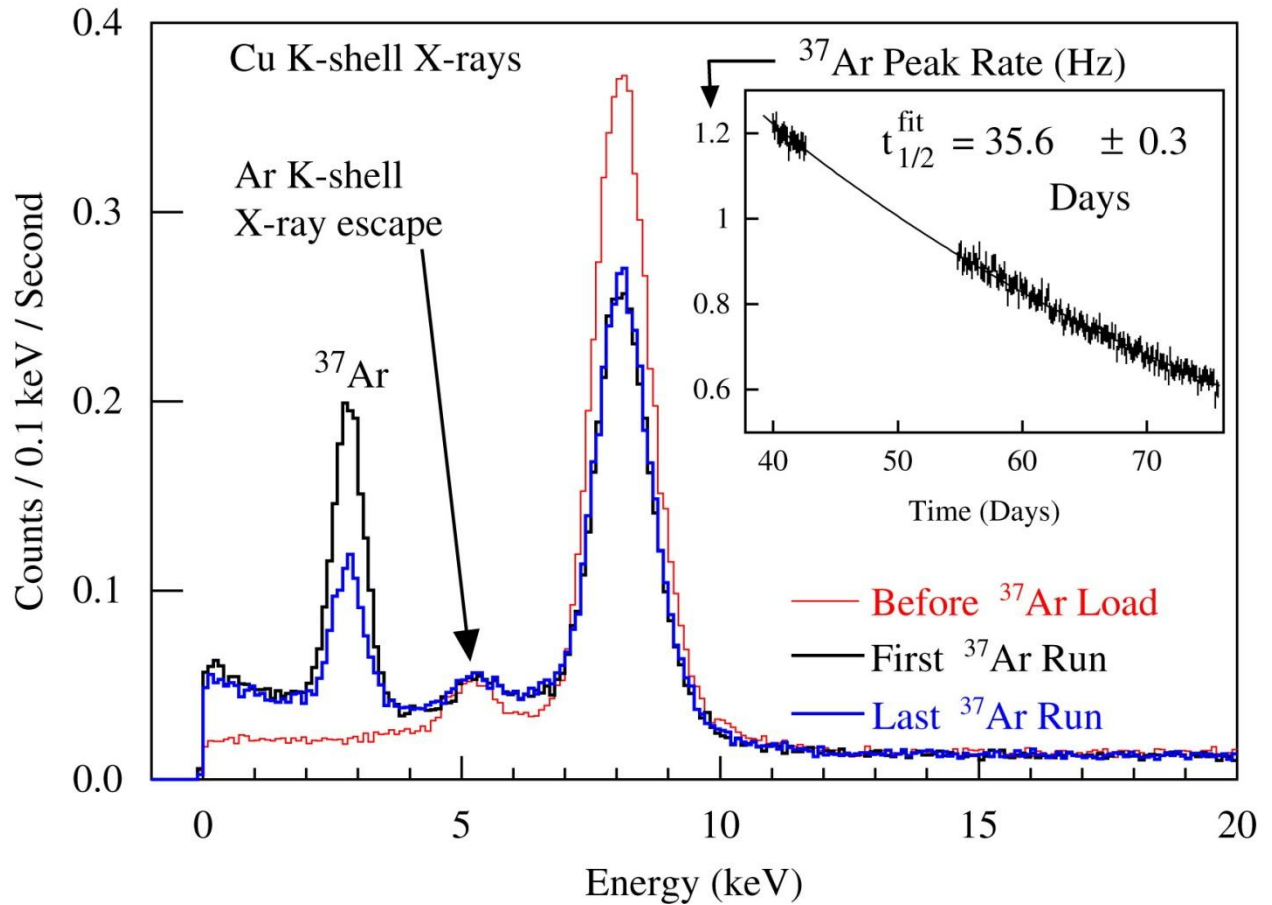


Figure 1.9. ULBPC energy spectra (Aalseth *et al.*, 2010).

### 1.2.1 CALIBRATION OF ULBPC

The development of an ultra-low-background proportional counter (ULBPC) is necessary to detect <sup>37</sup>Ar. Using the system (Aalseth *et al.*, 2010), the argon in the air was separated and counted. The 2.822 keV peak from the K-shell absorption is used to detect the <sup>37</sup>Ar. With a sample from The University of Texas at Austin, based on the 90.2%

branching ratio of the K-shell absorption allowed for the calculation of the activity of  $^{37}\text{Ar}$  to be  $1.50 \pm 0.02$  Bq. Using the Currie method (Currie 1968), the  $L_D$  and  $L_C$  for the detector system are 136.4 counts and 121 counts, respectively.

### 1.2.2 PRODUCTION OF $^{37}\text{Ar}$ BY IRRADIATION OF CALCIUM-CONTAINING COMPOUNDS

The need to develop a detector capable of measuring the solar neutrino radiation prompted Abdurashitov *et al.*, to create a strong  $^{37}\text{Ar}$  source (2002). In the development phase, the irradiation of natural argon gas (99.9997%) was compared to the irradiation of a calcium-containing compound (Michael *et al.*, 1984). The group used a high-purity calcium metal (99.85%) and natural argon vacuum sealed in quartz vials. The projected specific activities were 100 Ci/g  $^{37}\text{Ar}$  for the natural argon irradiation versus  $10^5$  Ci/g  $^{37}\text{Ar}$  for the metallic calcium sample.

The large scale production of the  $^{37}\text{Ar}$  target used CaO with a fast reactor through the  $^{40}\text{Ca}(n,\alpha)$  reaction pathway. Due to the separation difficulties encountered with the metallic calcium the group decided to use CaO, which also had a high density of calcium. The separation of radioargon from the CaO requires a waste intensive step with nitric acid. The process, started in April 2004, placed 330 kg of pressed calcium-oxide (CaO) in the BN-600 fast-neutron reactor in Zarechny, Russia for six months (Barsanov *et al.*, 2006). Through a neutron, alpha interaction with  $^{40}\text{Ca}$ ,  $^{37}\text{Ar}$  is produced. The flux at the sample location was  $2.3 \times 10^{15}$  neutrons/cm<sup>2</sup>/s with  $1.7 \times 10^{14}$  neutrons/cm<sup>2</sup>/s with energies above the  $^{40}\text{Ca}$  (n, $\alpha$ ) reaction threshold of 2 MeV. The calcium oxide samples spent 164 days in the core through the routine operation of the facility.

After a week of cooling time (Barsanov *et al.*, 2006), the irradiated CaO samples were dissolved in nitric acid. The argon gas was removed from the system by flowing helium gas through the system. The composition of the gas after this procedure is shown in Table 1.2 (Abdurashitov *et al.*, 2006). The sample was purified with the use of an activated charcoal section at -196°C, which allowed for the adsorption of the  $^{37}\text{Ar}$  gas.

Table 1.2. The composition of the gas by percent volume after being removed from the CaO sample container (Abdurashitov *et al.*, 2006).

Gas	% by volume
H <sub>2</sub>	1.34±0.32
He	56.62±0.96
N <sub>2</sub>	12.67±0.77
O <sub>2</sub>	1.20±0.17
$^{36}\text{Ar}$	0.77±0.16
$^{37}\text{Ar}$	2.87±0.15
$^{38}\text{Ar}$	13.12±0.37
$^{39}\text{Ar}$	2.40±0.12
$^{40}\text{Ar}$	6.81±0.41
CO <sub>2</sub>	2.20±0.11

### 1.2.3 DETECTION OF RADIOARGON ISOTOPES

The majority of the energy released from the decay of  $^{37}\text{Ar}$  is through neutrinos varying in energy from 811 to 813 keV per decay. The remaining energy is released through Auger electrons, recoil nuclei, and internal-bremsstrahlung photons. The possible decay modes, energy released, and branching ratios are shown in Table 1.3.

Table 1.3.  $^{37}\text{Ar}$  decay modes and released energy (Barsanov *et al.*, 2006).

Decay Mode	Energy release (keV)	Branching ratio for $^{37}\text{Ar}$ decays through a given mode	Energy release per event of $^{37}\text{Ar}$ decay (keV/decay)
<b>K capture</b>	2.8224	0.9017±0.0024	2.5450±0.0068
<b>L capture</b>	0.2702	0.0890±0.0027	0.0240±.0007
<b>M capture</b>	0.0175	0.0093 <sup>+0.0006</sup> <sub>-0.0004</sub>	0.0002
<b>IB 1s</b>	325 (avg)	~0.0005	0.16±0.02
<b>IB 2s</b>	325 (avg)	~0.00007	0.021±0.002
<b>IB p</b>	10 (avg)	~0.00007	~0.0007
<b>Sum</b>			2.751±0.021

#### 1.2.4 RADIOARGON DATING

The  $^{40}\text{Ar}/^{39}\text{Ar}$  technique for potassium-argon dating has been used since the 1960s (Sigurgeirsson 1962, Merrihue 1965). The radiogenic  $^{40}\text{Ar}$  is generated from an electron capture decay of  $^{40}\text{K}$  with a branching ratio of 10.72%. The age can be calculated using the potassium-argon age equation (Dalrymple *et al.*, 1981). If all of the daughter atoms are due to the decay of the parent, then the age may be calculated as

$$t = \frac{1}{\lambda} \ln \left( \frac{D}{N} + 1 \right) \quad (1.1)$$

where

N is the number of parent atoms

D is the number of daughter atoms

This is not the case for  $^{40}\text{Ar}$ . There is a naturally occurring component and the part from the decay of  $^{40}\text{K}$ . If we assume

$$D_t = D_0 + D \quad (1.2)$$

where

$D_t$  is the total amount of the daughter product, corrected by realizing there is a naturally occurring component

$D_0$  is the initially present or naturally occurring number of atoms of the daughter nuclide

Therefore,

$$t = \frac{1}{\lambda} \ln \left( \frac{D_t - D_0}{N} + 1 \right) \quad (1.3)$$

Distinguishing the initially present and radiogenic  $^{40}\text{Ar}$  is done by using a natural argon gas tracer and calculating the ratios of the argon isotopes.

### 1.2.5 APPLICATIONS

The current production of radioargon isotopes in a lab environment is mainly used to calibrate detectors. Pacific Northwest National Laboratory is currently using the  $^{37}\text{Ar}$  samples for the testing of the ULBPC (Aalseth *et al.*, 2010). The Baksan Neutrino Observatory used  $^{37}\text{Ar}$  to calibrate their gallium neutrino detector used for the detection of solar neutrinos (Barsanov *et al.*, 2006; Abdursashitov *et al.*, 2006; Abdurashitov *et al.*, 2002).

The monitoring of radioxenon in the atmosphere is helpful for detecting global nuclear activities. In order to differentiate between a peaceful nuclear use—medical isotope production, nuclear reactors, etc.—and a nuclear explosion, the ratio of the radioxenon isotopes is used. Unfortunately the half-lives of some of the radioxenon isotopes are too short to be useful under current testing methods. This limits the

acquisition window for the time after the detonation that the air can be successfully monitored for radioxenon produced from the possible nuclear detonation. The short half-lives also bring on a problem with delayed testing. A sample containing  $^{133\text{m}}\text{Xe}$  (2.19 day half-life) needs to arrive at the laboratory much faster than if the sample contains  $^{37}\text{Ar}$  (35 day half-life). Therefore, radioargon monitoring is an additional noble gas monitoring option for the verification of nuclear detonations.

The main goals of this research are:

1. Production of  $^{37}\text{Ar}$  through the irradiation of natural argon gas.
2. Production of  $^{37}\text{Ar}$  through the irradiation of calcium-containing compounds.
3. Production of 1 mBq  $^{42}\text{Ar}$  through the irradiation of natural argon gas.
4. Characterizing the 3L irradiation facility using an MCNPX model and neutron density monitoring wires.

## CHAPTER 2: THEORY

In the past,  $^{37}\text{Ar}$  was produced as a check source for anti-neutrino detectors. Recently radioargon isotopes have moved into the international nuclear monitoring community for the possibility of providing an additional noble gas to distinguish regular nuclear activities—medical isotope production, nuclear reactor operations, and beam line work—and underground, clandestine nuclear testing. The difference in radioargon production ratios is examined through this section.

### 2.1 Radioargon Production in Nuclear Explosions

The amount of material activated in a possible nuclear detonation depends on many variables. The major consideration includes the type of material that will be activated. In an underground nuclear explosion, a large number of neutrons will interact with surrounding material, most likely soil or rock. If the nuclear detonation is in the atmosphere, the main mode of radioargon production will be the absorption of neutrons by the naturally occurring argon gas in the air. The ratios of radioargon isotopes produced through these two methods differ greatly.

The main radioargon production mechanism in an underground nuclear detonation event will be the activation of the calcium within the soil and rock. Therefore, the model of the activation of different soils with different isotopic compositions is an important step to know the possible radioargon production ranges in the event of a nuclear detonation. The  $^{37}\text{Ar}$  production is dependent on the  $^{40}\text{Ca}$  concentration in the soil. The calcium content in soil is dependent on soil type, and  $^{40}\text{Ca}$  is 96.941% of the naturally occurring Ca. Therefore, the underground nuclear detonation will produce a

radioargon isotopic signature that is dominated by  $^{37}\text{Ar}$  with small traces of  $^{41}\text{Ar}$ . Using a basic standard for soil composition (Wedepohl 1971), the calcium content in the soil can be considered to be 28,770 parts per million. Assuming a  $1\text{ m}^3$  cavity radius and a  $1.5\text{ g/cm}^3$  soil density (Wielopolski *et al.*, 2004; Frank & Tolgyessy, 1993), this yields  $5.864 \times 10^6$  g of soil including  $1.632 \times 10^5$  g of  $^{40}\text{Ca}$ .

For a more specific design, the radius of the blast cavity can be calculated (Fokin, 2000)

$$r = \left( \frac{3}{4} \pi \frac{k_{\text{res}} Q U_{\text{sp}}}{P_{\text{h}}} \right)^{1/3} \quad (2.1)$$

where

$r$  is the radius of the blast cavity (m)

$Q$  is the mass of the charge (kg)

$U_{\text{sp}}$  is the specific energy (kgm/kg)

$P_{\text{h}}$  is the counter pressure at depth of the explosion ( $\text{kg/m}^2$ )

$k_{\text{res}}$  is the energy expended on the expansion of the cavity, such that

The equation can be simplified to

$$r = 0.2842 \left( \frac{E_0}{P_{\text{h}}} \right)^{1/3} \quad (2.2)$$

where

$E_0$  is the initial energy of the explosion ( $QU_{\text{sp}}$ )

This radius can be used to calculate the volume of the cavity created by an underground nuclear explosion. The  $^{37}\text{Ar}$  activity source term can be established.

The  $^{37}\text{Ar}$  activity created from an underground nuclear device detonation was calculated using an MCNP5-Monte Burns-ORIGEN 2.2 model (Trellue, 1998), which considered a variety of averages for soil and rock compositions. This model was based on a 1 kT weapon's grade fissile sphere ( $k_{\text{eff}} \sim 1.0$ ) surrounded by a soil or rock (Lowrey, 2010, Egnatuk *et al.*, 2011). An 8.7 cm radius spherical  $^{235}\text{U}$  core and a 5.1 cm radius spherical weapons grade plutonium core were used. The composition of the weapons grade uranium and plutonium is as defined in Stacey (2011). Using MCNP5, the soil and rock samples considered a radius of 2 m around the fissile core. This dimension is set so that 99.9% of the neutrons remain in the system.

Two soil compositions and three rock compositions were compared to model a range of materials, which the neutrons would interact with in an underground setting. The activity and concentration of the isotopes created for both a  $^{235}\text{U}$  and  $^{239}\text{Pu}$  spheres were calculated for a 1 kT device. The decay curves of the isotopes were calculated for times ranging from 5 minutes to 100 days after the detonation using ORIGEN 2.2. The activity of the  $^{37}\text{Ar}$  created through the activation of the soil is shown in Table 2.1. The results show that after 100 days of decay there should be  $86.2 \pm 45.5$  Ci per kT of  $^{37}\text{Ar}$  for a high enriched U weapon. For a plutonium based weapon, the calculations show  $138 \pm 82.0$  Ci per kT of  $^{37}\text{Ar}$  at 100 days decay. The plutonium based weapon produces more activation per kT due to more neutrons being released per fission—2.4680 neutrons/fission for  $^{235}\text{U}$  and 2.9460 neutrons/fission for  $^{239}\text{Pu}$ . The wide range of  $^{37}\text{Ar}$  activities is due to the range of calcium present in the rock or soil compositions. The hydrogen content of the rock or soil also has a large effect on the soil activation products.

Table 2.1. Activities of  $^{37}\text{Ar}$  in Ci/kT resulting from source term calculation in various surrounding soil and rock concentrations (Lowrey, 2010, Egnatuk *et al.*, 2011).

Soil Type		Initial	10 hr	1 day	10 days	30 days	100 days
U Core	Wedepohl (Rock)	1.014E+03	1.005E+03	9.937E+02	8.316E+02	5.597E+02	1.401E+02
	Taylor (Rock)	9.455E+02	9.377E+02	9.270E+02	7.757E+02	5.222E+02	1.307E+02
	Mason (Rock)	4.616E+02	4.579E+02	4.526E+02	3.788E+02	2.549E+02	6.380E+01
	Bowen (Soil)	3.488E+02	3.460E+02	3.420E+02	2.862E+02	1.926E+02	4.820E+01
	Vinogradov (Soil)	3.477E+02	3.448E+02	3.409E+02	2.853E+02	1.920E+02	4.805E+01
Pu Core	Wedepohl (Rock)	1.760E+03	1.745E+03	1.725E+03	1.444E+03	9.717E+02	2.432E+02
	Taylor (Rock)	1.502E+03	1.489E+03	1.472E+03	1.232E+03	8.294E+02	2.075E+02
	Mason (Rock)	7.241E+02	7.182E+02	7.100E+02	5.941E+02	3.999E+02	1.001E+02
	Bowen (Soil)	5.021E+02	4.980E+02	4.922E+02	4.119E+02	2.773E+02	6.938E+01
	Vinogradov (Soil)	5.011E+02	4.970E+02	4.913E+02	4.111E+02	2.767E+02	6.925E+01

The final piece of the subsurface nuclear detonation signal includes the gas diffusion to the surface and the transport of the radionuclides. The transport of the gas is dependent on the atmospheric pressure that causes the diffusion and flow along the cracks. The NOAA Air Resource Laboratory Hybrid Single-Particle Lagrangian Integrated Trajectory (HYSPLIT) transport and dispersion model (Draxler *et al.*, 2012) can be used to for atmospheric modeling of the radionuclide transport.

The activation volume of air requires a different method and a different surrounding medium. The naturally occurring argon in the atmosphere will mostly contain  $^{40}\text{Ar}$  (99.6003%), which will a  $^{41}\text{Ar}$  dominant isotopic signature. The amount of air activated by the explosion can be estimated by calculating the volume of air, which

will interact with the neutrons produced from fission. In order to evaluate the average distance a neutron will travel through a medium, the Fermi age equation (Duderstadt & Hamilton, 1976) can be used. In order to solve for  $r$ , the Fermi age can be evaluated by

$$\tau(u) = \int_0^u du' \frac{D(u')}{\xi \Sigma_s(u')} \quad (2.3)$$

where

$u = \ln\left(\frac{E_0}{E}\right)$ , the neutron lethargy

$\tau$  is the Fermi age in  $\text{cm}^2$

$D$  is the neutron diffusion coefficient,  $D = \frac{1}{3\Sigma_{tr}}$

$\xi$  is the average change in lethargy in an elastic collision,  $\xi = 1 - \frac{(A-1)^2}{2A} \ln\left(\frac{A+1}{A-1}\right)$

$A$  is the mass number of the target nucleus

$\Sigma_s$  is the macroscopic scattering cross-section

In order to assume a slowdown to neutron energies, the previous equation can put in terms of energy when considering

$$du = \frac{E}{E_0} \left(-\frac{E_0}{E^2}\right) dE = -\frac{dE}{E} \quad (2.4)$$

Therefore, the Fermi age described in terms of the neutron energy is

$$\tau(u) = \int_E^{E_0} \frac{dE}{E} \frac{D(E)}{\xi \Sigma_s(E)} \quad (2.5)$$

To apply the above equation to the slowdown of neutrons to a thermal range, the Fermi age is

$$\tau_{th}(u) = \int_{E_{th}}^{E_0} \frac{dE}{E} \frac{D(E)}{\xi \Sigma_s(E)} \quad (2.6)$$

The Fermi age is used to calculate the distance traveled away from the neutron birth place

$$\tau = \frac{1}{6} \langle r^2 \rangle \quad (2.7)$$

where

$r$  is the average distance a neutron travels away from the position it entered the system at energy  $E_0$ , the maximum energy a neutron can achieve in this system.

The volume of air activated can be described using the average neutron distance traveled  $r$  as

$$V_{air} = \frac{4}{3} \pi r^3 \quad (2.8)$$

The volume can be used to calculate the amount of argon in the air by

$$m_{Ar} = V \rho \phi_{Ar} \quad (2.9)$$

where

$m_{Ar}$  is the mass of the argon in the volume of air

$V$  is the volume of air activated

$\rho$  is the density of the air

$\phi_{Ar}$  is the abundance of argon in air (0.93%)

The number of atoms of a specific argon isotope in the volume of air can be calculated by

$$N_i = \frac{m_{Ar}}{m_a} \phi_i N_A \quad (2.10)$$

where

$N_i$  is the number of atoms of  $i^{\text{th}}$  naturally occurring isotope of argon

$m_a$  is the atomic mass of argon

$\phi_i$  is the natural abundance of the  $i$ th isotope

$N_A$  is Avogadro's number

## 2.2 Activation and Decay

The production ratios will be calculated by counting a sample with an HPGe detector and using the activity of the radionuclides that decay via gamma-ray emission at the time of the count. The activity at the end of irradiation will be calculated considering the half-life of the radionuclide in question. Then the production ratios will be established by considering the reactions and decays during the irradiation. Figure 2.1 shows the radionuclide build-up during the irradiation period ( $t_i$ ) and decay during the decay ( $t_d$ ) and counting ( $t_c$ ) periods.

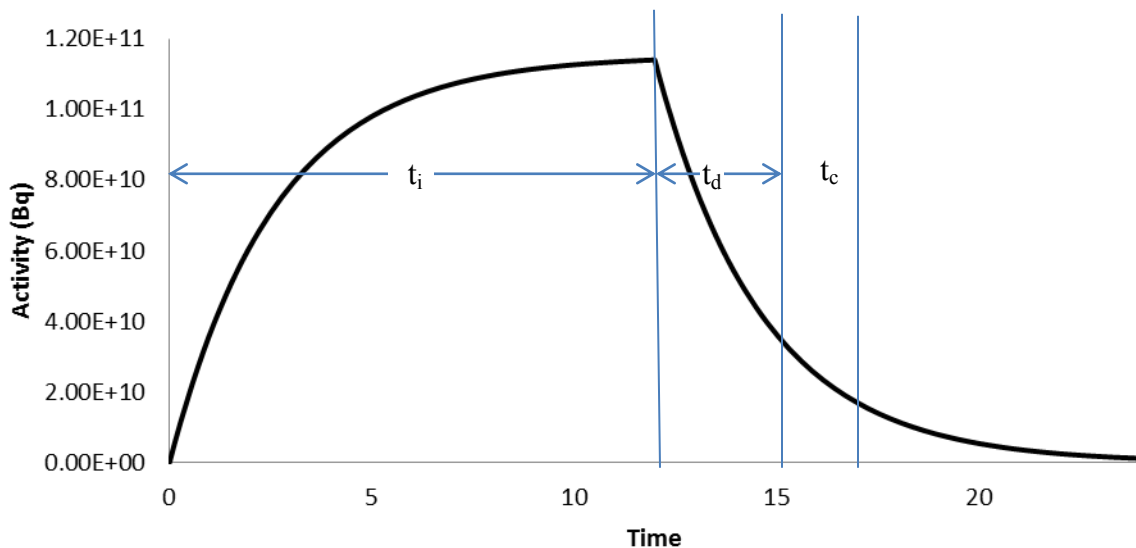


Figure 2.1. The activation and decay of a radionuclide.

The change of number of atoms during the irradiation time, production time, and counting time can be calculated by

$$\frac{dN^X}{dt} = \text{sources} - \text{losses} \quad (2.11)$$

where

$\frac{dN^X}{dt}$  is the time rate of change of the number of atoms of nuclide X

For this activation section of the graph, the source term will be related to the production avenues—decay from a parent radionuclide or through a number of neutron absorption reactions. For this example, we will exclude any parent-daughter relationship. Therefore, the neutron absorption reactions can be defined by

$$N_X = N_Y \sigma_{Y \rightarrow X} \phi \quad (2.12)$$

where

$N_Y$  is the number of incident atoms of nuclide Y undergoing neutron irradiation

$\sigma_{Y \rightarrow X}$  is the cross section for the reaction that will take nuclide Y plus a neutron and produce nuclide X

$N_X$  is the number of atoms of nuclide X

$\phi$  is neutron flux incident on nuclide Y ( $\text{n cm}^{-2} \text{ s}^{-1}$ )

The losses during the irradiation period include the decay of the radionuclide represented by

$$A = \lambda N \quad (2.13)$$

where

A is the activity in Bq

$\lambda$  is the decay constant

N is the number of atoms of the radioactive nuclide

Therefore, the neutron absorption reactions with the radionuclide can be expressed as  $(N_X \sigma_a \phi)$ . The rate of change of the amount of atoms of a specific nuclide can be expressed as

$$\frac{dN_X(t)}{dt} = N_Y(t) \sigma_{Y \rightarrow X} \phi - \lambda N_X(t) - N_X(t) \sigma_a \phi \quad (2.14)$$

where

$N_X(t)$  is the number of atoms of nuclide X at time t

$\sigma_a$  is the absorption cross section of nuclide  $N_X$

The function of  $N_X$  is dependent on the amount of  $N_Y$  at a given time. Therefore, a series of rate of change equation for each dependent radionuclide will need to be solved.

The decay of each radionuclide, if there are no parent-daughter decay relationships, only requires the solving for the radionuclide of interest. The use of an HPGe for the detection of gamma ray requires the calculation of the decay that happens while the sample is being counted. Therefore,

$$C = \frac{N_0 \phi \sigma_c \varepsilon \gamma}{\lambda} (1 - e^{-\lambda t_i}) (e^{-\lambda t_d}) (1 - e^{-\lambda t_c}) \quad (2.15)$$

where

C is counts

$\varepsilon$  is the detector efficiency at the energy/channel for the photon/particle to be detected

$\gamma$  is the intensity of the photon/particle upon decay of the radionuclide

$t_i$  is the irradiation time

$t_d$  is the decay time

$t_c$  is the count time

## **2.3 Radioargon Production in Reactor Facility**

### **2.3.1 PRODUCTION OF $^{37}\text{Ar}$**

The production methods for  $^{37}\text{Ar}$  that will be examined in this work include the irradiation of natural argon and the irradiation of calcium containing compounds. The irradiation of natural argon gas will be dependent on the thermal flux and the calcium irradiation will use the Cd liner to mainly interact with the epithermal and fast neutrons.

#### **2.3.1.1 Irradiation of natural argon**

Natural argon gas is made up of  $^{40}\text{Ar}$ ,  $^{38}\text{Ar}$ , and  $^{36}\text{Ar}$  as shown in Table 2.2. During irradiation, the gas slowly acquires radioargon isotopes  $^{41}\text{Ar}$ ,  $^{39}\text{Ar}$ , and  $^{37}\text{Ar}$  through single radiative capture events. Calcium is naturally occurring in the soil. The stable calcium isotope needed to produce  $^{37}\text{Ar}$ ,  $^{40}\text{Ca}$ , has an atomic abundance of 96.941%. The natural abundance and thermal cross-sections of the stable argon isotopes is shown in Table 2.2.

Table 2.2. The natural abundance of argon isotopes (Rosman & Taylor, 1997) and their thermal radiative capture cross-sections (Mughabghab *et al.*, 1981).

Isotope	Natural Abundance	Thermal absorption cross-section (b)
<sup>36</sup> Ar	0.3365%	5.2±0.5
<sup>38</sup> Ar	0.0632%	0.8±0.2
<sup>40</sup> Ar	99.6003%	0.660±0.010

The production method using irradiation of the natural argon gas is dependent on the absorption of a neutron by <sup>36</sup>Ar. The creation of a compound nucleus in an excited state has a few possible outcomes. Radiative capture is the outcome used in the production of <sup>37</sup>Ar from <sup>36</sup>Ar, as



where

A is the mass number

\* denotes an excited state

γ is a gamma-ray

Resonance elastic scattering



and inelastic scattering



are the two other outcomes possible from the <sup>37</sup>Ar compound nucleus in an excited state.

Through radiative capture, stable, naturally occurring <sup>36</sup>Ar becomes <sup>37</sup>Ar. The capture cross-section of <sup>36</sup>Ar, as shown in Figure 2.2, is dependent on the energy of the

incident neutron. The thermal dominated neutron spectrum in The University of Texas at Austin TRIGA reactor will provide optimal production of  $^{37}\text{Ar}$  using this method.

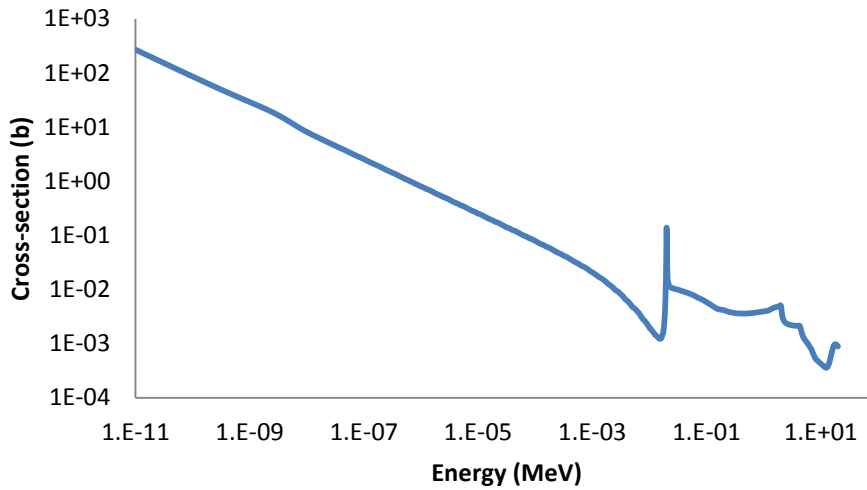


Figure 2.2. The radiative capture cross-section of  $^{36}\text{Ar}$  versus the energy of the incident neutron (Santamarina *et al.*, 2009).

### 2.3.1.2 Irradiation of calcium

The other  $^{37}\text{Ar}$  production avenue includes the irradiation of  $^{40}\text{Ca}$  with fast neutrons. The reaction threshold requires higher energy neutrons than the irradiation of natural argon, but the amount of other radioargon isotopes is minimal.  $^{37}\text{Ar}$  is produced by  $^{40}\text{Ca}(n,\alpha)^{37}\text{Ar}$ . The cross-section of the  $(n,\alpha)$  reaction cross-section is shown in Figure 2.3. The various cross-section libraries differ in the thermal and epithermal regions. The ROSFOND group (Zabrodskaya *et al.*, 2007) would be expected to have the most familiarity with the  $^{40}\text{Ca}(n,\alpha)^{37}\text{Ar}$  pathway due to the large scale production of  $^{37}\text{Ar}$  through the irradiation of calcium-containing compounds. However, there are mistakes in the formatting of the files that make the files unusable.

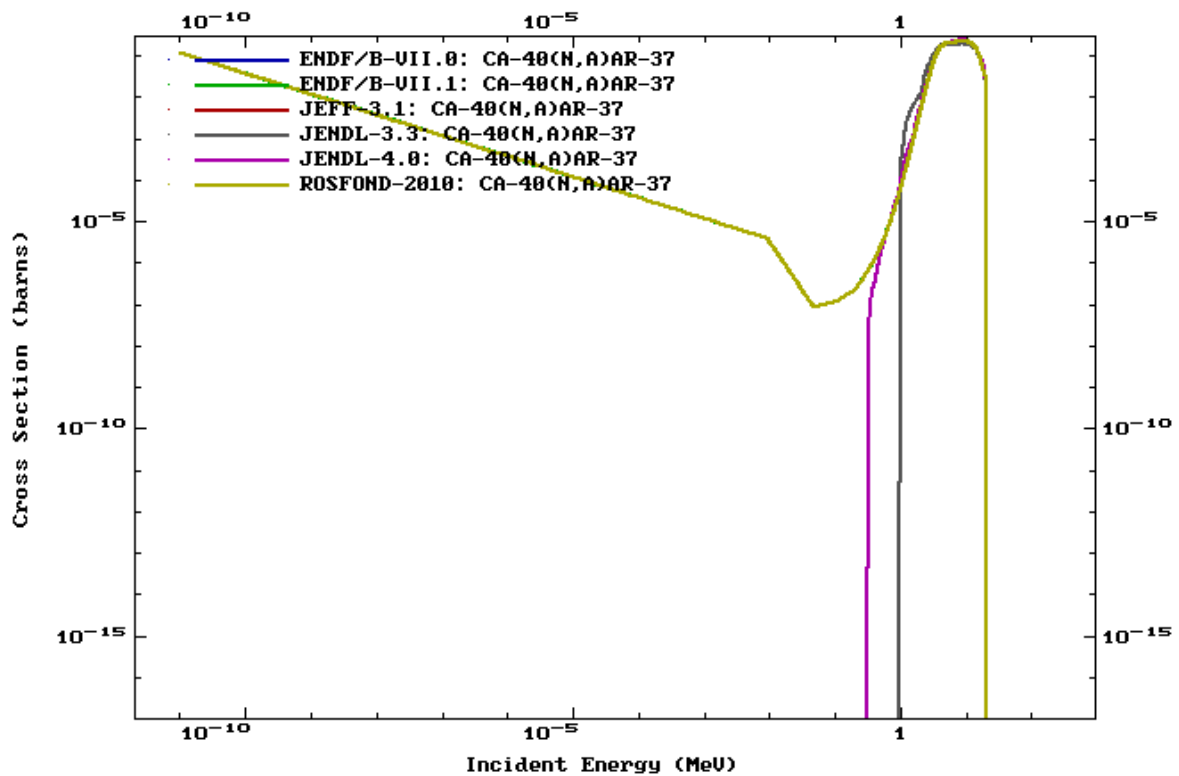


Figure 2.3. The  $(n,\alpha)$  cross-section for  $^{40}\text{Ca}$  (Chadwick *et al.*, 2006; Chadwick *et al.*, 2011; Koning *et al.*, 2006; Shibata *et al.*, 2002; Shibata *et al.*, 2011; Zabrodszkaya *et al.*, 2007).

The ROSFOND (Zabrodszkaya *et al.*, 2007).data does agree with the Riedmann and Purtschert (2001) cross-section, which also assumed the  $1/v$  law for the thermal neutron section. The  $^{40}\text{Ca}(n,\alpha)^{37}\text{Ar}$  reaction cross-section used by the group was pieced together using data and a  $1/v$  fit; the reaction cross-section is shown in Figure 2.4.

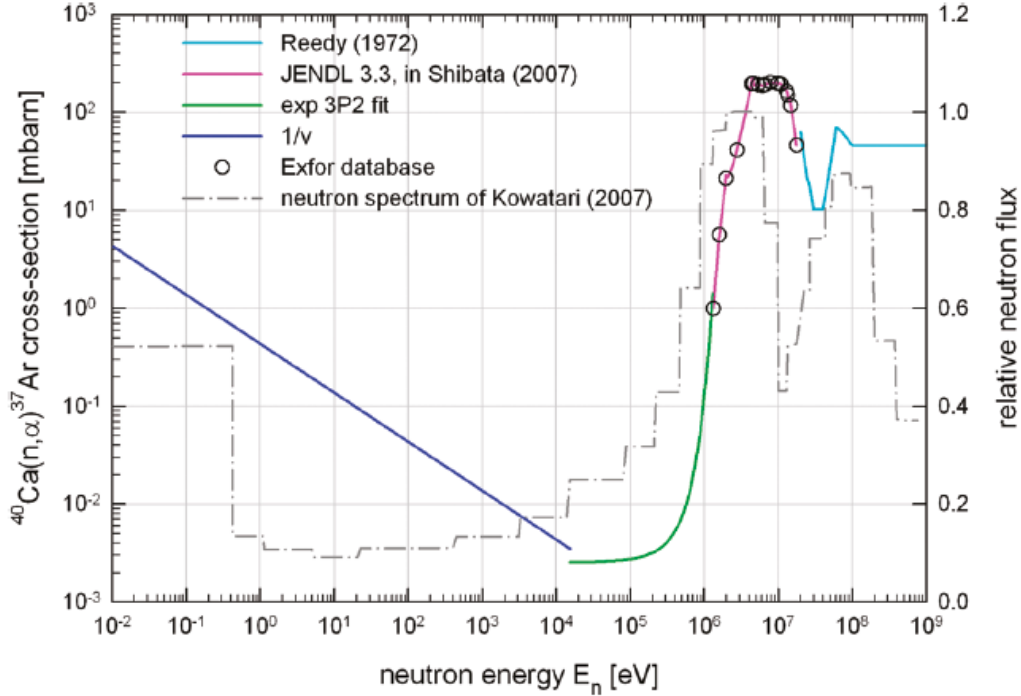


Figure 2.4. The  $^{40}\text{Ca}(n,\alpha)^{37}\text{Ar}$  reaction cross-section data used by Riedmann and Purtschert (2011).

The calculation of the amount of  $^{37}\text{Ar}$  in a sample can be obtained by determining the activity. Argon-37 has a  $35.04 \pm 0.04$  d half-life and decays by electron capture to  $^{37}\text{Cl}$ . It decays by electron capture, such as



Since both  $^{37}\text{Ar}$  and  $^{37}\text{Cl}$  shown in the reaction above are in their ground state, there are no gamma rays emitted—except for a possible internal bremsstrahlung x-ray. In order to measure the  $^{37}\text{Ar}$  decay, the atomic shell cascade resulting from the decay to  $^{37}\text{Cl}$  can be detected with a peak at 2.822 keV from a K electron shell capture on a proportional counter (Barsanov *et al.*, 2006). The majority of the energy released is placed into the neutrino, which has energy between 811 and 813 keV.

The production ratios of radionuclides that decay via gamma-ray emission can be estimated and used to predict the induced activities of  $^{37}\text{Ar}$  and  $^{39}\text{Ar}$ . However, there are conflicting cross-section libraries and data libraries with missing reaction cross-sections. For example, the CINDER90 library agrees with the JENDL 3.3 data (Shibata *et al.*, 2002), but does not reach the peak height of the JENDL 4.0 data (Shibata *et al.*, 2011), shown in Figure 2.5. This could be due to the limited 63 energy group scope of CINDER90 or the weighting the cross-sections.

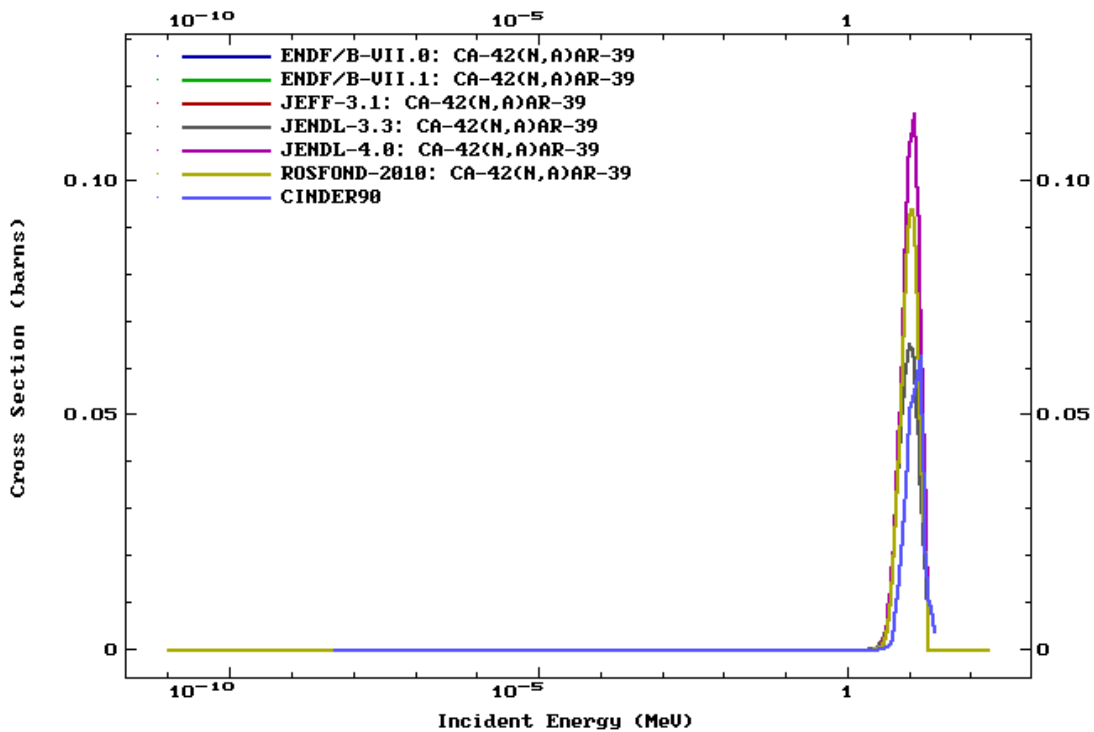


Figure 2.5. The  $^{42}\text{Ca}(n,\alpha)^{39}\text{Ar}$  reaction cross-sections (Chadwick *et al.*, 2006; Chadwick *et al.*, 2011; Koning *et al.*, 2006; Shibata *et al.*, 2002; Shibata *et al.*, 2011; Zabrodskaya *et al.*, 2007).

CINDER90 does not have a  $^{42}\text{Ca}(n,p)^{42}\text{K}$  reaction cross-section. The other libraries once again have similar shapes, shown in Figure 2.6. ENDF, JEFF and

ROSFOND have the same data. JENDL 4.0 is close, but JENDL 3.3 is a much larger and higher shape—similar to the issue with the  $^{42}\text{Ca}(n,\alpha)^{39}\text{Ar}$  reaction cross-section.

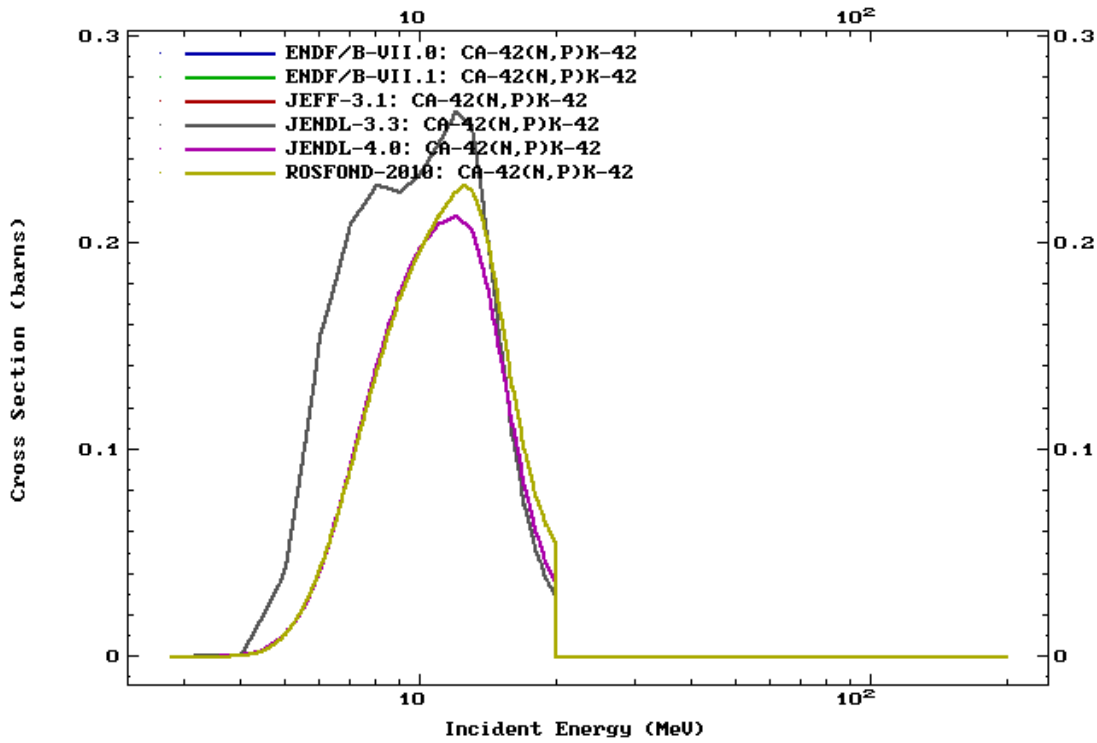


Figure 2.6. The  $^{42}\text{Ca}(n,p)^{42}\text{K}$  reaction cross-sections (Chadwick *et al.*, 2006; Chadwick *et al.*, 2011; Koning *et al.*, 2006; Shibata *et al.*, 2002; Shibata *et al.*, 2011; Zabrodszkaya *et al.*, 2007).

For the  $^{43}\text{Ca}(n,p)^{43}\text{K}$  reaction cross-section, the ROSFOND (Zabrodszkaya *et al.*, 2007), JEFF (Koning *et al.*, 2006), and ENDF (Chadwick *et al.*, 2006; Chadwick *et al.*, 2011) libraries agree—shown in Figure 2.7. The updated JENDL, JENDL 4.0, has a similar shape (Shibata *et al.*, 2011). However, the JENDL 3.3 reaction cross-sections have a different shape and are shifted to the lower energies in comparison to the other libraries (Shibata *et al.*, 2002).

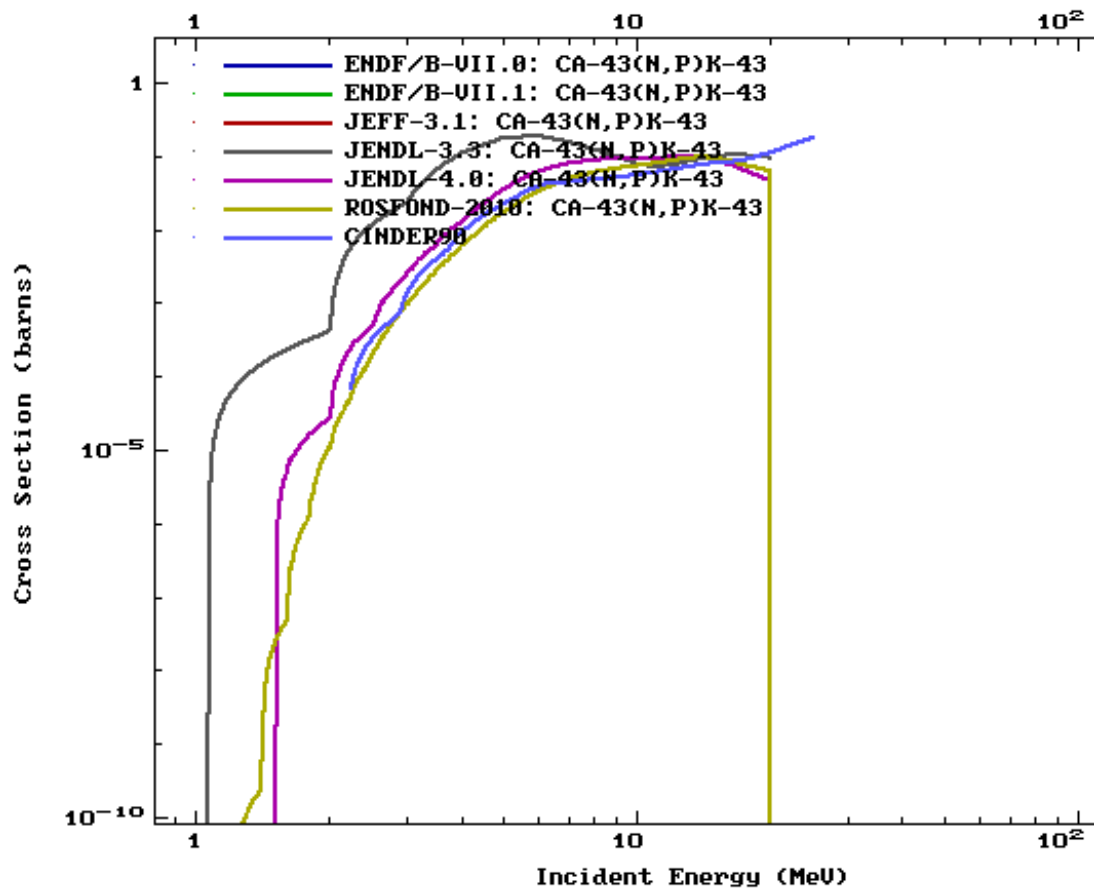


Figure 2.7.  $^{43}\text{Ca}(n,p)^{43}\text{K}$  reaction cross-sections (Chadwick *et al.*, 2006; Chadwick *et al.*, 2011; Koning *et al.*, 2006; Shibata *et al.*, 2002; Shibata *et al.*, 2011; Zabrodskaya *et al.*, 2007).

The  $^{46}\text{Ca}(n,\gamma)^{47}\text{Ca}$  reaction will be significantly decreased with the use of a Cd liner. This reaction pathway will also have only a small amount of calcium to use because  $^{46}\text{Ca}$  is only 0.004% of the naturally occurring Ca. However, the high intensity (71.7%) gamma-ray at 1297.09 keV and the long half-life, 4.53 days allow the radionuclide to be present when some of the initial radionuclides with shorter half-lives have decayed away. The different reaction cross-section libraries agree on this radiative capture cross-section, shown in Figure 2.8.

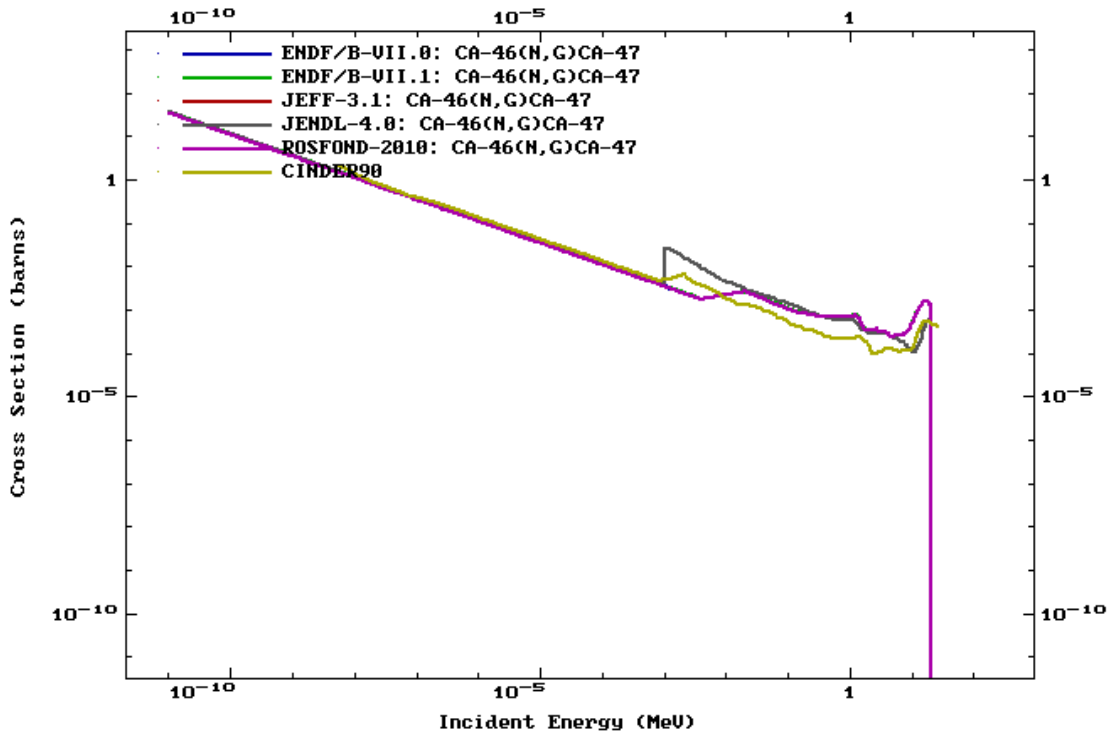


Figure 2.8.  $^{46}\text{Ca}(n,\gamma)^{47}\text{Ca}$  reaction cross-section (Chadwick *et al.*, 2006; Chadwick *et al.*, 2011; Koning *et al.*, 2006; Shibata *et al.*, 2002; Shibata *et al.*, 2011; Zabrodskaya *et al.*, 2007).

## 2.4 Production of Radioargon in a Reactor

The production of  $^{42}\text{Ar}$  through the irradiation of natural argon gas requires a double capture by the stable, naturally occurring  $^{40}\text{Ar}$  isotope.  $^{40}\text{Ar}$  has an isotopic abundance of 99.6003%. The first capture produces  $^{41}\text{Ar}$ , which has half-life of 109.34 minutes. In order to calculate the amount of  $^{42}\text{Ar}$  that will be produced in a given situation, we must start by considering the change in each of the products in the system— $^{40}\text{Ar}$ ,  $^{41}\text{Ar}$ ,  $^{42}\text{Ar}$ , and  $^{42}\text{K}$ . For the case of tracking the production of  $^{42}\text{Ar}$  and counting  $^{42}\text{K}$ ,

$$\frac{dN^{Ar-40}}{dt} = -\phi\sigma_c^{Ar-40}N^{Ar-40}(t) \quad (2.20)$$

$$\frac{dN^{Ar-41}}{dt} = \phi\sigma_c^{Ar-40}N^{Ar-40}(t) - \lambda_{Ar-41}N^{Ar-41}(t) - \phi\sigma_c^{Ar-41}N^{Ar-41}(t) \quad (2.21)$$

$$\frac{dN^{Ar-42}}{dt} = \phi\sigma_c^{Ar-41}N^{Ar-41}(t) - \lambda_{Ar-42}N^{Ar-42}(t) - \phi\sigma_c^{Ar-42}N^{Ar-42}(t) \quad (2.22)$$

$$\frac{dN^{K-42}}{dt} = \lambda_{Ar-42}N^{Ar-42}(t) + \phi\sigma_c^{K-41}N^{K-41}(t) - \lambda_{K-42}N^{K-42}(t) - \phi\sigma_c^{K-42}N^{K-42}(t) \quad (2.23)$$

where

$N(t)$  is the function the number density with respect to time

$t$  is the irradiation time

$\phi$  is the flux within the reactor

$\sigma_c$  is the radiative capture cross-section

$\lambda$  is the decay constant

The above differential equations can be solved in terms of the number density with respect to irradiation time.

$$N^{Ar-40}(t) = N^{Ar-40}(t=0)e^{-\sigma_c^{Ar-40}\phi t} = N_0^{Ar-40}e^{-\sigma_c^{Ar-40}\phi t} \quad (2.24)$$

$$N^{Ar-41}(t) = \frac{\phi\sigma_c^{Ar-40}N_0^{Ar-40}}{\lambda_{Ar-41} + \phi(\sigma_c^{Ar-41} - \sigma_c^{Ar-40})} \left( e^{-(\sigma_c^{Ar-41}\phi + \lambda_{Ar-41})t} - e^{-\sigma_c^{Ar-40}\phi t} \right) \quad (2.25)$$

$$N^{Ar-42}(t) =$$

$$\phi^2\sigma_c^{Ar-40}\sigma_c^{Ar-41}N_0^{Ar-40} * \left[ -\frac{e^{-\sigma_c^{Ar-40}\phi t}}{(\lambda_{Ar-41} + \phi(\sigma_c^{Ar-41} - \sigma_c^{Ar-42}))(\phi(\sigma_c^{Ar-41} - \sigma_c^{Ar-42}) - \lambda_{Ar-42})} + \frac{e^{-(\sigma_c^{Ar-41}\phi + \lambda_{Ar-41})t}}{(\lambda_{Ar-41} + \phi(\sigma_c^{Ar-41} - \sigma_c^{Ar-42}))(\phi(\sigma_c^{Ar-41} - \sigma_c^{Ar-42}) + \lambda_{Ar-41} - \lambda_{Ar-42})} + \frac{e^{-(\sigma_c^{Ar-42}\phi + \lambda_{Ar-42})t}}{(\lambda_{Ar-42} - \lambda_{Ar-41} + \phi(\sigma_c^{Ar-42} - \sigma_c^{Ar-41}))(\phi(\sigma_c^{Ar-42} - \sigma_c^{Ar-40}) + \lambda_{Ar-42})} \right] \quad (2.26)$$

$$\begin{aligned}
N^{K-42}(t) = & \lambda_{Ar-42} \phi^2 \sigma_c^{Ar-40} \sigma_c^{Ar-41} N_0^{Ar-40} * \\
& \left[ \frac{e^{-\sigma_c^{Ar-40} \phi t}}{\left( (-\lambda_{K-42} + \phi(\sigma_c^{Ar-40} - \sigma_c^{K-42}))(\phi(\sigma_c^{Ar-40} - \sigma_c^{Ar-42}) - \lambda_{Ar-42})(\phi(\sigma_c^{Ar-41} - \sigma_c^{Ar-40}) + \lambda_{Ar-41}) \right)} - \right. \\
& \frac{e^{-(\sigma_c^{Ar-41} \phi + \lambda_{Ar-41})t}}{\left( \phi(\sigma_c^{Ar-41} - \sigma_c^{Ar-40}) + \lambda_{Ar-41} \right) \left( \lambda_{Ar-41} - \lambda_{Ar-42} + \phi(\sigma_c^{Ar-41} - \sigma_c^{Ar-42}) \right)} * \\
& \frac{1}{\left( \lambda_{Ar-41} - \lambda_{K-42} + \phi(\sigma_c^{Ar-41} - \sigma_c^{K-42}) \right)} - \\
& \frac{e^{-(\sigma_c^{Ar-42} \phi + \lambda_{Ar-42})t}}{\left( \lambda_{Ar-42} - \lambda_{K-42} + \phi(\sigma_c^{Ar-42} - \sigma_c^{K-42}) \right) \left( \lambda_{Ar-42} + \phi(\sigma_c^{Ar-42} - \sigma_c^{Ar-40}) \right)} * \\
& \frac{1}{\left( \lambda_{Ar-42} - \lambda_{Ar-41} + \phi(\sigma_c^{Ar-42} - \sigma_c^{Ar-41}) \right)} - \\
& \left. \frac{e^{-(\phi \sigma_c^{K-42} + \lambda_{K-42})t}}{\left( \lambda_{K-42} - \lambda_{Ar-42} + \phi(\sigma_c^{K-42} - \sigma_c^{Ar-42}) \right) \left( \lambda_{K-42} + \phi(\sigma_c^{K-42} - \sigma_c^{Ar-40}) \right)} * \frac{1}{\left( \lambda_{K-42} - \lambda_{Ar-41} + \phi(\sigma_c^{K-42} - \sigma_c^{Ar-41}) \right)} \right]
\end{aligned}
\tag{2.27}$$

The above equations are valid for the amount of an isotope during irradiation or immediately after irradiation.

Since our sample was going to be allowed to sit for a period of time that would allow the  $^{42}\text{K}$  and the  $^{42}\text{Ar}$  equilibrate, the activation equations could be simplified. The sample also included a large enough amount of the stable argon isotopes that their loss due to absorption interactions was minimal. The cross-sections used were flux weighted collapsed cross-sections.

$$\bar{\sigma} = \frac{\sum_{i=1}^{63} \sigma_i \phi_i}{\sum_{j=1}^{63} \phi_j} \tag{2.28}$$

where

$\sigma_i$  is the cross-section of the  $i^{\text{th}}$  energy step and

$\phi_i$  is the flux at the  $i^{\text{th}}$  energy step.

Therefore, the activation equation used for the production of  $^{37}\text{Ar}$ ,  $^{39}\text{Ar}$ ,  $^{41}\text{Ar}$ , and  $^{42}\text{Ar}$  used in conjunction with the MCNPX model throughout this project are

$$\frac{dN_{Ar-37}(t)}{dt} = N_{0,36}\overline{\sigma_c^{36}}\phi - (\overline{\sigma_a^{37}}\phi + \lambda_{37})N_{Ar-37}(t) \quad (2.29)$$

$$\frac{dN_{Ar-39}(t)}{dt} = N_{0,38}\overline{\sigma_c^{38}}\phi - (\overline{\sigma_a^{39}}\phi + \lambda_{39})N_{Ar-39}(t) \quad (2.31)$$

$$\frac{dN_{Ar-41}(t)}{dt} = N_{0,40}\overline{\sigma_c^{40}}\phi - (\overline{\sigma_a^{41}}\phi + \lambda_{41})N_{Ar-41}(t) \quad (2.32)$$

$$\frac{dN_{Ar-42}(t)}{dt} = N_{Ar-41}(t)\overline{\sigma_c^{41}}\phi - (\overline{\sigma_a^{42}}\phi + \lambda_{42})N_{Ar-42}(t) \quad (2.33)$$

where

$\lambda$  is the decay constant and

$N_{0,xx}$  is the number of atoms of  $^{xx}\text{Ar}$ .

The solutions to the above activation equations are

$$N_{Ar-37}[t] = \frac{e^{-t(\lambda_{37} + \phi\overline{\sigma_a^{37}})}(\lambda_{37}N_{0,37} + \phi N_{0,37}\overline{\sigma_a^{37}} - \phi N_{0,36}\overline{\sigma_c^{36}} + e^{t(\lambda_{37} + \phi\overline{\sigma_a^{37}})}\phi N_{0,36}\overline{\sigma_c^{36}})}{\lambda_{37} + \phi\overline{\sigma_a^{37}}} \quad (2.34)$$

$$N_{Ar-39}[t] = \frac{e^{-t(\lambda_{39} + \phi\overline{\sigma_a^{39}})}(-\phi N_{0,38}\overline{\sigma_c^{38}} + e^{t(\lambda_{39} + \phi\overline{\sigma_a^{39}})}\phi N_{0,38}\overline{\sigma_c^{38}} + \lambda_{39}N_{0,39} + \phi\overline{\sigma_a^{39}}N_{0,39})}{\lambda_{39} + \phi\overline{\sigma_a^{39}}} \quad (2.35)$$

$$N_{Ar-41}[t] = -\frac{(-1 + e^{t(-\lambda_{41} - \phi\overline{\sigma_a^{41}})})\phi N_{0,40}\overline{\sigma_c^{40}}}{\lambda_{41} + \phi\overline{\sigma_a^{41}}} \quad (2.36)$$

$$N_{Ar-42}[t] = \frac{(\phi^2 N_{0,40} (-\lambda_{41} + e^{t(-\lambda_{42} - \phi\sigma_{a,42})}) \lambda_{41} + \lambda_{42} - e^{t(-\lambda_{41} - \phi\sigma_{a,41})}) \lambda_{42} - \phi\sigma_{a,41} + e^{t(-\lambda_{42} - \phi\sigma_{a,42})} \phi\sigma_{a,41} + \phi\sigma_{a,42} - e^{t(-\lambda_{41} - \phi\sigma_{a,41})} \phi\sigma_{a,42}) \sigma_{c,40} \sigma_{c,41}}{((\lambda_{41} + \phi\sigma_{a,41})(\lambda_{41} - \lambda_{42} + \phi\sigma_{a,41} - \phi\sigma_{a,42})(\lambda_{42} + \phi\sigma_{a,42}))} \quad (2.37)$$

It should be noted that the full absorption cross-sections were considered for the radioargon isotopes due to the considerable effect of interactions such as (n,p) and (n, $\alpha$ ).

In order to consider the amount of an isotope after a certain time after irradiation,  $t_d$ , can be expressed using the above equations and considering the decay.

$$N^X(t_d) = N^X(t = t_i) e^{-\lambda_X t_d} \quad (2.38)$$

#### 2.4.1 DECAY OF $^{42}\text{K}$ AND $^{42}\text{Ar}$

The detection of  $^{42}\text{Ar}$  is difficult because it emits only a beta-ray and an anti-neutrino when it decays to  $^{42}\text{K}$ .



The half-life of  $^{42}\text{Ar}$  is 32.9 years and decays with beta-ray with an average energy of 233 keV. In order to detect the presence of  $^{42}\text{Ar}$ , the decay of  $^{42}\text{K}$  will be monitored. Potassium-42 has a 12.36 hour half-life and beta decays and emits gamma-rays, with the energy and intensities shown in Table 2.3. The most prominent gamma-ray will be at 1524.7 keV, which is easily detected by an HPGe.

Table 2.3. Gamma-rays emitted during the beta decay of  $^{42}\text{K}$ .

Energy (keV)	Absolute Intensity
312.6	0.33629
586.87	0.00038
694.54	0.003254
899.43	0.051528
1022.78	0.020069
12227.66	0.00235
1524.7	18.08
1922.18	0.041222
2424.09	0.019888

#### 2.4.2 OTHER METHODS OF $^{42}\text{K}$ PRODUCTION

The possibility of  $^{41}\text{K}$  capturing a neutron is the other production mechanism of  $^{42}\text{K}$  in our system. The radiative capture cross-section of  $^{41}\text{K}$  is shown in Figure 2.9. Potassium-41 is produced in the system through the decay of  $^{41}\text{Ar}$ , which has half-life of 109.34 minutes and is the major product during natural argon gas irradiation. This production avenue is only available while the sample is being irradiated. Therefore, the baseline  $^{42}\text{K}$  activity after removal from the reactor can be measured and allows for the measurement of  $^{42}\text{K}$  produced from the decay of  $^{42}\text{Ar}$  only after irradiation has ended.

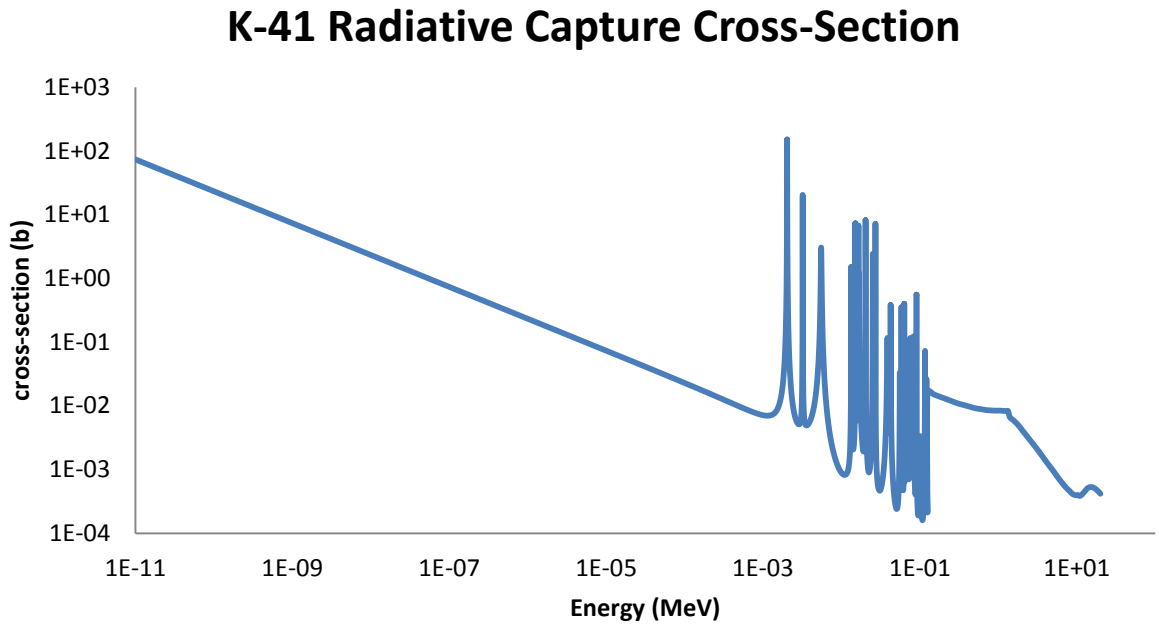


Figure 2.9. Radiative capture cross-section versus incident neutron energy for  $^{41}\text{K}$  (Santamarina *et al.*, 2009).

## 2.5 Argon cross-sections

The available cross-sections for the stable argon isotopes are well-known and readily available. The predominant cross-sections for stable argon isotopes are shown in Figure 2, Figure 2., and Figure 2. The cross-section libraries are from the most complete source within the JEFF 3.1A library maintained by the Nuclear Energy Agency. The cross-section libraries for the radioargon isotopes are conflicting and difficult to locate. The data provided in the JEFF 3.1A libraries are shown in Figure 2.11, Figure 2.13, Figure 2.15, and Figure 2.16. The other libraries appear to have very similar data to the JEFF 3.1A data for  $^{36}\text{Ar}$ , pictured in Figure 2.10 (JEFF 200).

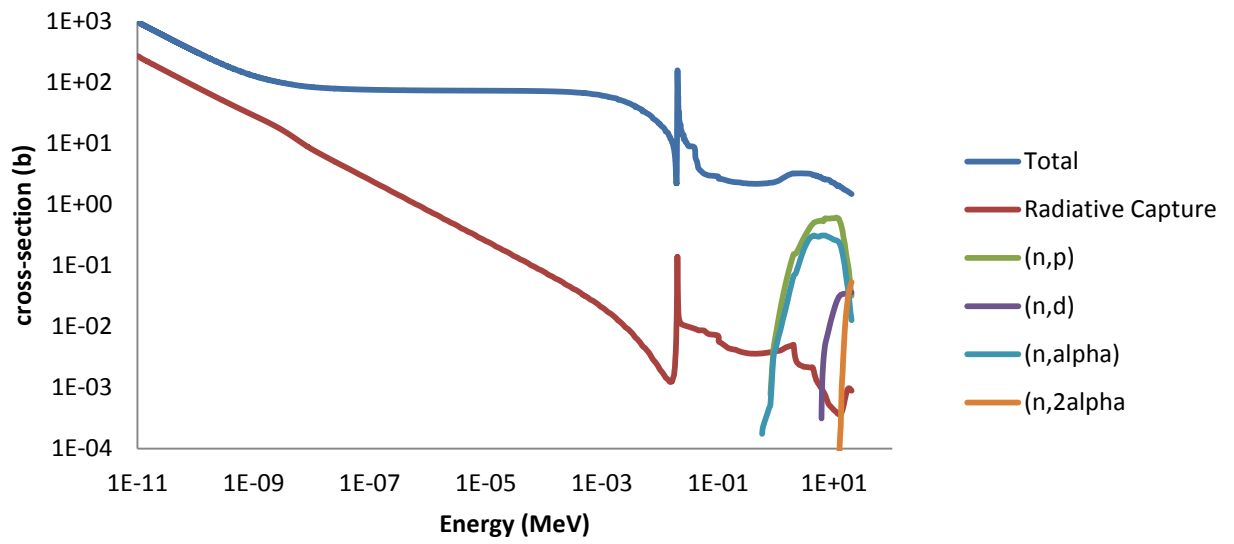


Figure 2.10.  $^{36}\text{Ar}$  cross-sections from JEFF 3.1 (Koning *et al.*, 2006).

The ROSFOND nuclear data library is similar in shape to the JEFF 3.1A cross-sections for  $^{37}\text{Ar}$ , shown in Figure (Koning *et al.*, 2006). The large (n,p) and (n, $\alpha$ ) cross-sections should be noted. The induced activity solutions were updated to include the absorption cross-sections, instead of just the radiative capture cross-section. The absorption cross-section of  $^{39}\text{Ar}$  also had a small contribution due to the (n, $\alpha$ ) pathway.

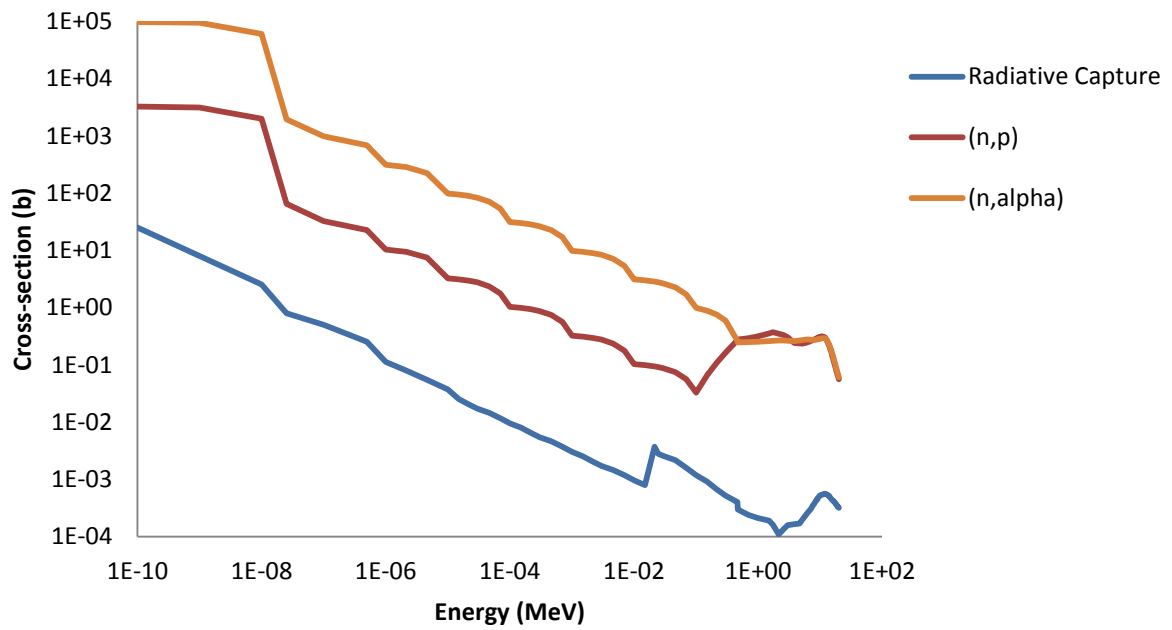


Figure 2.11. JEFF 3.1  $^{37}\text{Ar}$  cross-sections (Koning *et al.*, 2006).

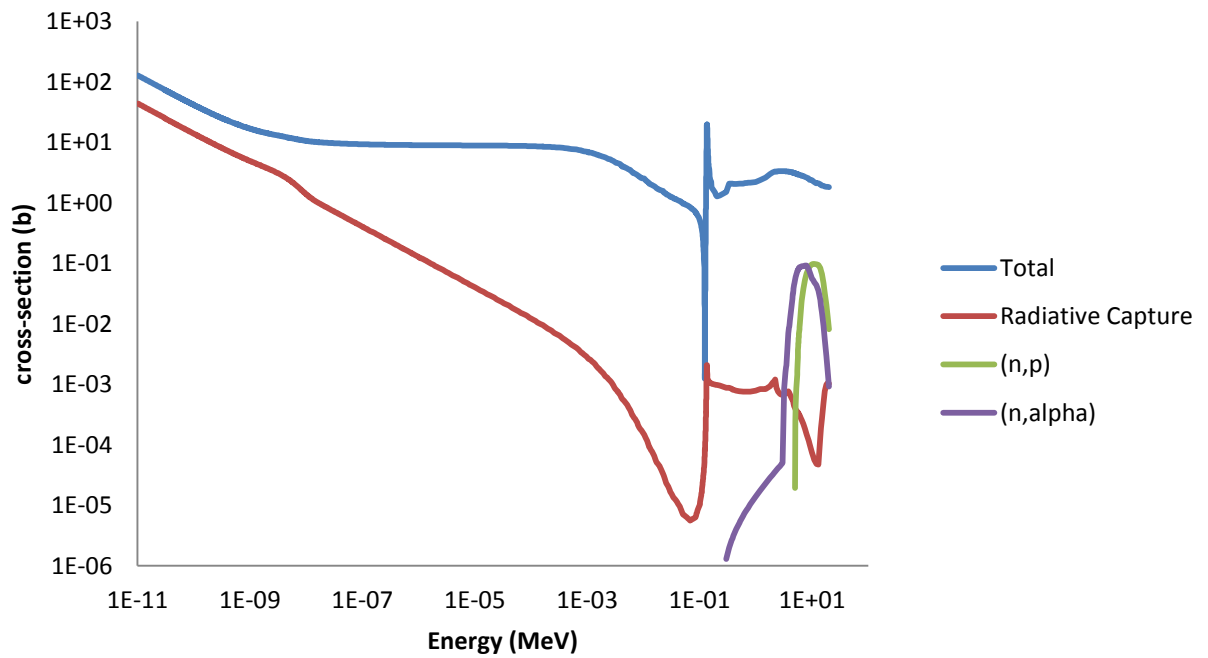


Figure 2.12. JEFF  $^{38}\text{Ar}$  cross-sections (Koning *et al.*, 2006).

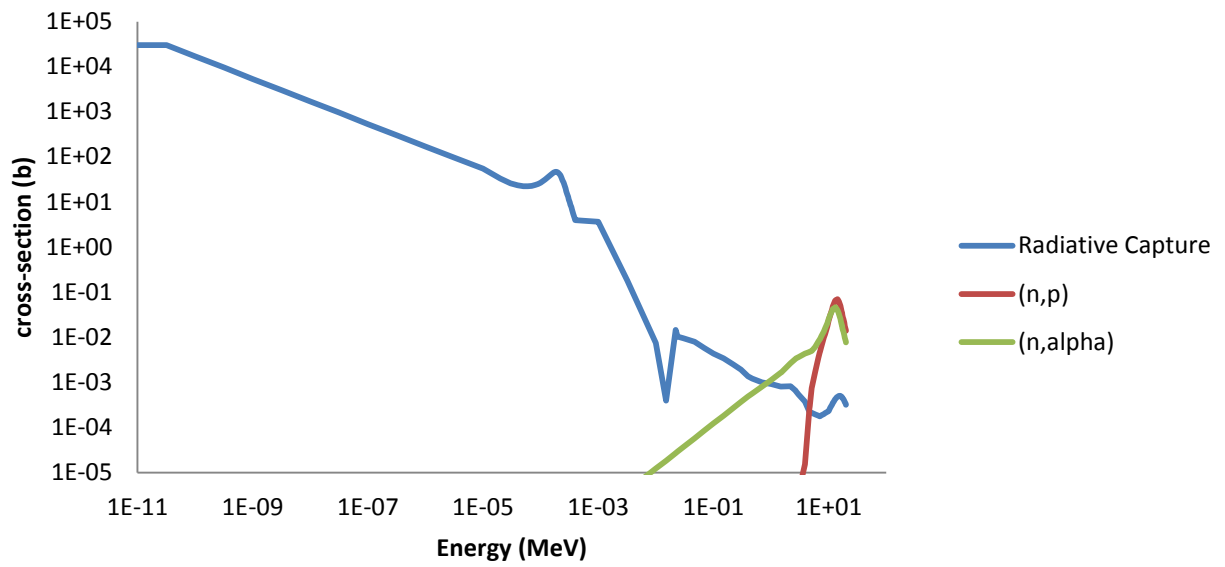


Figure 2.13. JEFF 3.1  $^{39}\text{Ar}$  cross-sections (Koning *et al.*, 2006).

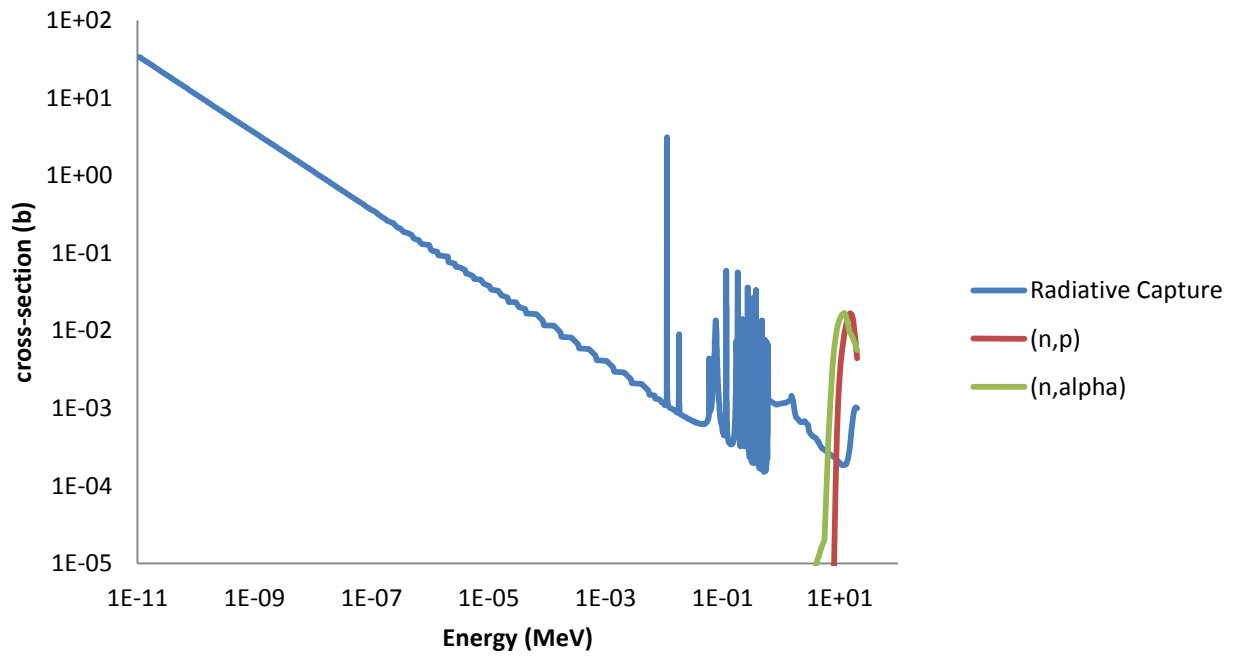


Figure 2.14. JEFF 3.1  $^{40}\text{Ar}$  cross-sections (Koning *et al.*, 2006).

The ROSFOND library, or any other nuclear data library, does not have any cross-sections for  $^{41}\text{Ar}$ . The CINDER90 library only has the radiative capture cross-section. The comparison of the two nuclear libraries is shown in Figure 2.15.

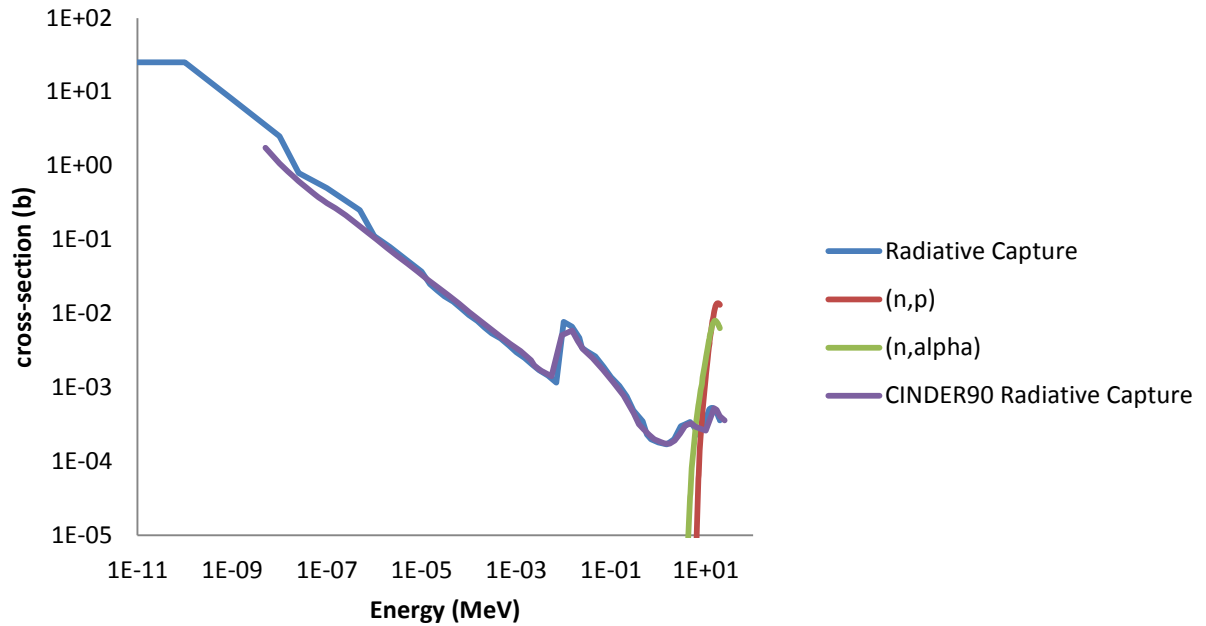


Figure 2.15.  $^{41}\text{Ar}$  cross-section libraries. The first three are JEFF 3.1 (Koning *et al.*, 2006) and the last is from CINDER90.

The ROSFOND (Zabrodskaya *et al.*, 2007) cross-sections match the  $^{42}\text{Ar}$  cross-section libraries provided in JEFF 3.1A (Koning *et al.*, 2006), shown in Figure 2.16.

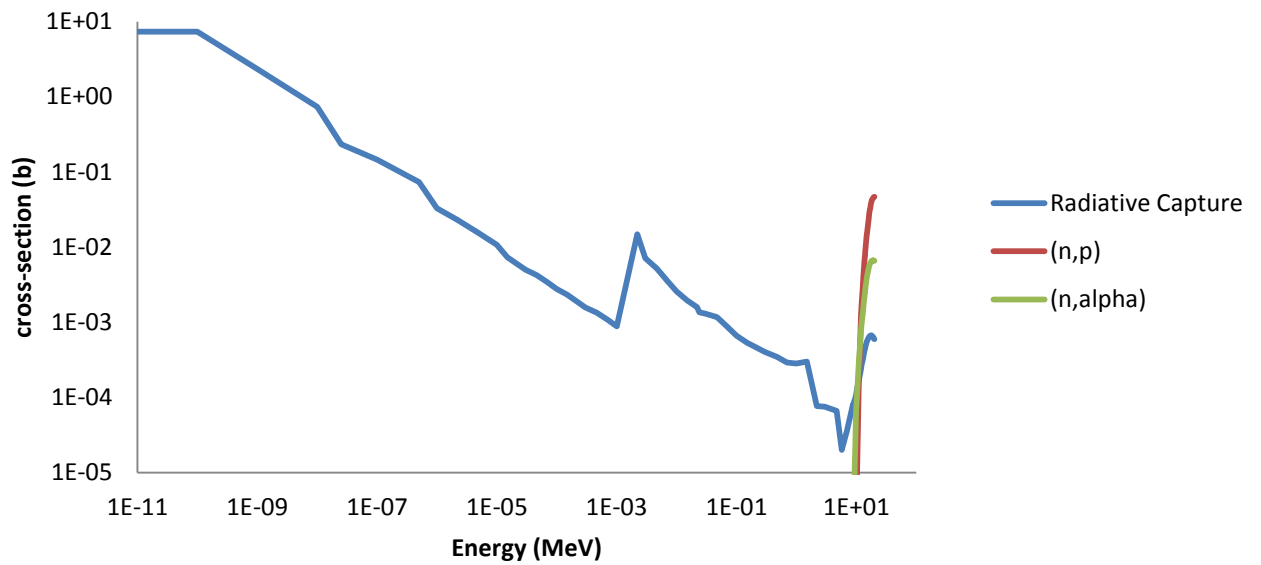


Figure 2.16. JEFF 3.1  $^{42}\text{Ar}$  cross-sections (Koning *et al.*, 2006).

The UT TRIGA MCNPX reactor model used to approximate radioargon production during the experiments of this project is coupled with the CINDER90 cross-section libraries. The stable argon isotopes in the CINDER90 libraries agree with the values in the JEFF 3.1A libraries. However, CINDER90 does not have any values for the  $^{44}\text{Ca}(n,\alpha)$  reaction or  $^{41}\text{Ar}$  reactions other than radiative capture.

## CHAPTER 3: REACTOR MODEL

The experiments completed used The University of Texas at Austin 1.1 MW TRIGA Mark II research reactor located on the J.J. Pickle Research Campus within the Nuclear Engineering Teaching Laboratory (NETL), shown in Figure 3.1. The current reactor configuration has 114 uranium zirconium hydride fuel rods with several in-core irradiation facilities—the 3L, central thimble, pneumatic system, and the rotary specimen rack—and five beam ports for external neutron experiments.

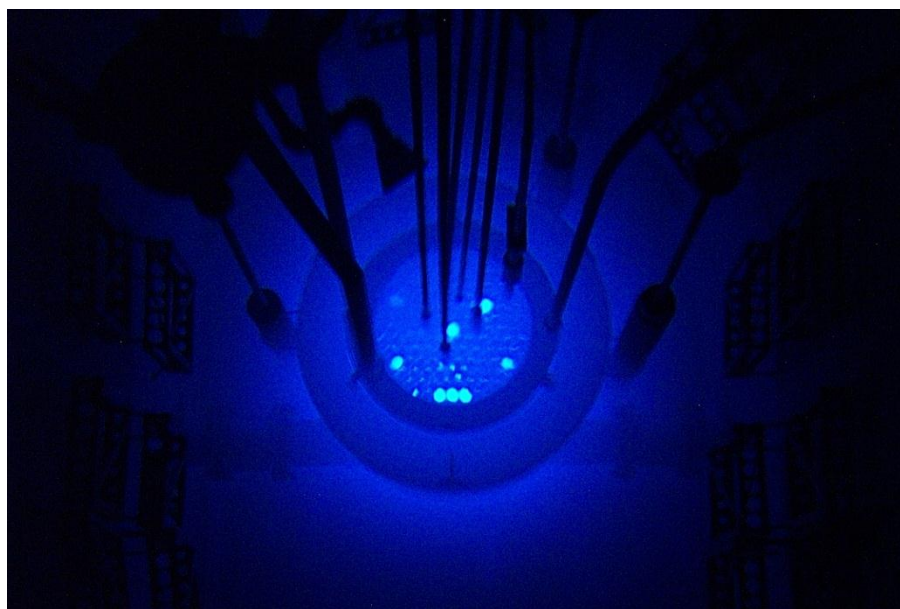


Figure 3.1. The University of Texas at Austin 1.1 MW TRIGA Mark II research reactor core during a pulse.

All of the samples for this project were irradiated in the three-element (3L) facility within the reactor core. The 3L facility takes up positions E11, F13, and F14 in the current core configuration, as shown in Figure 3.2. A 6061 Al canister with a liner was used for all of the irradiations. The liner is either lead or cadmium. The lead liner is

used as a ballast due to the large empty volume within the Al canister. The Cd liner prevents 95% of the thermal neutrons to pass through. This allows for the irradiation to mainly include activations by epithermal and fast neutrons. The lead liner was used for the natural argon gas irradiations because the thermal neutrons were the optimal energy level to interact with the stable argon isotopes. In order to minimize unnecessary thermal activations, the Cd liner was used during the CaO irradiation.

The procedure utilized for small volume gas irradiation using a Teflon valve is based on the methodology originally developed for radioxenon production (Haas *et al.*, 2009). The 3L facility was slightly altered to allow the irradiation of a much larger volume of gas for some of the other experiments.

Due to the lack of gamma-ray emission during the decay of the longer-lived radioargon isotopes, a computation method to calculate the induced activity of the radioargon isotopes of interest was necessary. The original  $^{37}\text{Ar}/^{41}\text{Ar}$  production ratios were approximated by the WISE Uranium Project (“WISE” 2011). This method was only used as a simple approximation for original activity calculations necessary before the experiment and to estimate the time window for shipping the radioargon samples.

In order to reduce the error in the induced  $^{37}\text{Ar}$  activity, the calculated production ratio was improved using a neutron flux profile generated by a slightly altered MCNPX UT TRIGA reactor model developed by Braisted (2008) and the CINDER90 cross-section libraries. The full MCNP reactor deck is in Appendix D. A top-view of the reactor core is shown in Figure 3.2, which shows the location of the 3L facilities within the reactor core.

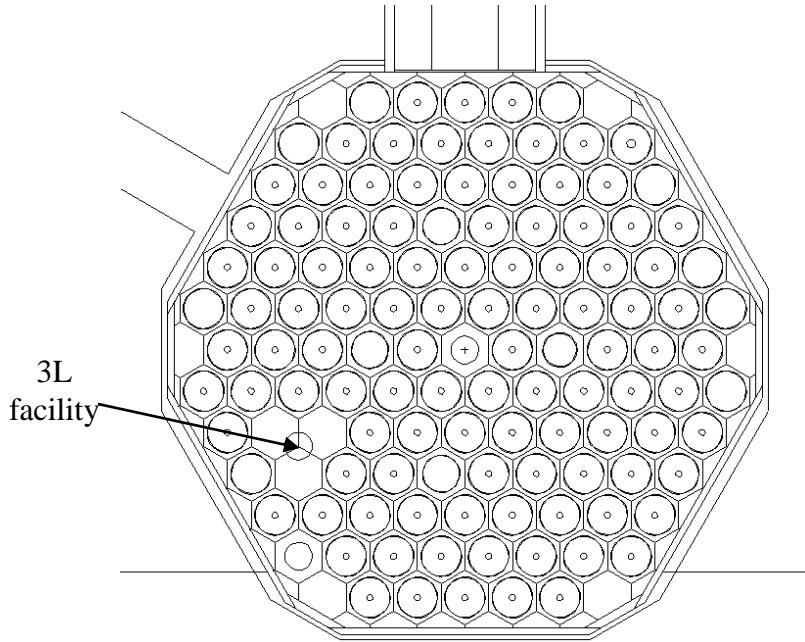


Figure 3.2. The MARK II TRIGA reactor MCNPX model shown from above. The 3L irradiation facility used in this experiment is indicated.

### 3.1 MCNPX

MCNPX is a Monte Carlo (MC) radiation transport code which tracks the transport of neutron and gamma-rays, or neutral particles (NP). The code was developed and is updated at Los Alamos National Laboratory in New Mexico. This model used MCNPX—Version 2.7C.

The most frequently used tallies for this model are the F4 and F5 tally. The f4 tally gives the average flux in a cell ( $\#/cm^2$ ). This tally represents the sum of the weight of the particle times the track-length divided by the cell volume. Therefore, it can be represented as

$$F4 = \frac{1}{V} \int_V dV \int_E dE \int_{4\pi} d\Omega \Phi(\mathbf{r}, E, \boldsymbol{\Omega}) \quad (3.1)$$

where the letters in bold represent vectors. The F5 tally gives the flux at a point or a ring ( $\#/cm^2$ ). There is a collided and uncollided flux profile generated.

The UT TRIGA MCNPX model was used to generate 63-group energy-distributed neutron flux profile for each of the different experimental set-ups. For the small volume gas irradiation using the Teflon vial, a point tally (f5) in the 3L placed 1.5” above the bottom of the irradiation canister with the lead liner was used. A volume tally (f4) was used to create a neutron flux profile for the entire 3L canister using the lead liner to approximate the large volume gas irradiation procedure. A point tally (f5) in the 3L placed 1.5” above the bottom of the irradiation canister with the Cd liner was used to approximate the representative flux during the CaO irradiation. There were also Co-Al wires irradiated at various power levels and during the CaO irradiation to benchmark the total fluence during the experiments. The MCNPX point tally output comparing the point tally within the 3L (using both the lead and cadmium liner), the RSR, the central thimble facility, and the center point of a fuel element is shown in Figure 3.3Figure .

## UT TRIGA Reactor Flux Profiles

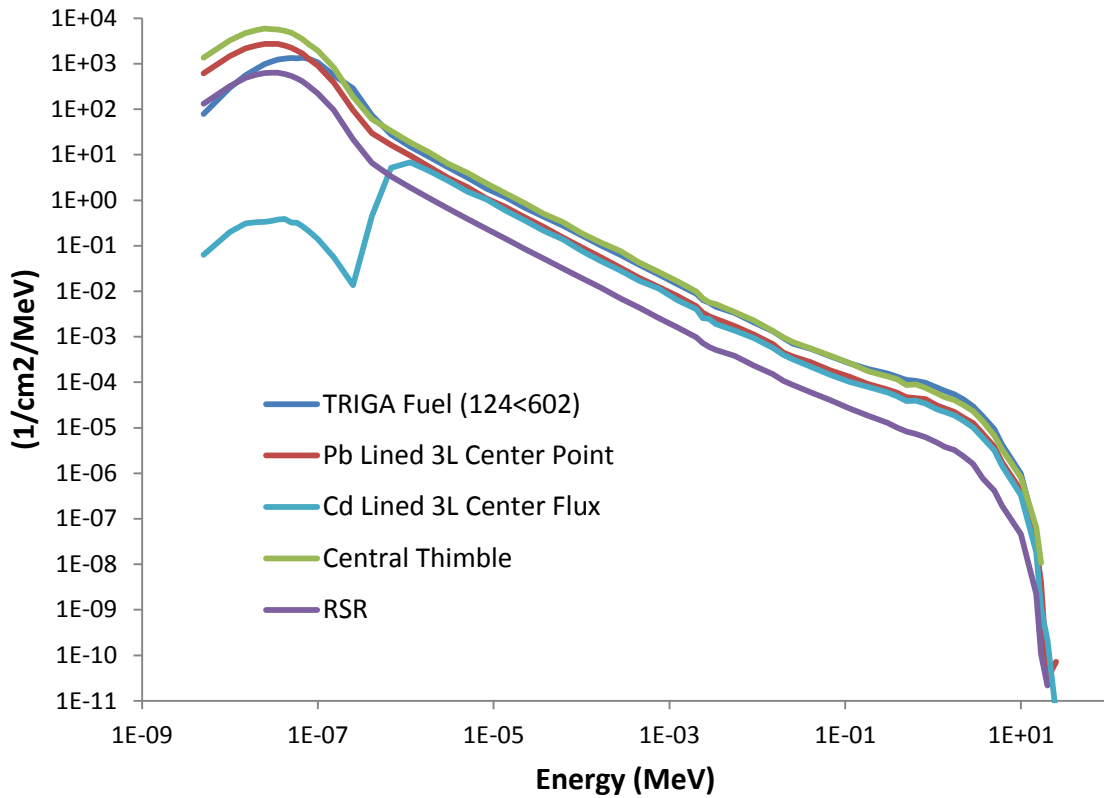


Figure 3.3. The flux profile of five different positions generated by the MCNPX model of the TRIGA core.

The CINDER90 cross-section libraries were used in conjunction with the neutron flux profile to create a collapsed cross-section for the radioisotopes of interest in a specific experimental design. For the notation in the paper, the energy collapsed cross-sections is indicated with a bar. Therefore,

$$\bar{\sigma} = \frac{\sum_{i=1}^{63} \sigma_i \phi_i}{\sum_{j=1}^{63} \phi_j} \quad (3.2)$$

Using the solution of the Bateman equations derived in the Theory section, the activity of radioisotopes of interest were approximated throughout the irradiation and

decay within the experiment assuming a steady irradiation level and the using the collapsed cross-section.

### **3.2 Characterization of the 3L irradiation facility**

In order to benchmark the output of the MCNP model, the irradiation of standard reference material at various powers and in two facilities (lead and cadmium-lined 3L canisters). NIST SRM 953 Co-Al wire was used. The Co-Al wire was used to experimentally calculate the flux at the same point in the irradiation canister that the gas valves and quartz tube were placed.

#### **3.2.1 CO-AL WIRES**

NIST SRM 953, neutron density monitor wire, with 0.1% by weight of cobalt in aluminum was irradiated for 1 hour at 500 kW, 300 kW, and 100 kW in the lead and cadmium-lined 3L canisters. There were also several pieces of SRM 953 wire irradiated at 950 kW; one for one hour and one for 30 minutes. The mass and spectrum data of each sample is listed in Table 3.1.

Table 3.1. The irradiation of SRM 953 samples at different power levels. Each sample was counted for a live time of 43,200 seconds within a few days of irradiation.

Power	Irradiation Time (min)	Mass (g)	Irradiation Facility	Counts at 1173.237 keV peak	Counts at 1332.501 keV peak
500 kW	60	0.01022	Pb	38198±207	34616±189
500 kW	60	0.01190	Cd	3251±80	3081±66
300 kW	60	0.01171	Pb	24275±241	21710±187
300 kW	60	0.1125	Cd	1924±53	1698±46
100 kW	60	0.01228	Pb	8628±108	7691±95
100 kW	60	0.01242	Cd	811±90	792±60

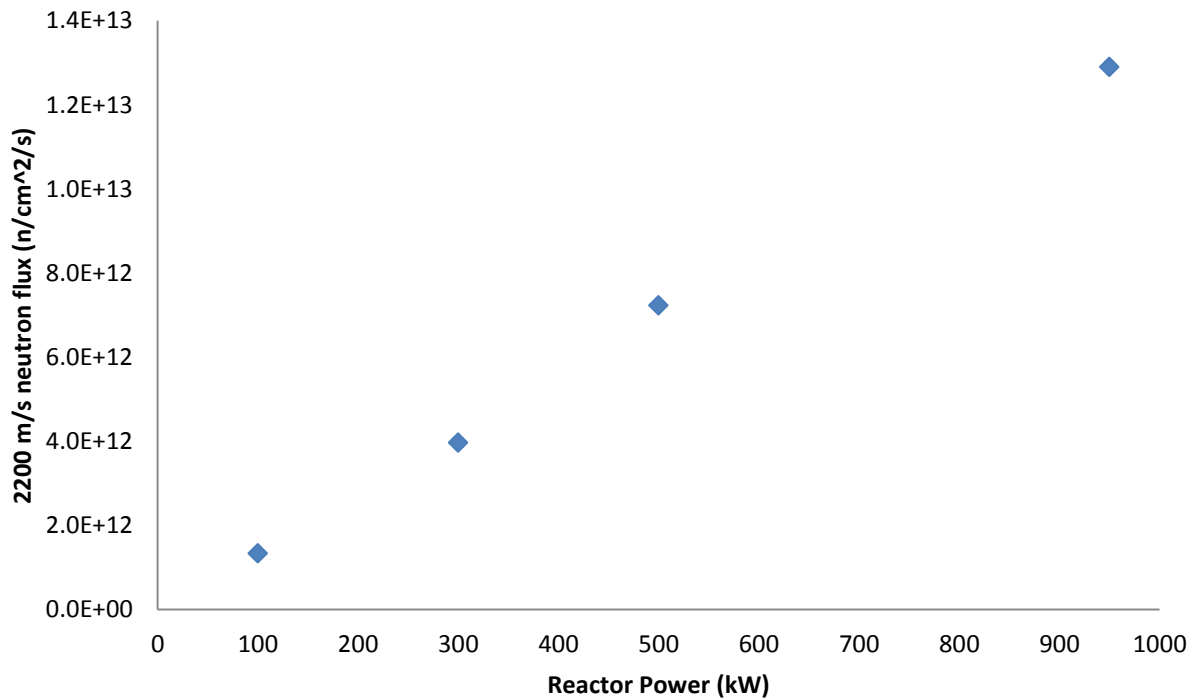


Figure 3.4. The 2200 m/s neutron flux in the lead-lined 3L.

### 3.3 Modeled Production Experiments

The wire and foil irradiations provided a flux benchmark for all of the reactor model calculations. In several of the radioargon production experiments, a Co-Al wire was run with the sample to calculate a flux that was used during a production experiment. This created an overlap of wire irradiations at certain power levels. As expected, the flux was relatively similar based on the power level.

The UT TRIGA model provided a 63 group energy distributed flux profile at separate points in the reactor. For the  $^{37}\text{Ar}$  production, the point tally was placed 1.5" above the bottom of the 3L irradiation canister. The 3L facility does have a 1" spacer that stays in the reactor. There is an additional spacer to be used in the 3L irradiation canister, so the sample can reach the peak flux in the reactor. This option was not used for the Teflon valve irradiations because of issues with embrittlement. The CaO irradiation did not use the inside spacer either. For the large volume irradiation procedure, a volume tally was used for the entire 1.4 L volume to calculate the fluence through the irradiation period.

## CHAPTER 4: <sup>37</sup>AR PRODUCTION

The major thrust of the project was the production of <sup>37</sup>Ar through two methods—the irradiation of natural argon and the irradiation of calcium-containing compounds. The third option of irradiating enriched <sup>36</sup>Ar gas was not used due to the low activities of <sup>37</sup>Ar required by the follow-up experiments. However, the production activities of <sup>37</sup>Ar through the irradiation of enriched <sup>36</sup>Ar gas using the large volume gas irradiation procedure are calculated using the UT TRIGA MCNPX model in the Large Volume Irradiation Procedure section.

The irradiation of small amounts of natural argon gas provided a small sample of <sup>37</sup>Ar after the dominant radioargon isotope <sup>41</sup>Ar decayed away. For medium-scale <sup>37</sup>Ar production, the irradiation of enriched <sup>36</sup>Ar gas provides a single-step process with minimal waste streams produced. However, the large (n,p) and (n,α) reaction cross-section of <sup>37</sup>Ar must be considered when calculating the production rates of <sup>37</sup>Ar. The previous large scale production of <sup>37</sup>Ar has been done through the irradiation of calcium-containing compounds in fast reactors due to the size constraints of the in-core irradiation facilities and the plans for long term irradiation during the normal operating schedule.

### 4.1 Irradiation of Natural Argon

The irradiation of natural argon gas creates several radioargon isotopes. The isotopic composition of natural argon is 99.6003% <sup>40</sup>Ar, 0.0632% <sup>38</sup>Ar, and 0.3365% <sup>36</sup>Ar. The predominant radioargon isotope created is <sup>41</sup>Ar through radiative capture of a neutron by <sup>40</sup>Ar. <sup>41</sup>Ar decays by beta decay to <sup>41</sup>K and emits a gamma ray. With a half-

life of 109.34 minutes, the  $^{41}\text{Ar}$  produced during the irradiation is allowed to decay before the shipment and use of the  $^{37}\text{Ar}$  to minimize exposure.  $^{37}\text{Ar}$  decays via electron capture to  $^{37}\text{Cl}$  without the release of a gamma-ray;  $^{39}\text{Ar}$  decays via beta decay to  $^{39}\text{K}$  with no gamma-ray released. Therefore, the only gamma-ray emission detectable with an HPGe is the decay of  $^{41}\text{Ar}$ . With a half-life of 109.34 minutes, the  $^{41}\text{Ar}$  produced during the irradiation is allowed to decay before the shipment and use of the  $^{37}\text{Ar}$  to minimize exposure.

The amount of  $^{37}\text{Ar}$  produced is calculated by measuring the amount of  $^{41}\text{Ar}$  present in the sample at the time of removal. The activity of  $^{41}\text{Ar}$  while the sample is being counted is calculated by

$$A_{41}(t = t_d) = \frac{C}{t_c \epsilon \gamma_i} \quad (4.1)$$

where

$A_{41}$  is the activity of the  $^{41}\text{Ar}$  produced during the irradiation

$t_d$  is the decay time or time elapsed after the end of the irradiation

$C$  is the counts in the peak area of the  $^{41}\text{Ar}$  decay peak at 1293.587 keV

$t_c$  is the count time

$\epsilon$  is the detector efficiency at 1293.587 keV

$\gamma_i$  is the gamma yield of the 1293.587 keV gamma-ray, which is 99.1%

After the activity of  $^{41}\text{Ar}$  at the count time is established the activity is calculated from the removal from the reactor.

$$A_{41}(t = t_i) = \frac{A_{41}(t=t_d)}{e^{-\lambda_{Ar-41}t_d}} \quad (4.2)$$

where

$A_{41}(t=t_i)$  is the  $^{41}\text{Ar}$  activity when the irradiation ended.

The production ratio of  $^{37}\text{Ar}/^{41}\text{Ar}$  ( $P_{37-41}$ ) was calculated using the 63-group energy-dependent cross-sections of the two isotopes with respect to the flux profile generated by the MCNPX reactor model. The activity of the  $^{37}\text{Ar}$  of the sample,  $A_{37}(t)$ , is

$$A_{37}(t) = A_{37}(t = t_i)e^{-\lambda_{Ar-37}t} = A_{41}(t = t_i)P_{37-41}e^{-\lambda_{Ar-37}t} \quad (4.3)$$

where

$A_{37}(t=t_i)$  is the activity of  $^{37}\text{Ar}$  at the end of the irradiation period

$t$  is the time elapsed from the end of the irradiation period to the time the activity is being calculated.

#### 4.1.1 EXPERIMENTAL SET-UP

Natural argon gas is irradiated in a Swagelok 43 series PFA Teflon plug valve, shown in Figure 4.1. The large knob is on during the filling of the valve, but is removed prior to placement into the aluminum irradiation canister due to size restrictions. The volume of the plug valve was measured to be  $0.580 \pm 0.050$  cc.



Figure 4.1. Swagelok 43 series PFA Teflon plug valve.

The Teflon valve is filled with natural argon gas (99.9999%) using a gas manifold shown in Figure 4.2. The Teflon valve is attached to the manifold at the bottom right (blue and white valve pictured in Figure 4.1) and is opened. The knob leading to the scientific grade natural argon gas canister is opened to the manifold and the diaphragm valve attached to the natural argon canister, shown in Figure 4.3, is opened slightly. The manifold is filled with argon gas to about room pressure, shown by the pressure sensors noted in Figure 4.2. The knob leading to the argon gas canister is closed and the knob leading to the vacuum line is opened. The rough pump is turned on the manifold is pumped down and then the high vacuum is turned on and allowed to pump down as low as possible (about 0.115 mTorr). The vacuum line is closed and the manifold is filled again. The manifold and valve are filled and pumped down five times before the valve is filled for irradiation. This procedure is used to minimize contamination in the sample. The valve is filled to approximately 760 Torr.

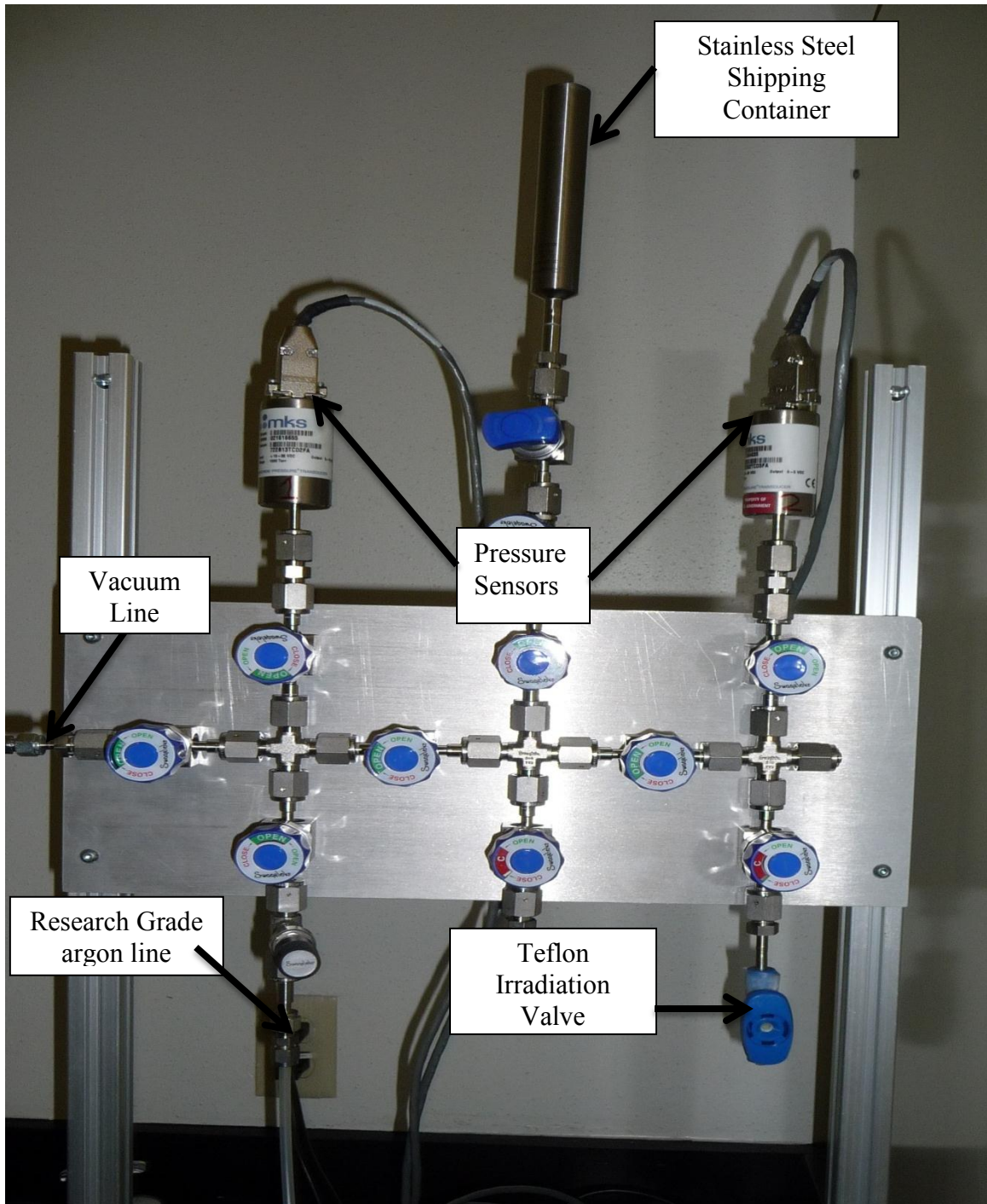


Figure 4.2. Gas manifold used to transfer argon for small volume irradiation experiments.



Figure 4.3. The diaphragm valve attached to the scientific grade natural argon gas canister.

The argon-filled valve, with the knob removed, is placed in an aluminum canister and placed into the 3L irradiation facility within the reactor, shown in Figure 4.4. The irradiation mainly yields three radioargon isotopes— $^{37}\text{Ar}$ ,  $^{39}\text{Ar}$ , and  $^{41}\text{Ar}$ . The irradiation periods are typically 1 to 3 hours long. The reactor power is between 100 and 500 kW in order to minimize embrittlement of the Teflon valve. During the course of the experiment, there were several samples that were lost due to the cracking of the Teflon valve while it was being fastened to the gas manifold.



Figure 4.4. The aluminum 3L irradiation canister.

After irradiation, the procedure dictates a cooling period of at least 24 hours and is followed by counting the  $^{41}\text{Ar}$  in the Teflon valve. Therefore, the exposure due to the release of the remaining  $^{41}\text{Ar}$  upon breaking a valve is minimal and substantially smaller than the activation of the air in the reactor bay due to the beam-port experiments.

After the irradiation, the irradiated gas is counted while still in the Teflon valve. The irradiated argon gas is then transferred from the Teflon valve to a stainless steel container using the gas manifold shown in Figure 4.2. The stainless steel container is attached to the center-top valve between the two pressure sensors. The Teflon valve is attached to the bottom-right valve, as shown in Figure 4.2. The system and stainless steel shipping container is filled and pumped down four times. The knobs leading to unnecessary lines—the vacuum pump, the argon gas line, and one of the pressure sensors—are closed to minimize the volume manifold before opening the Teflon valve. The Teflon valve containing the irradiated argon gas is opened and the gas is allowed to move freely into the stainless steel shipping container. The pressure of the system is noted.

After the transfer, the stainless steel canister is counted and compared to the original Teflon valve count to calculate the transfer efficiency. The sample is counted using the HPGe at beam port 3 while the reactor is not running. The stainless steel canister provides more of a line than a point source for counting. Therefore, the detector efficiency along the line was approximated by calculating the efficiency of the detector at different points using a  $^{152}\text{Eu}$  check source and averaging over the length of the gas sample within the stainless steel container. There is also error introduced into the system

because the placement of the stainless steel cylinder is only estimated. However, this error is negligible in comparison to the production ratio problems brought on by the inconclusive radioargon cross-section libraries.

#### **4.1.2 PROCEDURE**

1. The metal parts on the Swagelok Teflon valve should be removed. The large blue screw should be removed and the knob should be pulled off. Reattach only the knob.
2. Both the stainless steel shipping container (SC) and the Teflon valve (TV) are attached to the transfer system in the positions shown in Figure 4.5.
3. The vacuum should be turned on and the components should be positioned as shown in the “Establish a high vacuum” row in Table 4.1. Allow the system to pump down as close to 0 Torr as possible. This should take about 5 minutes.
4. Close D4 and wait 5 minutes. If the pressure increased more than 0.3 Torr/s over a 2 minute period, the system will need to be leak checked and connections will have to be tightened. When there are no leaks in the system, D4 can be reopened.
5. Arrange the valves as shown in the “Fill system” row in Table 4.1.
6. Allow the pressure in the system to reach approximately 740 Torr as indicated by the pressure sensors (P1, P2).
7. Close D7 and B. Open D4. Wait about 10 minutes until the pressure drops to approximately 0 Torr.
8. Arrange the valves as shown in the “Establish a high vacuum” row in Table 4.1. Allow the system to fill to approximately 740 Torr.

9. Repeat steps 6 and 7 five times.
10. Record the pressure of the system from P2. Close all valves and remove the Teflon valve for irradiation.
11. Remove the knob from the Teflon valve for irradiation. Place near the system for use during the gas transfer process.
12. Irradiate the Teflon valve at a power level between 100-500 kW for up to 2 hours in the lead-lined 3L irradiation facility depending on the desired  $^{37}\text{Ar}$  activity.
13. Allow the sample to cool in the 3L canister either in the reactor or in the cooling rack on the side. The cooling time is dependent on the irradiation time and power.
14. Remove the sample from the 3L and count the sample using an HPGe detector.
15. After the counting irradiated sample and Teflon valve, replace the knob on the Teflon valve. Attach the Teflon valve to the transfer system. Keep the Teflon valve closed until the protocol indicates.
16. Turn off the vacuum. Arrange the valves indicated in the “Transfer” row in Table 4.1. Record the pressure indicated on P2.
17. Close all valves. Remove stainless steel shipping container.
18. The system should be allowed to sit for a few days because there will be lingering radioargon isotopes, specifically  $^{41}\text{Ar}$ .
19. Use a HPGe detector to count the irradiated gas in now in the stainless steel shipping container. Depending on the activity, the health physicist will decide the shipping date.

20. After a few days of decay, arrange all of the components as described in the “Establish a high vacuum” row in Table 4.1. Allow the system to pump down to approximately 0 Torr with the high vacuum venting into a fume hood.
21. Arrange the components as described in “Fill system without sample” row in Table 4.1 Allow the system to fill to approximately 740 Torr.
22. Repeat steps 20 and 21 five times.
23. Close all valves and turn off argon gas and the vacuum.

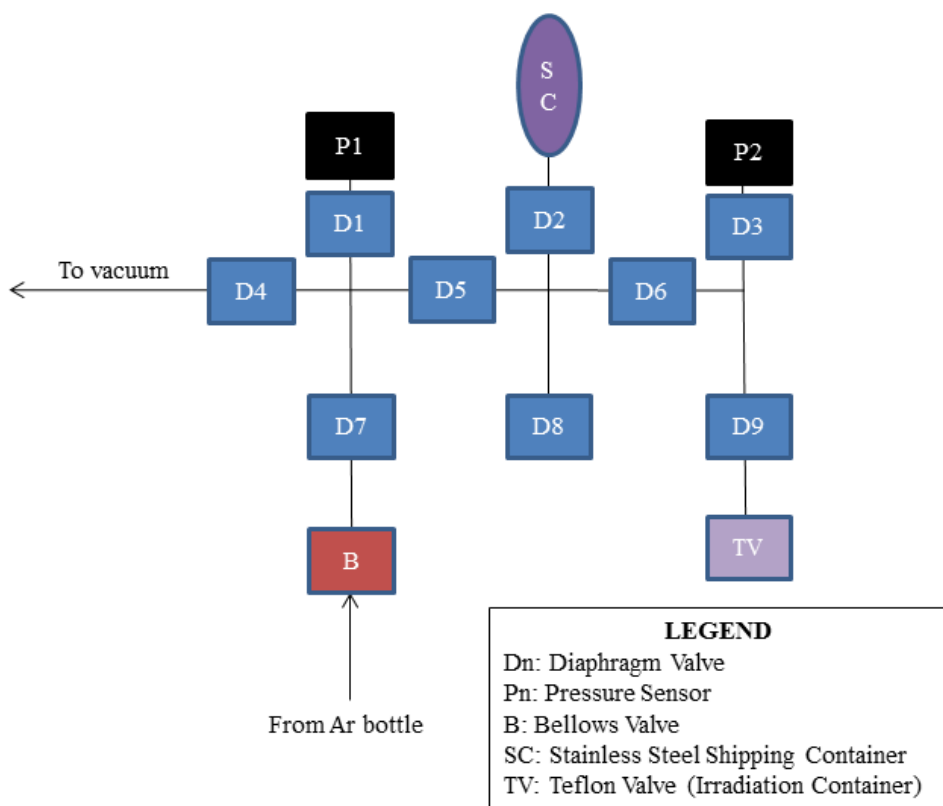


Figure 4.5. The schematic of the gas transfer system for this experiment with numbered and labeled components.

Table 4.1. The gas transfer system components labeled as indicated in the legend of Figure 4.5. 0 indicated off or closed. 1 indicated on or open.

Action	D1	D2	D3	D4	D5	D6	D7	D8	D9	B	Ar	SC	TV	V
Establish a high vacuum	1	1	1	1	1	1	0	0	1	0	0	1	1	1
Fill system	1	1	1	0	1	1	1	0	1	1	1	1	1	0
Transfer	0	1	1	0	0	1	0	0	1	0	0	1	1	0
Fill system without sample	1	0	1	0	1	1	1	0	0	1	1	-	-	1

### 4.1.3 RESULTS

The counting of the radioargon sample in the stainless steel canister is counted at the HPGe within the beam port 3 shielding while the reactor is not running. The 0.18±0.18 cm thick stainless steel with an attenuation coefficient of 0.0527±0.00002 cm<sup>2</sup> g<sup>-1</sup> and a density of 7.97±0.03 g cm<sup>-3</sup> has an attenuation of 0.927±0.0070. With a 2 hour irradiation period and a decay time of 16253 s, the <sup>41</sup>Ar activity at the start of the count was 1.31956x10<sup>6</sup> ± 5.29 x10<sup>4</sup> Bq including the adjustment for attenuation due to the stainless steel container. The <sup>41</sup>Ar activity was 7.32x10<sup>6</sup>±3.25x10<sup>4</sup> Bq. The <sup>41</sup>Ar/<sup>37</sup>Ar production ratio of 3.54x10<sup>5</sup> for a 2 hour irradiation is an order of magnitude higher than originally anticipated due to originally ignoring the large (n,p) and (n,α) reaction cross-sections for <sup>37</sup>Ar. Therefore, there is an expected 20.66±2.068 Bq activity of <sup>37</sup>Ar at the end of the irradiation. The error assumes a 10% error in the production ratio. The production ratio of <sup>41</sup>Ar/<sup>39</sup>Ar of 1.185x10<sup>9</sup> is very close to the initial estimation. The calculated production activity of <sup>39</sup>Ar is 6.17±0.618 mBq.

The <sup>41</sup>Ar/<sup>xx</sup>Ar production ratios vary with time due to the comparatively shorter half-life of <sup>41</sup>Ar, 109.34 min. The <sup>41</sup>Ar/<sup>42</sup>Ar production ratio is interesting because <sup>42</sup>Ar

production is based on the concentration of  $^{41}\text{Ar}$ . The radioargon production ratios are shown in Figure 4.6, Figure 4.7, and Figure 4.8.

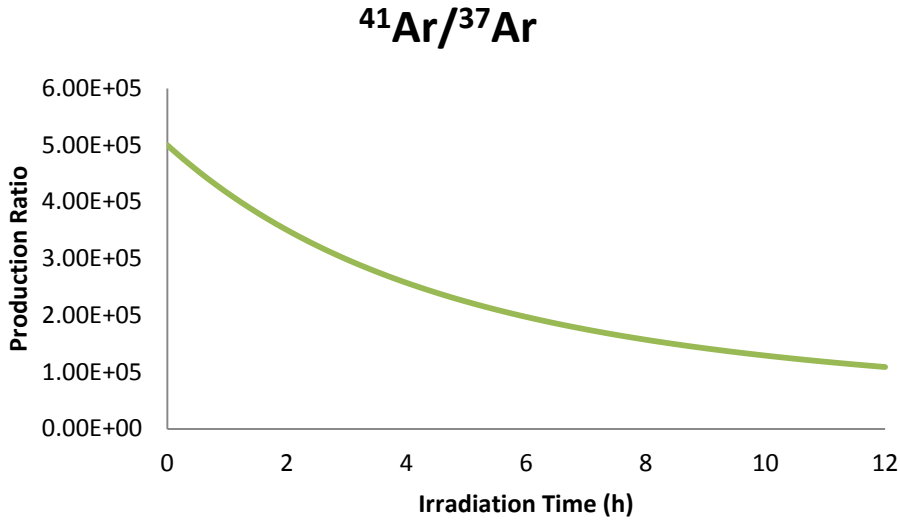


Figure 4.6. The  $^{41}\text{Ar}$  to  $^{37}\text{Ar}$  production ratio based on irradiation time.

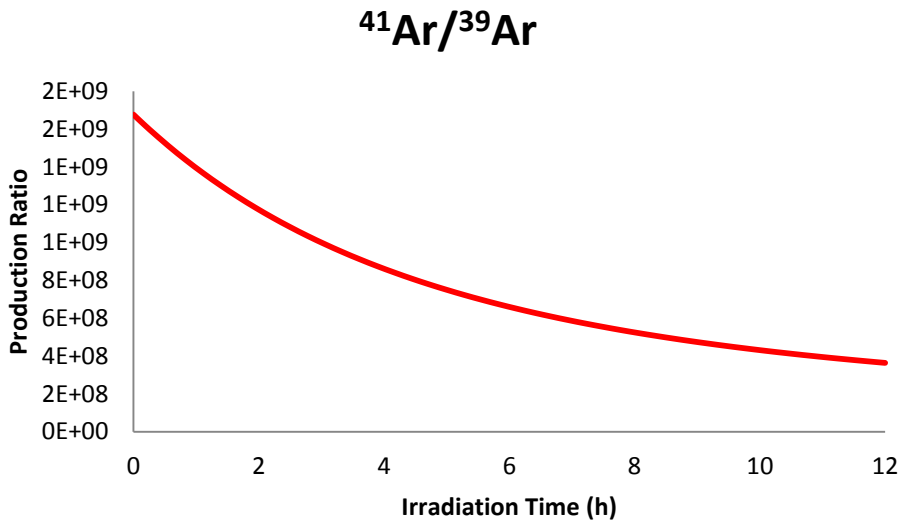


Figure 4.7. The  $^{41}\text{Ar}$  to  $^{39}\text{Ar}$  production ratio based on irradiation time.

## $^{41}\text{Ar}/^{42}\text{Ar}$

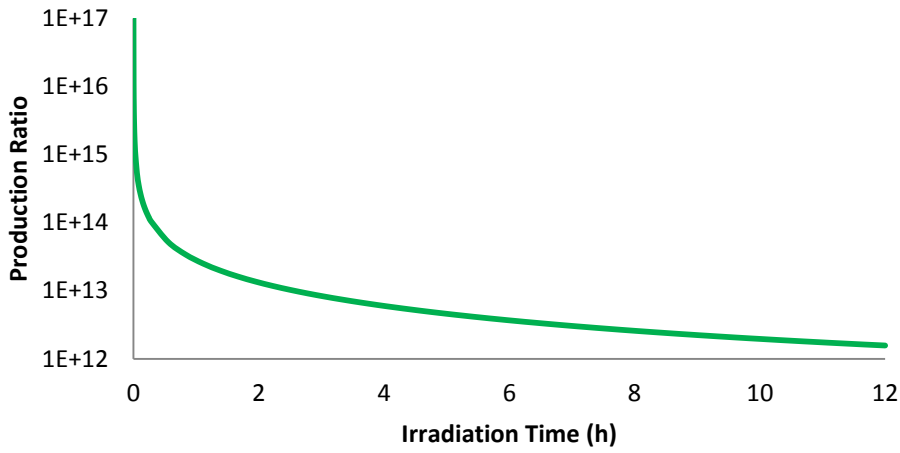


Figure 4.8. The  $^{41}\text{Ar}$  to  $^{42}\text{Ar}$  production ratio based on irradiation time.

The exposure rate in mR/hr at 1 foot resulting from natural argon irradiation is shown in Figure 4.7. The only radioargon isotope to contribute to the exposure rate is  $^{41}\text{Ar}$ . As  $^{41}\text{Ar}$  beta decays to  $^{41}\text{K}$ , it releases a 1293.587 keV gamma-ray with 99.1% intensity and a 1677.198 keV gamma-ray with 0.052% intensity. The  $^{41}\text{Ar}$  1293.587 keV gamma-ray contributes nearly 100% to the total exposure and there is no perceivable difference between the  $^{41}\text{Ar}$  1293 keV gamma-ray exposure rate and the total exposure rate, shown in Figure 4.9.

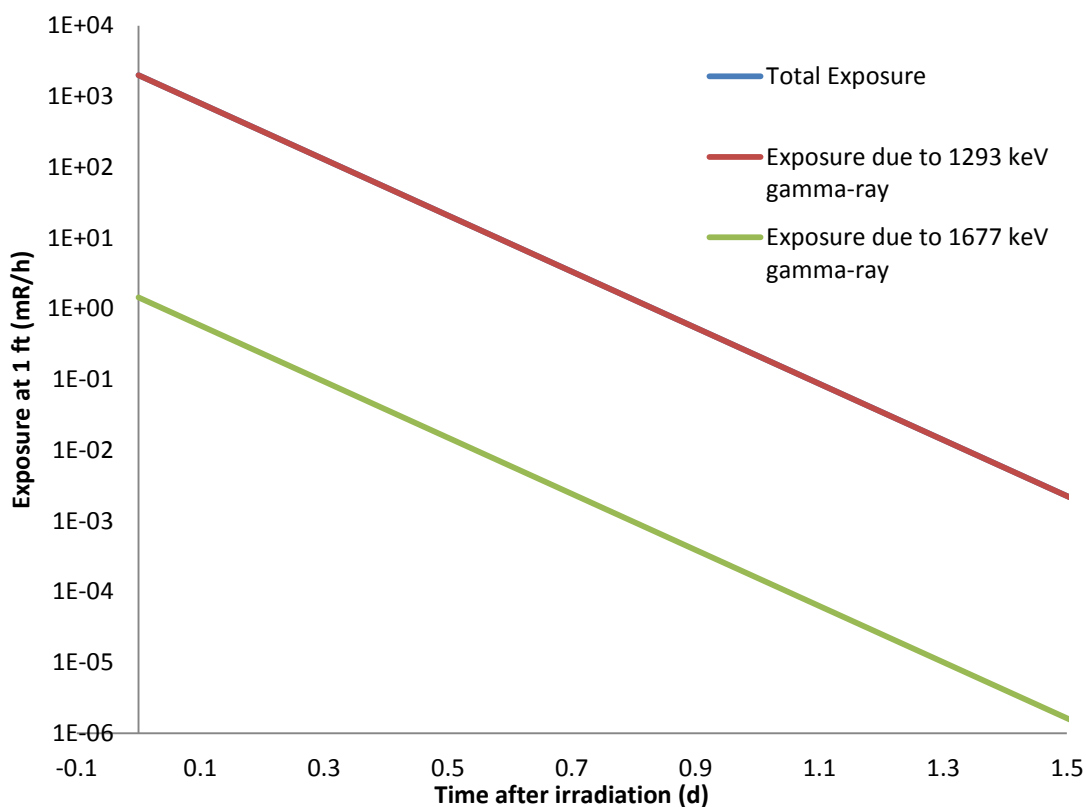


Figure 4.9. The exposure rate due to the  $^{41}\text{Ar}$ .

## 4.2 Irradiation of calcium-containing compounds

The major production pathway for large-activity  $^{37}\text{Ar}$  samples has been the irradiation of solid calcium-containing compounds. The  $^{40}\text{Ca}(n,\alpha)^{37}\text{Ar}$  pathway provides a sample with limited competing radioargon isotopes. However, the threshold for this reaction is 0.5 MeV and is not the optimal pathway to rely on with a thermal reactor. Therefore, the past groups have relied on fast reactors, long irradiation procedures, and large solid samples. In order to maximize our activity while minimizing the thermal activations of our sample, the Cd liner in the 3L canister was used.

The predominant calcium isotope in naturally occurring calcium is the desired  $^{40}\text{Ca}$ , so the additional expense of an enriched sample was unnecessary. The natural abundance of calcium isotopes is shown in Table 4.2.

Table 4.2. The percent abundance of calcium isotopes in naturally occurring Ca.

Ca isotope	Percent Abundance
$^{40}\text{Ca}$	96.941%
$^{42}\text{Ca}$	0.647%
$^{43}\text{Ca}$	0.135%
$^{44}\text{Ca}$	2.086%
$^{46}\text{Ca}$	0.004%
$^{48}\text{Ca}$	0.187%

The decision of which calcium-containing compound to use was based on ease of gas separation, minimizing the waste streams, and ability to withstand the heat generated during the irradiation within in Cd-lined facility. The major compounds considered were calcium oxide ( $\text{CaO}$ ), the metallic form, and calcium oxalate ( $\text{CaC}_2\text{O}_4$ ) shown in Table 4.3. Calcium oxalate allows for the easiest extraction of  $^{37}\text{Ar}$  requiring only a liquid nitrogen-cooled charcoal trap and is relatively chemically inert. However, the compound breaks down to calcium oxide at temperatures of  $200^\circ\text{C}$ , which could be reached during the irradiation. The radioargon release was also poor, even when heated. Metallic calcium has a high density of calcium and a high melting point. However, the separation of gas from the sample will be extremely difficult and require multiple steps. Therefore,

CaO was chosen for this experiment. CaO is chemically stable at high temperatures and has a high density of Ca. Also, the possibility of removing the produced argon gas is not as involved as the metallic Ca.

Table. 4.3. The advantages and disadvantages of using the different calcium-containing compounds.

	Advantages	Disadvantages
CaO	High calcium density High melting point	Argon release requires dissolving compound in nitric acid (liquid waste stream)
Metallic	High calcium density High melting point	Extremely difficult to separate radioargon
CaC <sub>2</sub> O <sub>4</sub>	Easy to extract argon (liquid nitrogen-cooled charcoal trap)	Decomposition temperature could be reached in cadmium-lined 3L

This method is preferred by scientists with access to a fast reactor system. In order to minimize the thermal activation of the system, the Cd-liner was used in the 3L canister instead of the lead-lined canister used for the other experiments. The modified flux profile allowed for a longer irradiation without compromising the activity of <sup>37</sup>Ar produced. With the thermal activations minimized, the <sup>37</sup>Ar capture reactions—(n,α), (n,p), and (n,γ)—were minimized, which allowed for a larger final induced activity of <sup>37</sup>Ar.

Using the flux profile generated by the MCNPX reactor model and the CINDER90 cross-section library, collapsed cross-sections were generated for the reactions of interest. The activities of the isotopes of interest were calculated at various

time steps in order to optimize the irradiation time, shown in Figure 4.10.  $^{41}\text{Ar}$  was also expected, but CINDER90 did not have an available cross-section for the  $^{44}\text{Ca}(n,\alpha)$  interaction. The ENDF VII.0 cross-section reaction cross-section libraries were used for  $^{42}\text{Ca}(n,p)^{42}\text{K}$  and  $^{44}\text{Ca}(n,\alpha)^{41}\text{Ar}$  (Chadwick, *et al.* 2006).

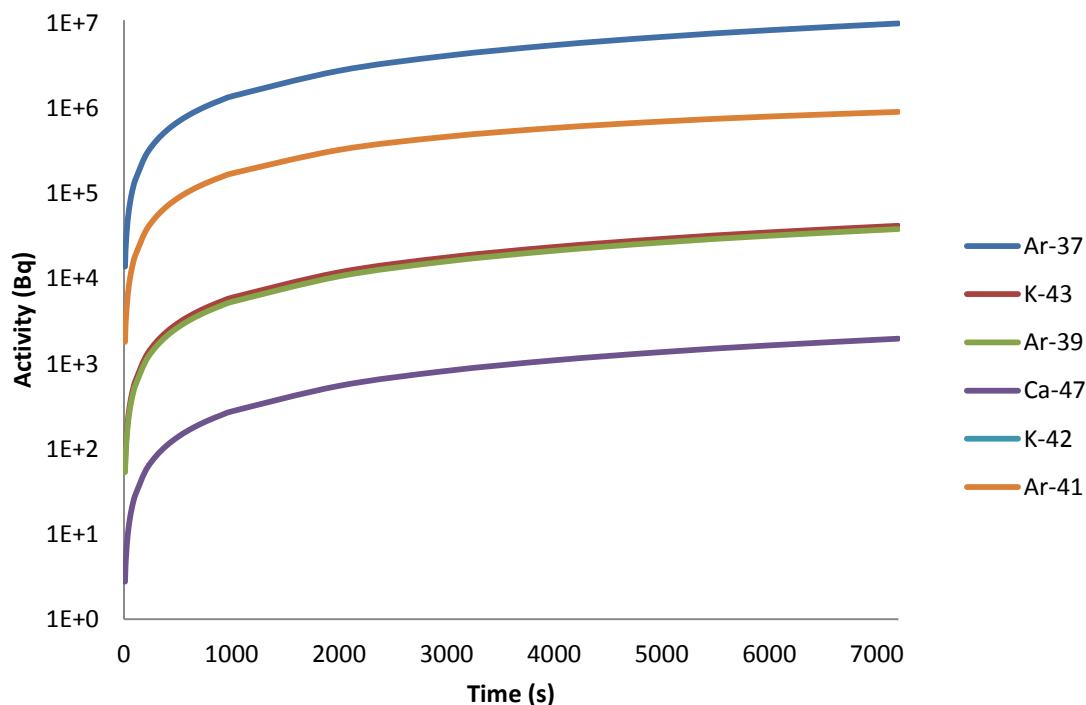


Figure 4.10. The activity induced of isotopes of interest at different time steps assuming a position in the Cd-lined 3L facility at 500 kW.

#### 4.2.1 EXPERIMENTAL SET-UP

A 2.0 g sample of CaO (Puratronic®, 99.998%--metals basis, excluding other alkaline earth and alkali metals 130ppm max) was enclosed in a double-walled quartz ampule. The sample was pumped down in order to minimize gaseous contaminants in the sample tube. A Co-Al neutron flux density wire (NIST SRM 953) was taped to the tube in the center of the sample in order to calculate a neutron fluence during the irradiation

and is shown in Figure 4.11. The sample was wrapped in aluminum foil with a loop at the end to allow the reactor operator to easily remove the sample for the Cd-lined 3L facility, shown in Figure 4.12.

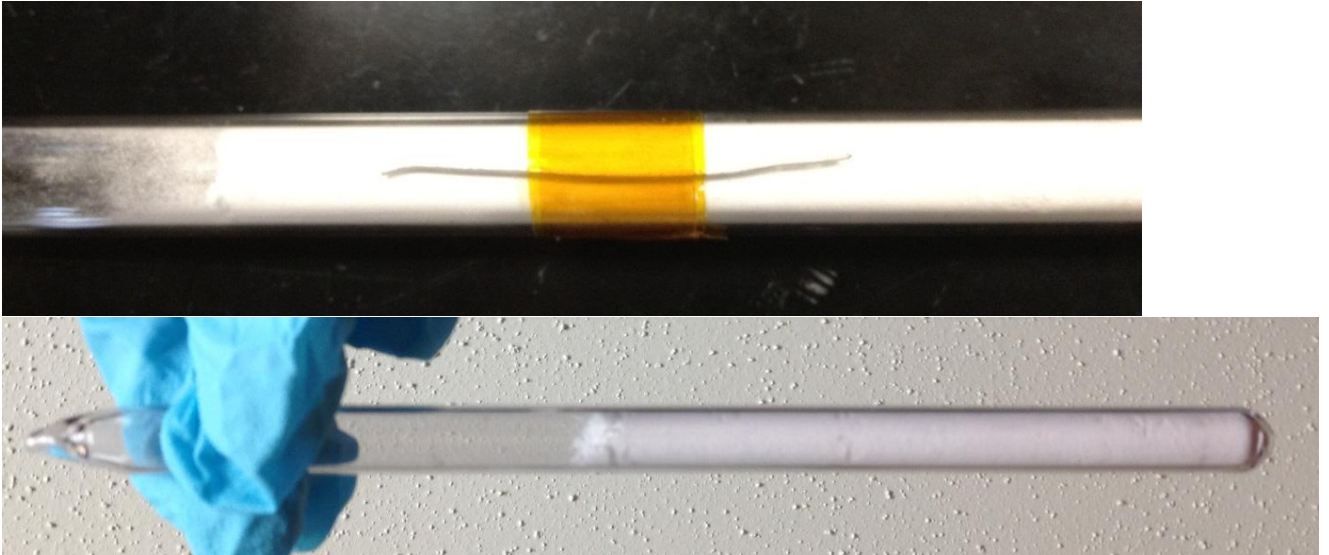


Figure 4.11. The quartz ampoule filled with 2.0 g CaO is shown in the bottom picture. The ampoule and the placement of the neutron density flux monitoring wire is shown in the top picture.



Figure 4.12. The aluminum foil wrapped around the sample to ease the removal of the sample from the narrow 3L aluminum canister.

#### **4.2.2 METHOD**

The sample was irradiated for 2 hours in the Cd-lined facility at 500 kW in the morning. The sample was removed after the reactor was shut down for the day. The quartz ampule was placed on a single HPGe detector, shown in Figure 4.13, about 12 hours after the end of the irradiation. The sample was counted in position D (7 cm) for all of the counts.

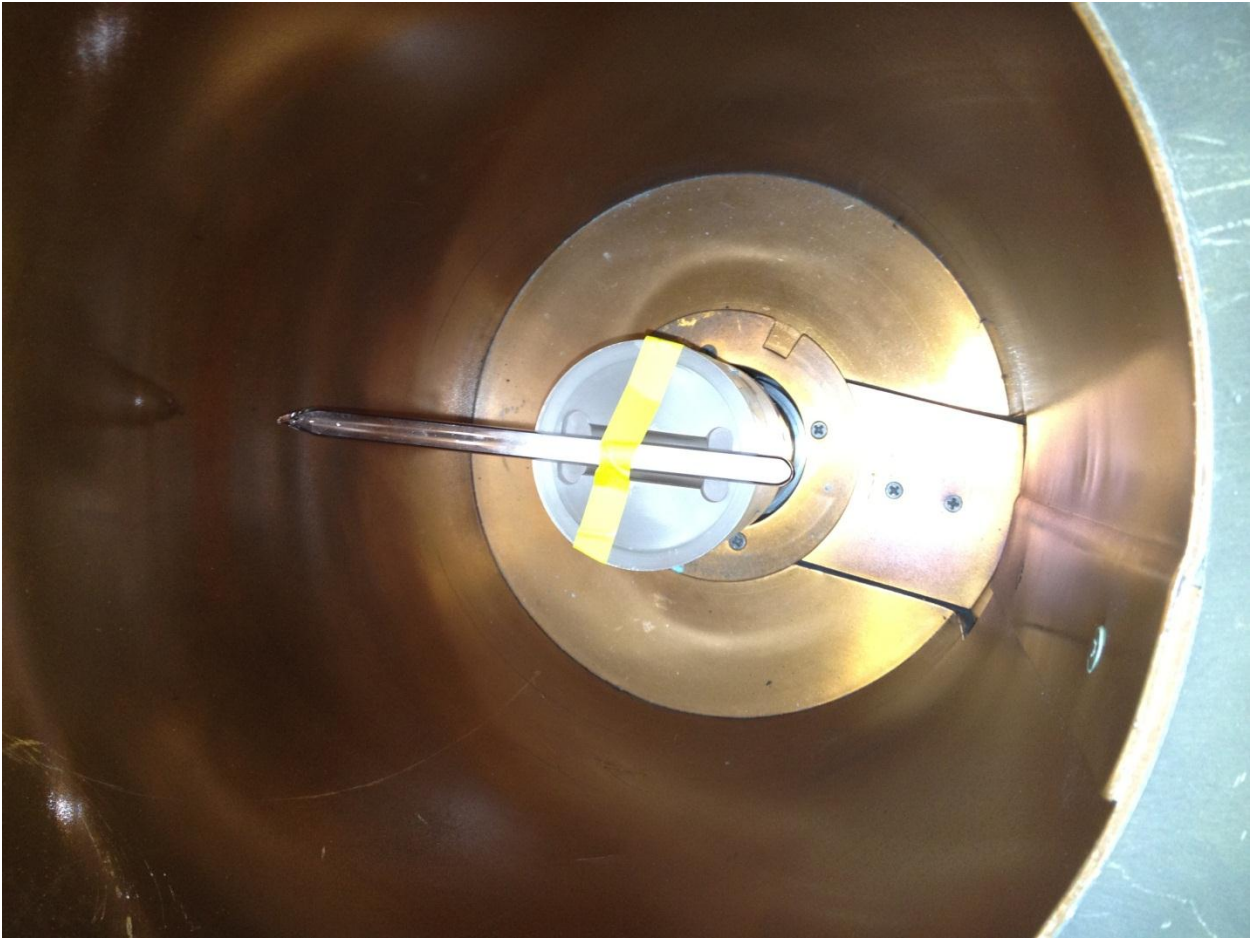


Figure 4.13. The positioning of the quartz ampoule after irradiation. The neutron density flux monitoring wire has been removed.

#### **4.2.3 PROCEDURE**

1. Seal the 2.0 g of CaO in a double-wall quartz ampoule with a vacuum. Keep the CaO away from moisture because it is highly reactive.
2. Store the ampoule in an upright position to allow the CaO powder to fall to the bottom of the ampoule.

3. Weigh a piece of SRM 953 and attach it to the center of the powder on the ampoule. Affix the wire with the tape approved for irradiation experiments, as shown in Figure 4.11.
4. Wrap the quartz ampoule in aluminum foil with a loop at the top as shown in Figure 4.12.
5. Keep the sample upright to keep the CaO settled in the bottom of the ampoule.
6. Irradiate the sample in cadmium-lined 3L facility at 500 kW for 2 hours in the morning.
7. Due to the activation of the silicon in the surrounding material, the sample should be left in the reactor until the end of the day.
8. Count the sample with a HPGe detector for 2 hours in the D position.
9. Continue to periodically count the sample with the sample HPGe detector for increasing time intervals.
10. The entire sealed ampoule will be placed in long-term storage when the sample is no longer needed.

#### **4.2.4 PRODUCTION**

There were numerous counting intervals as the sample decayed—length, start date, and live time are shown in Table 4.4. The beginning counting intervals were shorter, which would allow the short-lived isotopes show through even with an extremely active sample.

Table 4.4. CaO counting time.

Count Number	Date	Start Time	Real Time (s)
1	5/31/2012	10:45 PM	504
2	5/31/2012	10:56 PM	7200
3	6/1/2012	9:48 PM	7200
4	6/1/2012	1:20 PM	7200
5	6/1/2012	5:21 PM	43200
6	6/2/2012	10:09 AM	43200
7	6/3/2012	12:52 PM	80000

The first two counting periods showed the appearance of  $^{41}\text{Ar}$ , which was produced via the  $^{44}\text{Ca}(n,\alpha)$  pathway. Counting period two is shown in Figure 4.14 with the  $^{41}\text{Ar}$  and  $^{47}\text{Ca}$  peaks in the 1,290 keV region in an enlarged picture. In the subsequent counts, the count time was longer and did not show the presence of any other radioargon isotopes. The sample was counted periodically over the next week to find the signatures of other radioactive products. The 1,524.70 keV peak of  $^{42}\text{K}$  was present in the first seven spectrum and was produced through the  $^{42}\text{Ca}(n,p)$  pathway. The peaks of  $^{43}\text{K}$  at 220.631 keV, 372.760 keV, 396.861 keV, 593.390 keV, and 617.490 keV were also present in the majority of the spectra. The only radiative capture product of calcium was  $^{47}\text{Ca}$  with a 4.536 day half-life. The 1,297.09 keV peak was present in the spectra. The larger peaks from the  $^{42}\text{K}$ ,  $^{43}\text{K}$ , and  $^{47}\text{Ca}$  are shown in Figure 4.15.

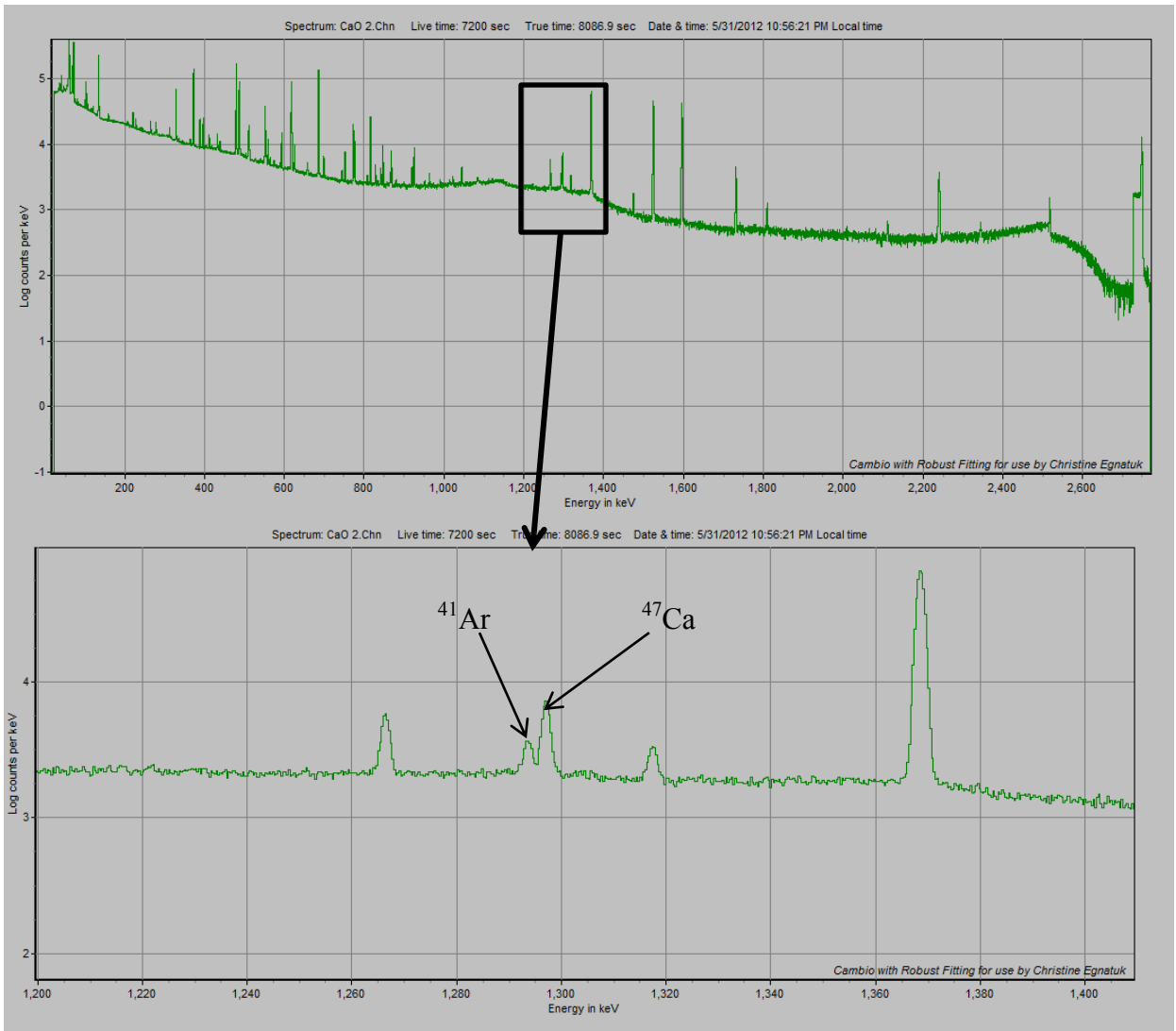


Figure 4.14. CaO spectra.

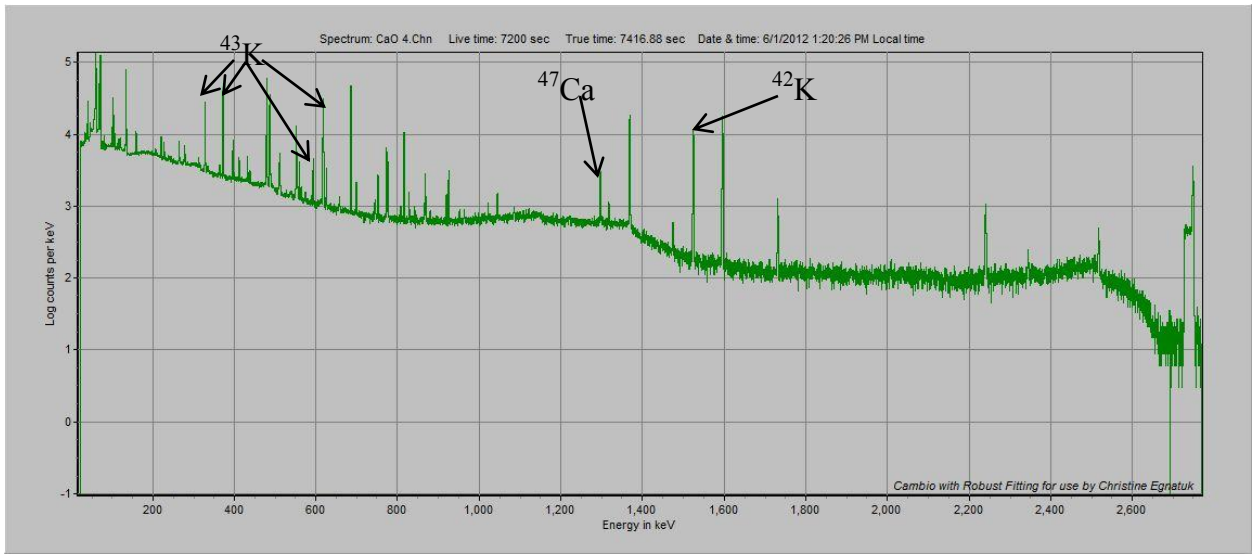


Figure 4.15. A longer count of the CaO sample after a longer decay period.

This experiment was a successful in producing a radioargon sample that is predominantly  $^{37}\text{Ar}$  with a TRIGA reactor via the  $^{40}\text{Ca}(n,\alpha)$  pathway. With the proper detector set-up the production ratios of radioargon isotopes could be determined. This method would provide radioargon production ratios that are much closer to the underground nuclear event signature. Since there were no experiments which required  $^{37}\text{Ar}$  at production time, the entire sample remains in the sealed quartz ampule. The separation procedure requires nitric acid and would produce a radioactive liquid waste stream, which would be costly to dispose of and problematic to store at the NETL facility. The sealed sample will be placed in RAM storage for the foreseeable future.

#### 4.2.5 RESULTS

The induced activities of  $^{37}\text{Ar}$  and  $^{39}\text{Ar}$  were estimated by calculating a detectable radionuclide activity at the end of irradiation. Then the activity of the radioargon isotope of interest was estimated by using a production ratio based on the cross-sections. The

cross-sections used were the collapsed cross-sections based on the CINDER90 libraries for  $^{43}\text{K}$  and  $^{47}\text{Ca}$ . Due to the lack of  $^{44}\text{Ca}(n,\alpha)^{41}\text{Ar}$  and  $^{42}\text{Ca}(n,p)^{42}\text{K}$ , reaction cross-section libraries in CINDER90, the reaction cross-sections from ENDF VII.0 (Chadwick, *et al.* 2006) were used. The energy-dependent flux weighted reaction cross-sections used in the calculations are shown in Table 4.5. For the upper energy dominated reactions like (n, $\alpha$ ), the fission spectrum average cross-section is larger than the collapsed cross-section. However, when the reaction is dominated by thermal neutrons like a radiative capture reaction, the fission spectrum averaged cross-section is much lower than the collapsed cross-section.

Table 4.5. Calcium cross-sections used to estimate the  $^{39}\text{Ar}$  and  $^{37}\text{Ar}$  production activities.

Reaction	Collapsed cross-section	Fission Spectrum Averaged Cross-section
$^{40}\text{Ca}(n,\alpha)^{37}\text{Ar}$	21.2 mb	49.77 mb
$^{42}\text{Ca}(n,\alpha)^{39}\text{Ar}$	0.594 mb	2.675 mb
$^{44}\text{Ca}(n,\alpha)^{41}\text{Ar}$	81.2 $\mu\text{b}$	212.1 $\mu\text{b}$
$^{42}\text{Ca}(n,p)^{42}\text{K}$	2.42 mb	9.139 mb
$^{43}\text{Ca}(n,p)^{43}\text{K}$	1.74 mb	26.73 mb
$^{46}\text{Ca}(n,\gamma)^{47}\text{Ca}$	13.2 mb	172.2 $\mu\text{b}$

The production activities were estimated using the following equation

$$A_{Ar-37}(t_d = 0) = A_{Ar-41} \frac{N_{Ca-40} \sigma_{\alpha}^{Ca-40} (1 - e^{-\lambda_{37} t_i})}{N_{Ca-44} \sigma_{\alpha}^{Ca-44} (1 - e^{-\lambda_{41} t_i})} \quad (4.4)$$

The estimated activities and the values from the MCNPX model are shown in Table 4.6. The error represented in the table is only a function of the counting and efficiency. This is a gross underestimation. The largest source of error will be the cross-section libraries, but there was not a straight forward way to calculate this error.

Table 4.6. The estimated activities and the modeled activities in Bq.

Based on	Estimated Activities		MCNPX model	
	<sup>37</sup> Ar	<sup>39</sup> Ar	<sup>37</sup> Ar	<sup>39</sup> Ar
<sup>41</sup> Ar	6.51E5±2.75E4	4.35E-2±3.52E-3	1.15E6	7.68E-2
<sup>42</sup> K	1.28E6±5.47E3	8.51E-2±7.00E-4		
<sup>43</sup> K	1.30E6±8.47E3	8.66E-2±5.66E-4		
<sup>47</sup> Ca	4.08E6±1.01E05	2.72E-1±3.52E-3		

## CHAPTER 5: LARGE VOLUME IRRADIATION PROCEDURE

In order to understand the signature of a nuclear event or activity via radioargon activities, the ratio of radioargon isotopic activities is necessary. Therefore, another radioargon isotope will need to help decipher the meaning of the  $^{37}\text{Ar}$  activity detected.  $^{41}\text{Ar}$  is relatively easy to detect due to a 99% intensity of a high energy gamma-ray (1,293.587 keV) during its decay to  $^{41}\text{K}$ . Unfortunately, the half-life of  $^{41}\text{Ar}$  (109.34 min) is too short to allow it much use during event analysis. However,  $^{41}\text{Ar}$  is regularly used throughout these experiments as a benchmark for the other radioargon production activities.

In order to fill the void,  $^{42}\text{Ar}$  was proposed as a secondary radioargon isotope. In order to produce a measureable amount of  $^{42}\text{Ar}$ , a large amount of  $^{40}\text{Ar}$  needed to be irradiated. The production of  $^{42}\text{Ar}$  requires longer irradiation periods because of the double capture production pathway. In an event setting,  $^{42}\text{Ar}$  can be produced through the double capture of  $^{40}\text{Ar}$  naturally occurring in the air or the (n, $\alpha$ ) reaction with  $^{45}\text{Ca}$  in the soil.

The TRIGA reactor at The University of Texas has been used in the production of gaseous radioisotopes through the irradiation of stable noble gases (Haas *et al.*, 2009 and Ward *et al.*, 2009). The methods have included irradiation within (Ward *et al.*, 2009) and outside of the reactor at a beam line (Haas *et al.*, 2009; Ward *et al.*, 2009). The gas irradiation procedures previously in place at The University of Texas at Austin have relied on the irradiation of a relatively small volume of gas (0.5-1.75cm<sup>3</sup>). The in-core irradiation procedure was similar to the  $^{37}\text{Ar}$  production experiments using the Teflon

Swagelok valve. In order to avoid pressuring the gas, a technique was developed which would allow a significantly larger (1.4 L) gas sample to be irradiated.

The irradiation canister already in place for in-core irradiations in the 3L position was used as the basis for the development of the technique. Some of the constraints on the methodology included the reactor operating schedule and the short half-life of  $^{41}\text{Ar}$ . In order to accommodate the reactor operator schedule, the irradiation was broken up into 3 twelve hour irradiations separated by a 12 hour cooling period while the reactor was not operating. Due to the short half-life of  $^{41}\text{Ar}$ , a significant portion of the  $^{41}\text{Ar}$  produced in the previous day would have decayed by the time the reactor was started up the next day. Therefore, the broken irradiation procedure required extra time to allow for the build-up of  $^{41}\text{Ar}$ .

## 5.1 Experimental Set-up

$^{40}\text{Ar}$  is a naturally occurring, stable argon isotope that makes up 99.6003% of natural argon gas. Due to the high percentage of  $^{40}\text{Ar}$  in natural argon, there was no need to use an enriched gas. The first step in the production mechanism of  $^{42}\text{Ar}$  requires the radiative capture of a neutron, which produces  $^{41}\text{Ar}$ .  $^{41}\text{Ar}$  has a 109.34 minute half-life and must capture another neutron in order to produce  $^{42}\text{Ar}$ .

Approximately 1.4 L of natural argon gas at STP was irradiated for a total of 36 hours. The three 12-hour irradiation periods were broken up by cooling periods of 12-hours with a final cooling period of 84 hours before the gas was transferred to a double-ended gas cylinder for storage and shipment. The cooling time between irradiation

periods was required to fit into the reactor operating schedule, but it lengthened the irradiation time to produce the required activity of  $^{42}\text{Ar}$ . The long decay period at the end of the experiment was to minimize the exposure risk due to the induced activities of the impurities within the 6061 Al irradiation canister. This decay period allowed for nearly all of the  $^{41}\text{Ar}$  to decay to a point where activity levels were below our HPGe detector system detection limits. Therefore, the other radioargon isotope activities could not be extrapolated through production ratios as in other natural argon gas irradiations. The activity of the individual radioargon isotopes were solely calculated through the activation equations and the flux profile generated by MCNPX with normalization to the flux monitor.

The system was designed to maximize the amount of natural argon in the reactor while minimizing safety concerns. Therefore, the irradiation canister was filled to approximately the ambient pressure of natural argon gas. There were also venting mechanisms within the system to avoid any explosions if there was an overflow or extreme temperature change. The storage container was also chosen at a larger volume than the irradiation canister, so the irradiated gas in the container would be at a lower pressure than the surrounding environment and much lower than the pressure ratings of the cylinder. The larger storage container also improved the transfer efficiency of the system.

The gas transfer system, shown in Figure 5.1 was built around a 4-stage KNF diaphragm vacuum pump and compressor. The KNF pump was used to transfer the irradiated argon gas from the 3L to the transport container and is referred to as the

transfer pump in Figure 5.1. A separate vacuum was used to purge the system after excess natural argon gas filled the system.

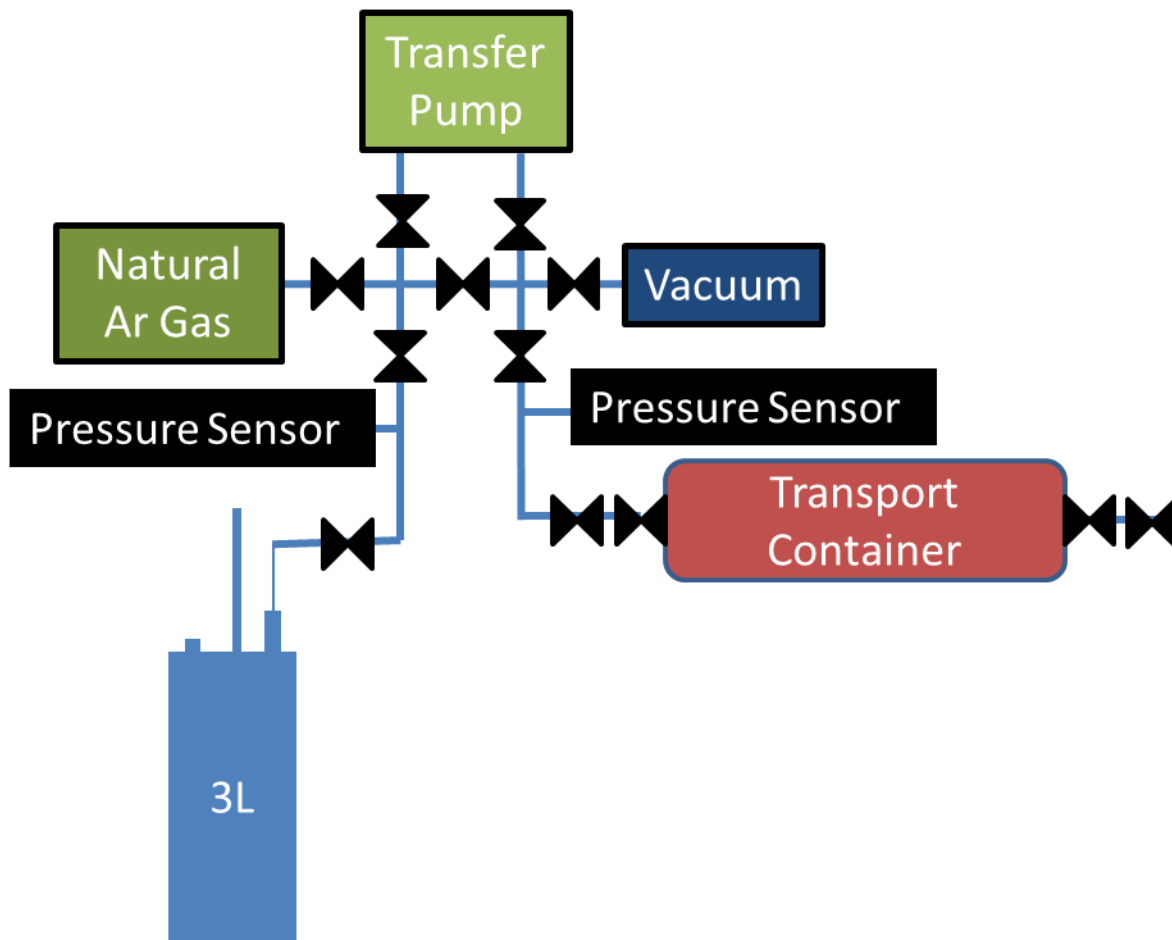


Figure 5.1. Gas Transfer System.

The valves indicated by the double-triangles in Figure 5.1, are Swagelok diaphragm valves, in Figure 5.2, with double female VCR fittings. The diaphragm valves were used whenever possible because the user can easily tell when the valve is open or closed. This valve also prevents the user from over-turning the valve and possibly breaking it.

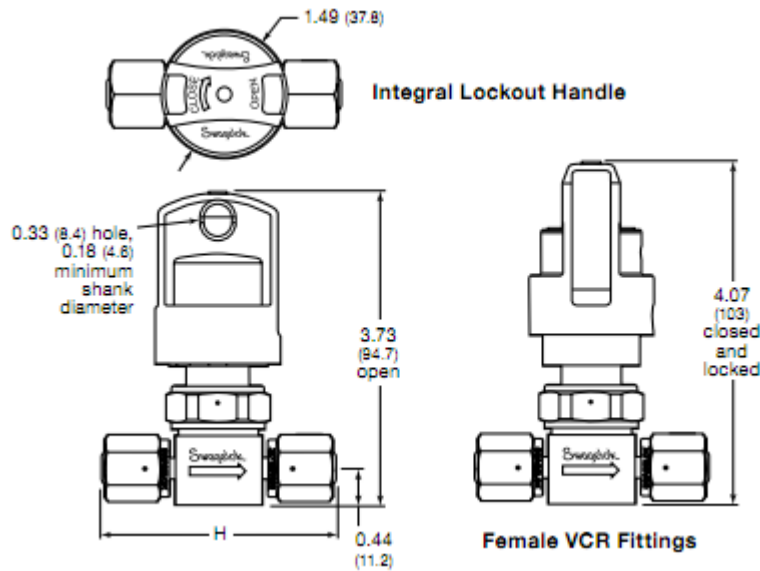


Figure 5.2. Swagelok diaphragm valves with double-sided female VCR fittings.

The irradiation canister, referred to as the 3L in Figure 5.1, is a 6061 aluminum canister specifically designed for in-core irradiations in the 3L position of The University of Texas reactor facility. Instead of placing a small vial in the core, as in the  $^{37}\text{Ar}$  production methods, the entire canister was filled with natural argon gas. The volume of the canister with the necessary lead weight, to prevent the canister from floating, is around 1.4 L. The volume of argon gas that is within the fuel length is 0.6 L. A schematic of the 3L canister is shown in Figure 5.3. The irradiation canister has one stainless steel bellows valve placed on the top to allow for easy attachment to the transfer system and a pressure relief valve, shown in Figure 5.4. The Swagelok stainless steel check valve is spring-loaded and will pop when the pressure exceeds 25 psig. The spring-loaded feature allows for the venting of a small amount of gas if the pressure of the cylinder exceeds 25 psig without completely emptying the container contents upon overpressure. The expansion of the gas in the canister during irradiation was considered

and no temperature possibly reached within the reactor core would cause the gas to reach a burst pressure. However, the safety mechanism was in place to avoid any possibility of a container burst. The valve was also a safety check for the filling of the canister during the flush and purge steps, as well as the gas placed into the canister for irradiation.

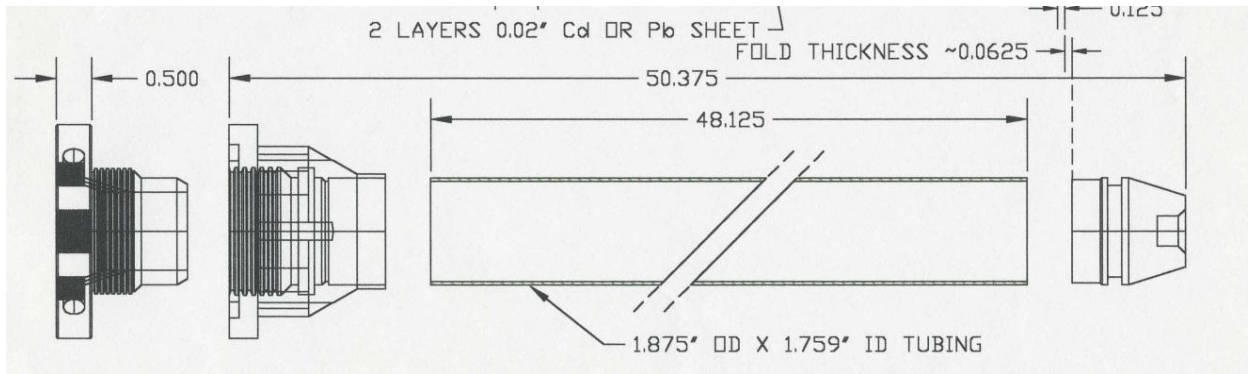


Figure 5.3. 3L irradiation canister made of 6061 aluminium with a lead liner for additional weight.

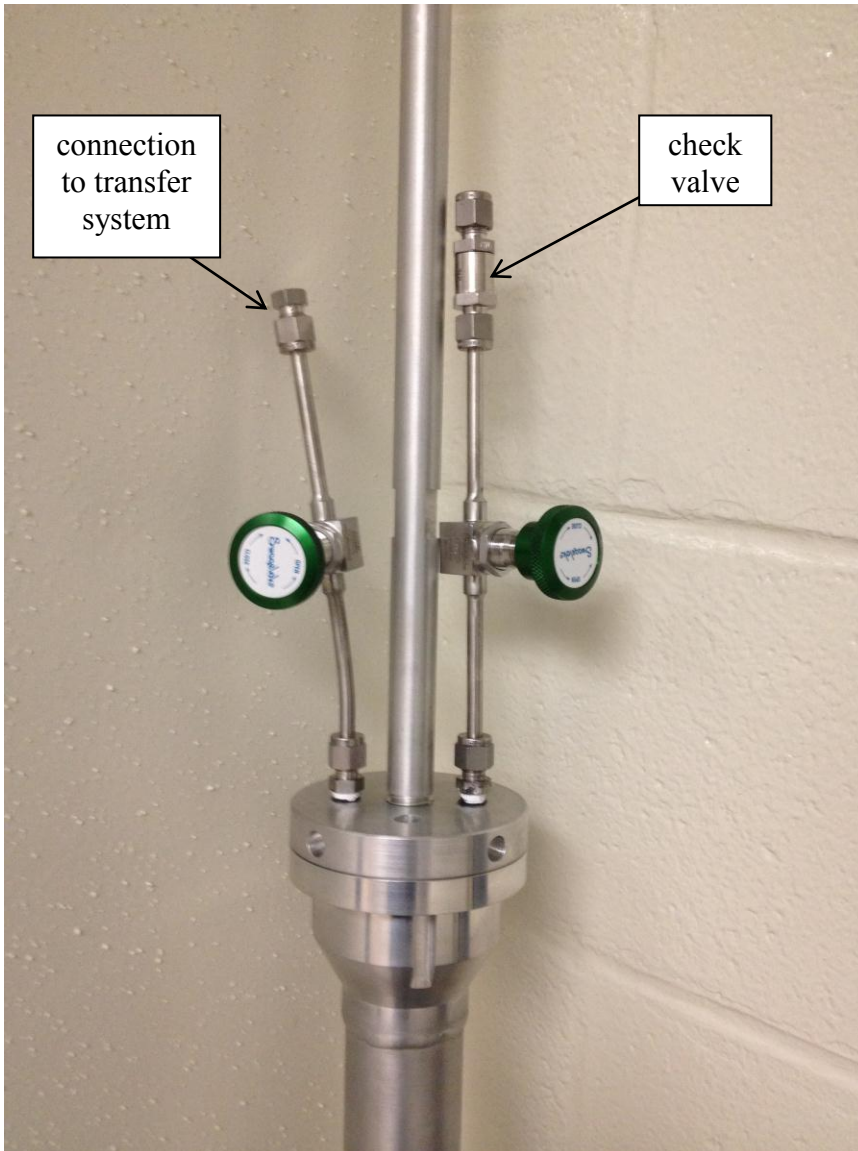


Figure 5.4. The top of the 3L irradiation canister. The two green Swagelok bellows valves are shown. The connection to the check valve is open during irradiation and filling, but closed while the vacuum or the transfer pump is on. The valve that connects to the transfer system is closed during irradiation and sealed with a small metal piece.

There was also concern of the exposure rate due to the impurities in the 6061 aluminum canister.  $^{28}\text{Al}$  has a 2.414 min half-life and is not an exposure concern. However, the impurities in the aluminum—silicon, iron, copper, manganese, magnesium,

chromium, zinc, and titanium—posed a possible exposure concern with the lengthened irradiation protocol. The activation of the aluminum and its impurities was done using ORIGEN-ARP in the SCALE 6.0 package in activation mode. The activities of the resulting radionuclides and used for the start of the exposure calculation. The exposure rate calculation was broken into two parts. The canister included shielding from the water; the lid included no shielding. Since the user would be touching the canister at the time of removal from the core, the exposure rate was calculated at the surface of the water. The exposure rate from each gamma-rays released during the decay of each radionuclide were corrected for attenuation and summed. The resulting exposure rate is shown in Figure 5.5. Due to a last minute change of plans, an older, previously irradiated canister was used for the experiment. Therefore, the exposure rate due to the 6061 aluminum canister was higher than anticipated, but presented no threat to the researcher during the gas transfer.

### Exposure rate at the surface of the water due to 3L 6061Al Canister

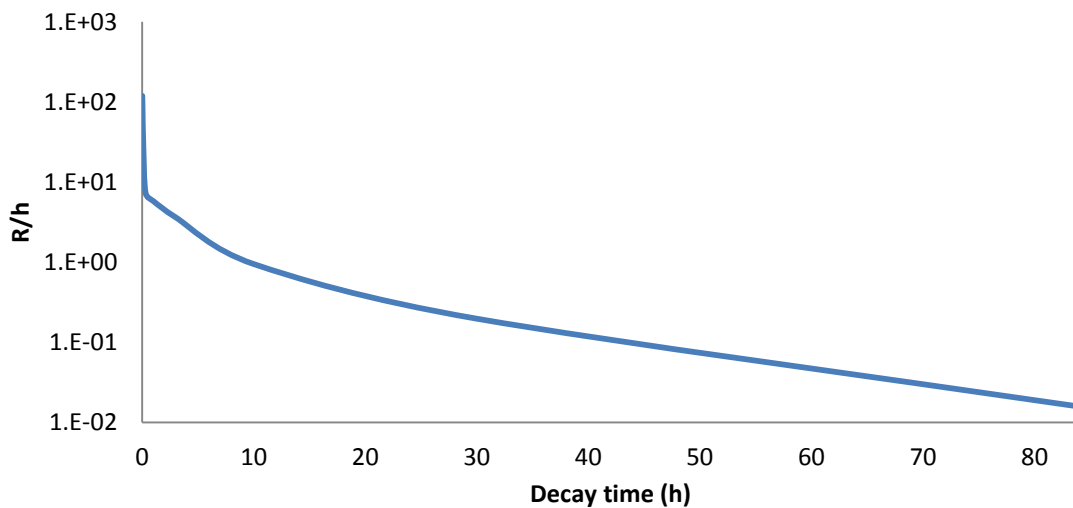


Figure 5.5. The exposure rate of the 6061 aluminum canister after three 12 hour irradiation periods separated by a 12 hour cooling period and an 84 hour decay period after the final irradiation.

In order to have the aluminum canister stay in place in the 3L position, a lead weight is necessary. The mass of the water displaced by the argon gas was calculated. An additional two pounds of negative weight, below buoyancy was added. Therefore, 5.606 pounds of lead was placed in the 3L canister. The same ORIGEN-ARP set-up was run with natural lead to calculate the activities at the end of the irradiation. The decay was used to calculate the exposure rate, shown in Figure 5.6. For this calculation, the attenuation of the air is only considered. The attenuation of the aluminum cap, although substantial, was not considered. The exposure due to the lead weight (ignoring the aluminum attention) will be  $2.24 \times 10^{-4}$  mR/h at 1 foot.

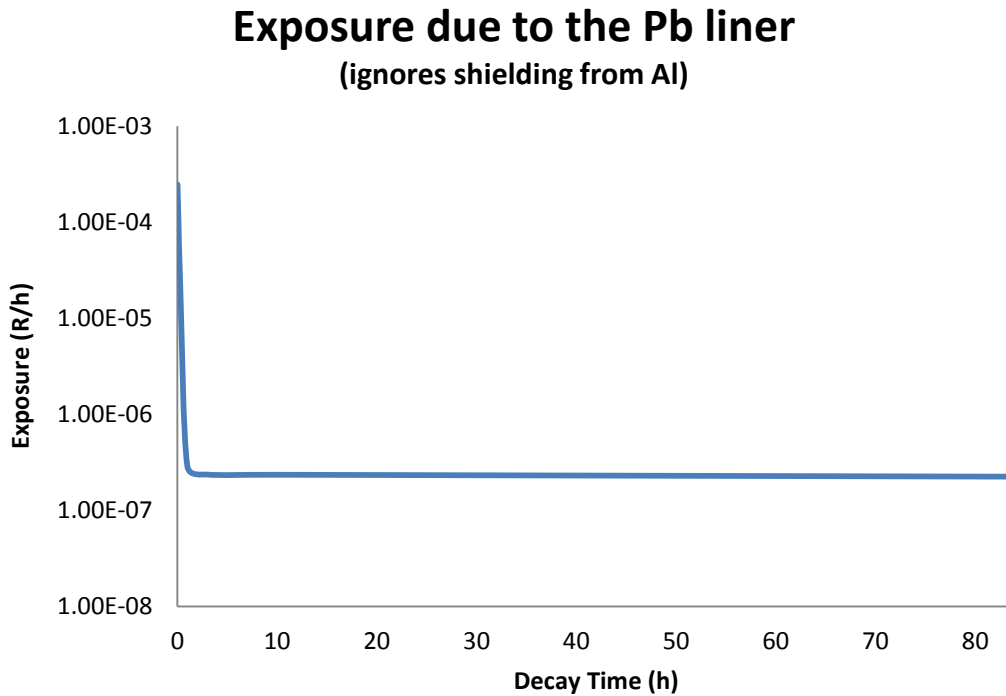


Figure 5.6. The exposure rate from the lead liner post-irradiation.

After the irradiation, the irradiated gas is transferred to a double-ended Swagelok gas cylinder, shown in Figure 5.7. The cylinder has two diaphragm valves, shown in Figure 5.8, on each side with a vacuum between them in order to ensure the gas sample quality. Epoxy was used on NPT connection between the cylinder and the connection piece, which then is attached to the first diaphragm valve. The second diaphragm valve is used for a back-up, as well as a double check. The volume between the two diaphragm valves on each side of the cylinder was pumped down to 0.3 psia. If the seal needs to be checked, the cylinder can be attached to the transfer system and the first diaphragm valve can be opened for the pressure to be checked.

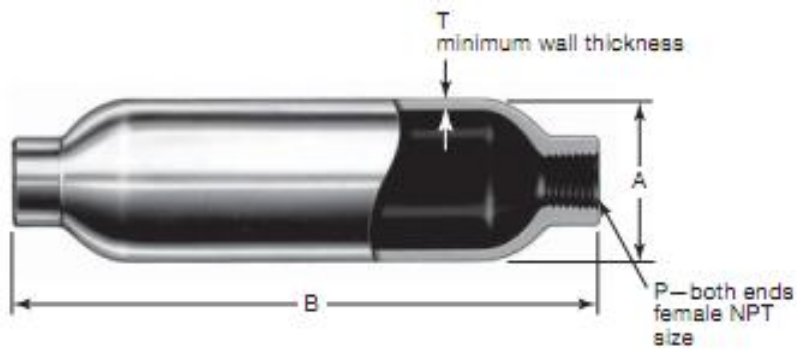


Figure 5.7. Swagelok double-ended cylinder.

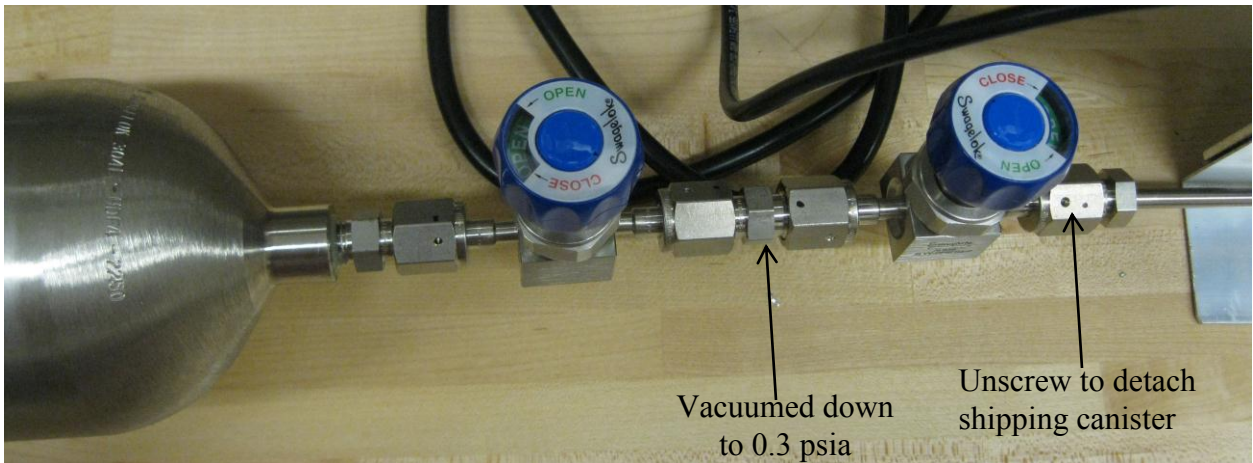


Figure 5.8. The connection from the Swagelok shipping cylinder to the transfer system.

There were three trial runs with this system before the actual 36 hour irradiation. This allowed for the ironing out of kinks and system checks including the vacuum seal and valve function. The trial runs included a shorter irradiation period, 15 to 45 minutes, and a shorter cooling period. The shorter cooling period allowed for the detection of the irradiated gas through the decay of  $^{41}\text{Ar}$ . The short-lived isotope is the major product of the irradiation and helped with the tracking of the irradiated gas through the transfer system.

The 3L canister was attached to the gas transfer system. The system will be pumped and flushed with argon gas. Then the 3L irradiation canister will be filled with argon gas through the opening of the diaphragm valves between the argon gas canister and the 3L irradiator. Assuming that the initial pressure in the canister is 14.696 psia when the canister is at room temperatures, an increase in temperature to 65 C will cause a resulting increase in pressure to 16.67 psia. Due to the 84 hour cooling time, the gas and canister will return to room temperature by the time of transfer.

After the irradiation and cooling period, the gas will be transferred from the 3L canister to a Swagelok double-ended cylinder. The system will be pumped and flushed with the natural argon gas in the same procedure as before the irradiation to remove impurities. The KNF UN813.4ANI transfer pump can be used to pump down a system to below 0.00725 Torr and will be used to transfer the gas from the 3L canister to the Swagelok double ended cylinder. The sealed pump will transfer the gas into a 2250 cm<sup>3</sup> Swagelok double-ended cylinder, which is pressure rated to 1800 psig.

## 5.2 Procedure

1. The system shown in Figure 5.9 should include the attachment of both the 3L canister and the gas cylinder.
2. In order to prepare the gas cylinder for irradiation. The system should be evacuated to less than 1 psia by setting the valve positions as indicated in Table 5.1 "Evacuate System" row and turning on the vacuum. This vacuum is only used to pump down the system, and it vents to the room. After the system is evacuated, the user should change the valve positions of the system to reflect Table 5.1 "Flush System" row. The regulator should be set to approximately 15 psi and the argon gas should be allowed to fill the system to approximately 14.7 psia.
3. Step 2 should be repeated 4 times.
4. The 3L canister should be pumped down to approximately 1 psia with the vacuum pump using valve positions in "Evacuate 3L" row of Table 5.1. The valve

- positions should be changed, as indicated in “Fill 3L with Ar” row of Table 5.1, and the system should be filled with natural argon to approximately 14.7 psia registering on P2.
5. After valve B1 is closed, the ¼” Swagelok nut above B1 is unscrewed. The 3L canister will be detached from the transfer system for irradiation. Valve B2 is opened, so the check valve (CV) will be able to allow venting if pressure above 25 psig is reached in the 3L canister.
  6. The 3L canister will be placed in the 3 element hole in the reactor.
  7. The irradiation will last 12 hours and be at 950 kW.
  8. After the irradiation is finished, the canister is left in the irradiation facility after the reactor is shut down for 12 hours.
  9. Steps 7 and 8 are repeated two more times (for a total of 3 irradiations). The final decay period is extended from 12 hours to 84 hours in order to allow the <sup>41</sup>Ar and activation products in the canister decay.
  10. The 3L canister is removed from the core position and placed in the dock at the top of the reactor pool. The dose rate at 30 cm from the 3L in the dock is measured. If the dose rate is significantly more than 25 mR/h, the HP or SRO has to evaluate the dose rate and give clearance before proceeding to the next step.
  11. The canister is connected to the transfer system by attaching the ¼” Swagelok nut connection, which stays connected to the transfer system, above valve B1 to the transfer system. Valve B1 is kept closed.

12. The valves of the system are set to the setting indicated by the “Evacuate System—prior to transfer” row in Table 5.1. The vacuum is turned on, and the double-ended gas cylinder (SC) evacuated to less than 1 psia, read through P1.
13. The valve positions are switched to the settings indicated by “Flush SC and system—prior to transfer” row. The regulator attached to the argon gas bottle is opened and set to approximately 15 psi. The system is filled to approximately 14.7 psia.
14. Steps 12 and 13 are repeated 3 more times. The double-ended gas cylinder will remain attached to the system throughout the entirety of the experiment in order to allow it to remain at a low pressure. The canister will be monitored throughout the experiment by making sure the pressure reading on P1 stays below 1 psia. If the system goes above 1 psia, check the connections. If no leaks are found, turn on the vacuum pump in the current valve positions.
15. After the valve positions are switched to the positions outlined the “Transfer Ar from 3L to SC” row, the radioargon is transferred from the 3L canister to the gas cylinder (SC) by turning on the transfer pump using the toggle switch on the backside of the pump.
16. After pressure gauge 2 (P2) indicates that the majority of the gas has been transferred to the other side of the system (pressure registering below 1 psia), the transfer pump will be turned off and the valve positions will be set-up according to the “Seal SC” row. The gas transfer can be double-checked by looking at P1.

- The pressure on pressure gauge 1 (P1) should be between 10 and 15 psia. The dose rate at 30 cm from the double-ended gas canister should be near background.
17. To prepare the gas cylinder for shipping, the vacuum will be turned on and the system will be pumped down using the valve positions specified in the “Seal SC” row. After the system reaches a pressure of approximately 1 psia, valve D9 will be closed. During this step, a small amount of radioargon will be vented into the room. Since the radioargon was allowed to decay for over 84 hours, the exposure rate will be negligible.
  18. The gas cylinder and attached valves (D9, D10, D11, and D12) will be detached from the system by unscrewing the Swagelok nut on the right side of D9, as shown in Figure 5.8. This set-up will be allowed to cool for an additional 3 days to allow  $^{41}\text{Ar}$  to decay away behind appropriate shielding as designated by HP or SRO.
  19. The Health Physicist will review the activities and dose rates and will address any special shipping requirements.

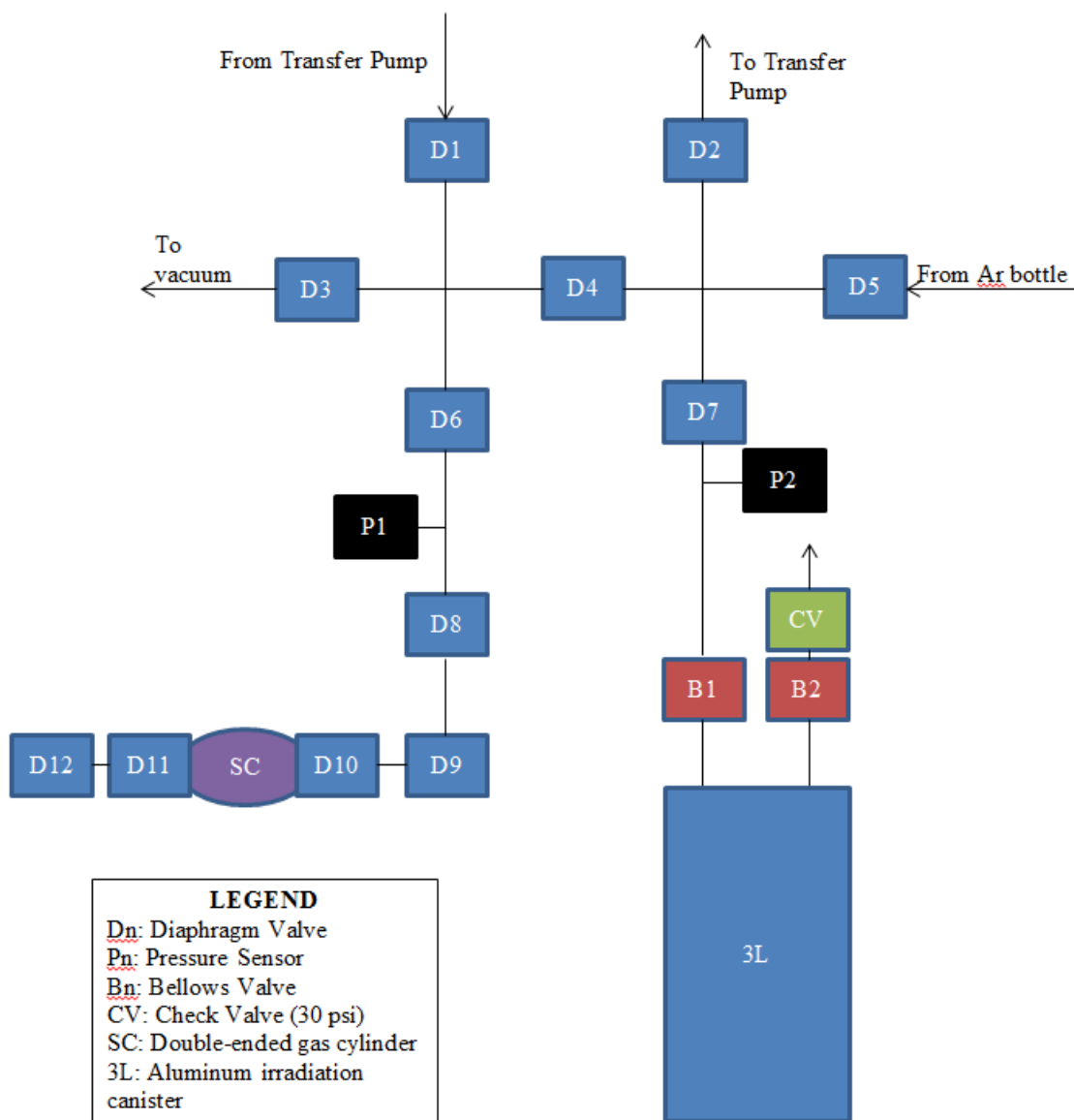


Figure 5.9. Large volume gas transfer system schematic with each valve labeled.

Table 5.1. The valve settings for each action with 0 indicating closed and 1 indicating open. For Ar (argon gas), TP (transfer pump) and V (vacuum), 0 means off and 1 means on.

	D1	D2	D3	D4	D5	D6	D7	D8	D9	D10	D11	D12	B1	B2	Ar	TP	V
Evacuate System	1	1	1	1	0	1	1	1	1	1	1	0	1	0	0	0	1
Flush System	1	1	0	1	1	1	1	1	1	1	1	0	1	1	1	0	0
Evacuate 3L	0	0	1	1	0	0	1	0	0	0	0	0	1	0	0	0	1
Fill 3L with Ar	0	0	0	0	1	0	1	0	0	0	0	0	1	1	1	0	0
Prepare SC for transfer	0	0	1	0	0	0	0	1	1	1	1	0	0	0	0	0	1
Transfer Ar from 3L to SC	1	1	0	0	0	1	1	1	1	1	1	0	1	0	0	1	0
Seal SC	0	0	1	0	0	1	0	1	1	0	0	0	0	0	0	0	1
Evacuate system—prior to transfer	1	1	1	0	0	1	1	1	1	1	1	0	0	0	0	0	1
Flush SC and system—prior to transfer	1	1	0	1	1	1	1	1	1	1	1	0	0	0	1	0	0

### 5.3 Model

The experiment was originally designed to produce a measurable amount of  $^{42}\text{Ar}$ . The requested amount was 1 mBq  $^{42}\text{Ar}$ . The initial calculations were conservative by considering a small volume and assuming a small flux. The production rate was calculated to be about seven times the requested activity, which would give a buffer on the experimental timeline or multiple experiments. The sample was eventually used for experiments requiring  $^{39}\text{Ar}$ . Therefore, the calculations include all of the radioargon activities induced during the irradiation. The sample was allowed to decay a few months before use to limit the amount of other radioargon isotopes present, specifically  $^{37}\text{Ar}$ .

A volume tally was used throughout the entire length of the 3L canister. The original estimation calculations only considered the 0.6L of gas along the length of the fuel. Considering the full volume of the 3L canister required an expansion of the UT TRIGA model and longer run times. The 63 group energy flux was used in conjunction with the energy-dependent CINDER90 cross-sections to create a collapsed cross-section. The values used in the production equations are shown in Table 5.2. The result also provided a much higher interaction rate with a volume increase of about 230%.

Table 5.2. The collapsed cross-section generated by the volume tally of the 1.4 L within the lead-lined 3L canister.

<b>Nuclide</b>	<b>Cross-section</b>	<b>Collapsed cross-section</b>
<sup>36</sup> Ar	$\sigma_c$	73.2 mb
<sup>37</sup> Ar	$\sigma_a$	52.7 b
<sup>38</sup> Ar	$\sigma_c$	0.326 b
<sup>39</sup> Ar	$\sigma_a$	241 b
<sup>40</sup> Ar	$\sigma_c$	0.258 b
<sup>41</sup> Ar	$\sigma_c$	0.236 b
<sup>42</sup> Ar	$\sigma_a$	58.7 mb

Due to the relatively small cross-sections of the stable argon isotopes, the number of atoms of <sup>36</sup>Ar, <sup>38</sup>Ar, and <sup>40</sup>Ar was assumed to be constant over the irradiation period. The activities of the four radioargon isotopes of interest were calculated, shown in Figure 5.10 and Table 5.3. The time axis in Figure 5.10 shows the continual time period of the experiment. The noticeable decreases in the <sup>41</sup>Ar activity are the periods when the reactor was off due to scheduling or the 84 hour decay period at the end of the experiment.

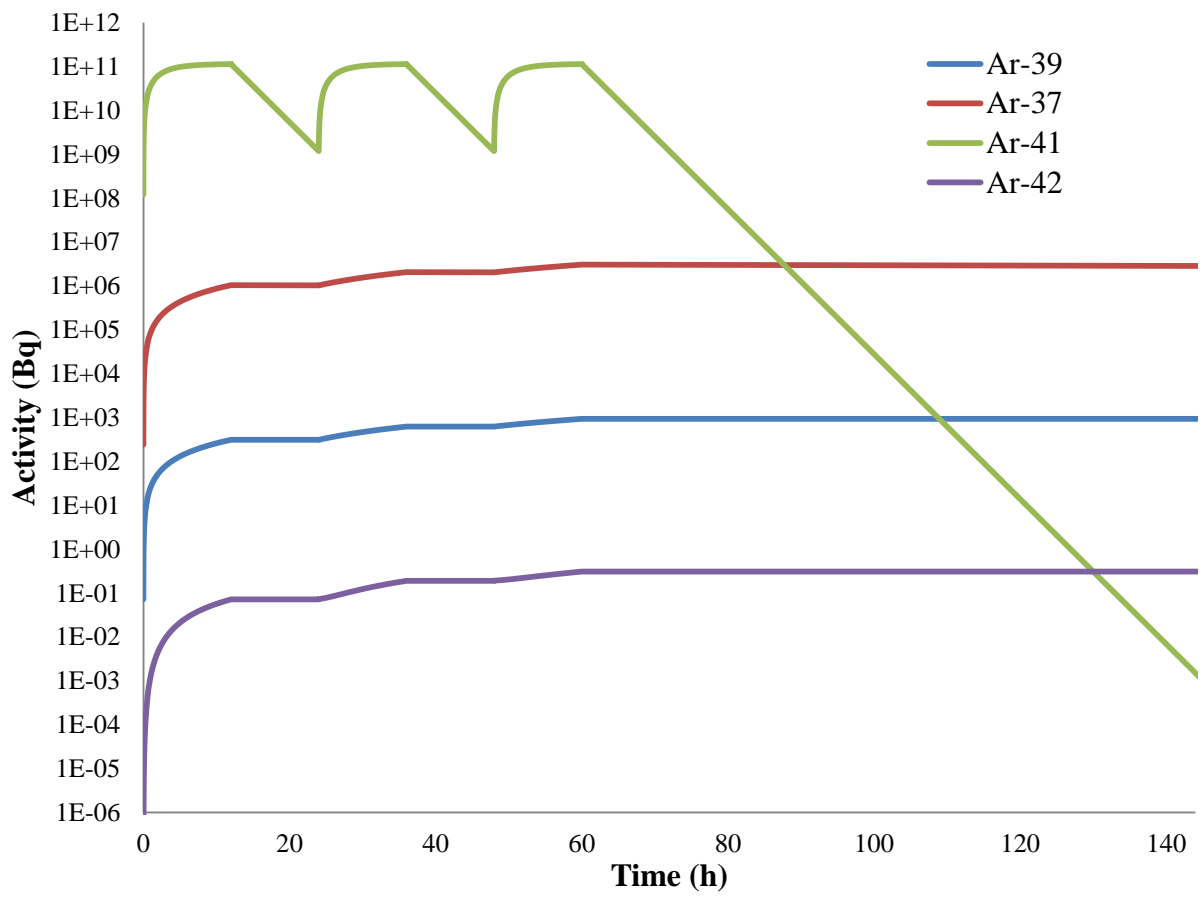


Figure 5.10. The activity of the radioargon isotopes through the irradiation and decay periods.

Table 5.3. Comparison of radioargon activities in Bq throughout the irradiation and decay process.

<b>Time (h)</b>	<b><sup>37</sup>Ar</b>	<b><sup>39</sup>Ar</b>	<b><sup>41</sup>Ar</b>	<b><sup>42</sup>Ar</b>
<b>12</b>	1.05E6	3.14E2	1.14E11	7.23E-2
<b>24</b>	1.04E6	3.14E2	1.19E9	7.23E-2
<b>36</b>	2.07E6	6.27E2	1.14E11	1.91E-1
<b>48</b>	2.05E6	6.27E2	1.19E9	1.91E-1
<b>60</b>	3.08E6	9.41E2	1.14E11	3.11E-1
<b>144</b>	2.87E6	9.41E2	1.25E-3	3.11E-1

### **5.4 Production Possibilities**

The large-volume gas irradiation procedure could also be used for additional radioisotope irradiations, specifically for noble gases. While there would be limitations due the lack of facilities to handle a sample with a high activity, this method could be safely used for the production of <sup>37</sup>Ar through the irradiation of enriched <sup>36</sup>Ar gas since <sup>37</sup>Ar decays via electron capture without the emission of a gamma ray. The exposure rate would be dependent on the purity of the gas used.

Assuming the full 1.4L volume was used and the irradiation was done at 950 kW with the lead-lined facility, a 12 hour irradiation would yield 3.7x10<sup>8</sup> Bq of <sup>37</sup>Ar. A shorter 2.5 hour irradiation would yield 7.83x10<sup>7</sup>Bq of <sup>37</sup>Ar. The induced <sup>37</sup>Ar activity is shown in Figure 5.11.

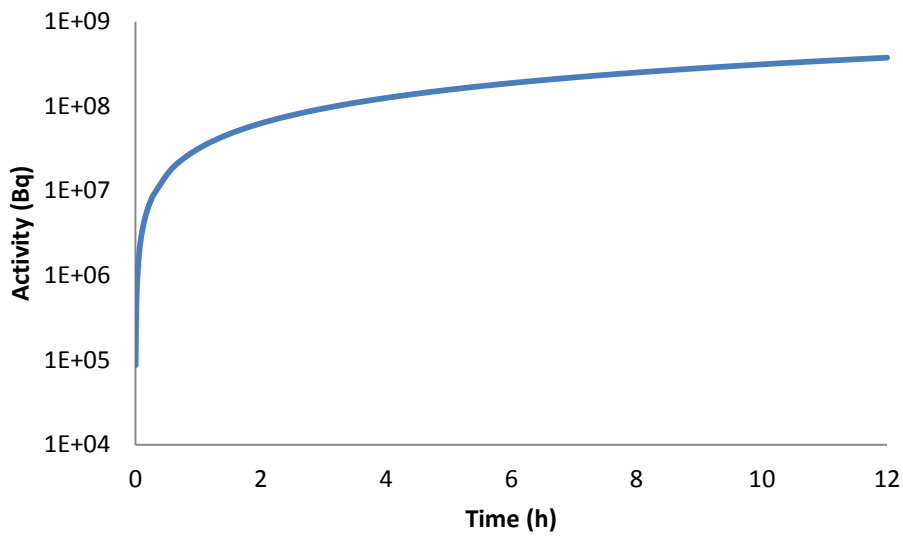


Figure 5.11.  $^{37}\text{Ar}$  activity with 1.4L of enriched  $^{36}\text{Ar}$  irradiated at 950 kW.

The production values of  $^{39}\text{Ar}$  using 1.4 L of enriched  $^{38}\text{Ar}$  gas would be  $1.15 \times 10^5$  Bq for a 2.5 h irradiation at 950 kW,  $3.68 \times 10^5$  Bq for an 8 h irradiation, and  $5.51 \times 10^5$  Bq for a 12 hour irradiation. The activation curve is shown in Figure 5.12.

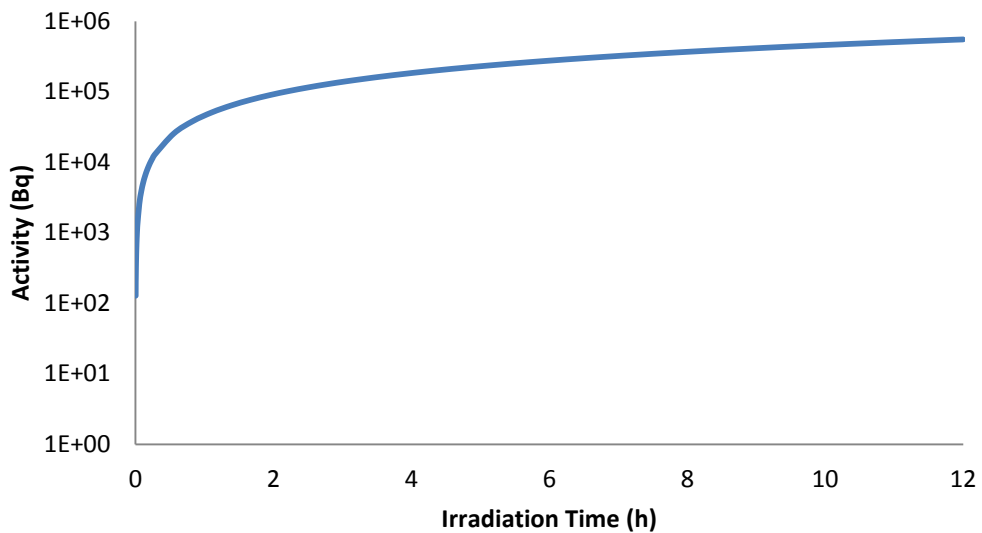


Figure 5.12. The activation curve of  $^{38}\text{Ar}(n,\gamma)^{39}\text{Ar}$ .

The production of  $^{127}\text{Xe}$  with the large volume gas irradiation procedure with enriched  $^{126}\text{Xe}$  gas was considered. This production also considered the  $^{127\text{m}}\text{Xe}$  component with a 69.2 s half-life, which decays to  $^{127}\text{Xe}$  with a 36.4 d half-life. The production model assumed an irradiation of 1.4L of enriched gas at 950 kW in the 3L facility. The induced activity of  $^{127}\text{Xe}$  with a 2.5 hour irradiation was 155 Bq, 496 Bq for an 8 hour irradiation and 743 Bq for a 12 hour irradiation. The exposure during handling would require a different handling procedure that is not currently in place if a high activity sample was produced due to the gamma-ray release during the decay to  $^{127}\text{I}$ .

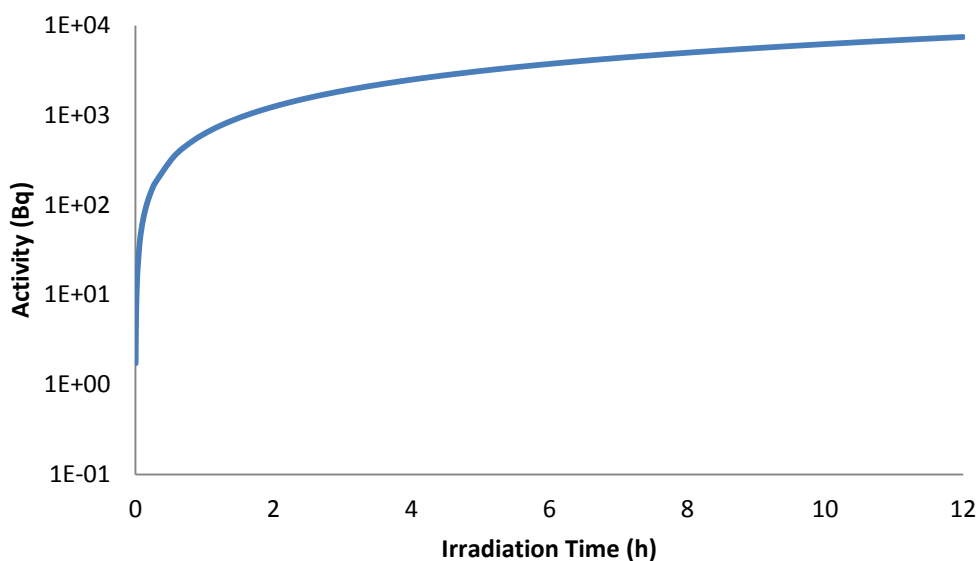


Figure 5.13. The activity curve of  $^{127}\text{Xe}$ .

The production estimate was much lower than anticipated. The difference was traced back to the CINDER90 cross-section library providing a lower value for the collapsed cross-section. The CINDER90 library includes only a single resonance peak, widened due to the large energy bins, and is similar to the ENDF VI.8 and JEFF 3.1 library. The more recent version of ENDF, VII.0 and VII.1, feature multiple resonance

peaks and starting at a lower energy level. This also agrees with the JENDL 4.0 and ROSFOND cross-sections (Shibata *et al.*, 2011; Zabrodskaya *et al.*, 2007). The JENDL 3.3 cross-section differs from all of the other cross-section libraries (Shibata *et al.*, 2002).

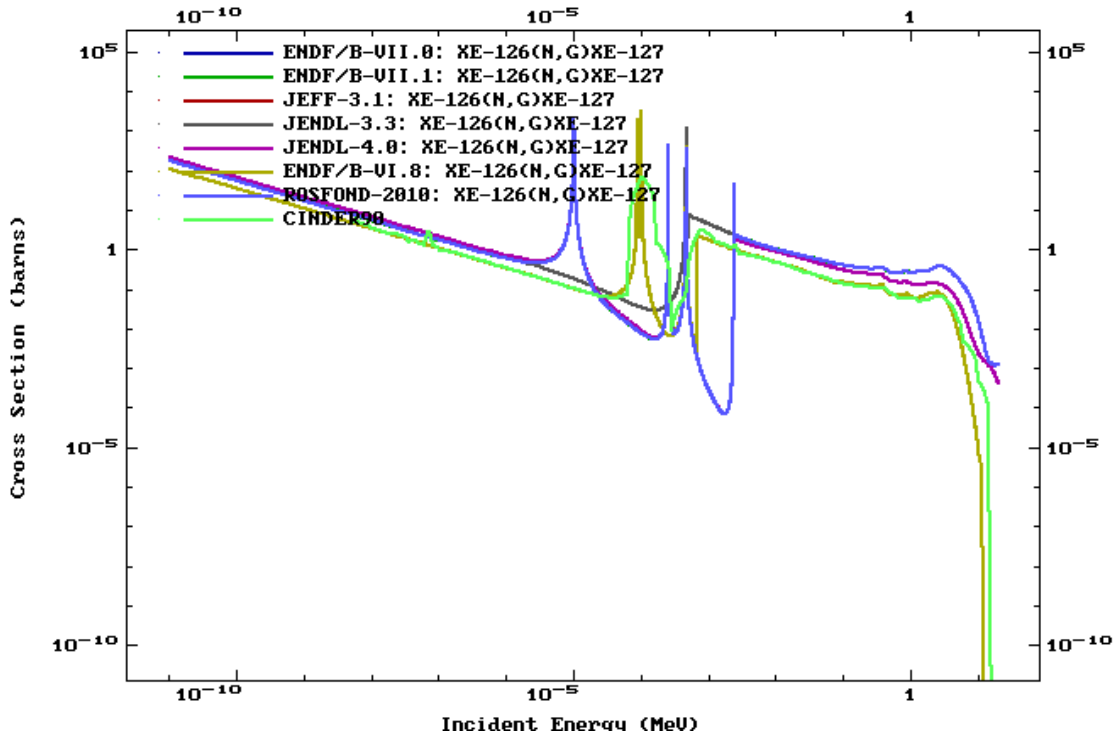


Figure 5.14. The  $^{126}\text{Xe}(n,\gamma)^{127}\text{Xe}$  reaction cross-sections (Chadwick *et al.*, 2006; Chadwick *et al.*, 2011; Koning *et al.*, 2006; Shibata *et al.*, 2002; Shibata *et al.*, 2011; Zabrodskaya *et al.*, 2007).

## CHAPTER 6: CONCLUSION

The production of radioargon was successful with the three methods. The gas irradiation methods proved to be an optimal fit for the mainly thermal flux of the UT TRIGA reactor. The computation model improved the approximation of the produced radioargon isotopes. The model also allowed for the examination of the developed large volume irradiation procedure for new radionuclide production experiments.

The UT TRIGA MCNPX reactor model improved the calculation of the induced radioargon activities of the radioargon isotopes that do not decay via gamma ray emission. However, the limiting factor of this method still is the cross-section libraries. Unfortunately the radioargon cross-section libraries do not agree (CINDER90 vs. JEFF 3.1). The groups that have done the most with the radioargon isotopes only have incomplete cross-section libraries. The future work of the model would include modifying the deck to use the BURN card and radioargon libraries generated with NJOY99.

The proven technique of irradiating  $0.58 \text{ cm}^3$  of a gas in the 3L canister was the starting point. This method has been used for years at NETL for radioxenon production and will continue with radioargon production. Irradiating natural argon gas in the Teflon vial produced a small amount of  $^{37}\text{Ar}$  with minimal impurities after the  $^{41}\text{Ar}$  had decayed. In order to produce a pure  $^{37}\text{Ar}$ , the use of enriched  $^{36}\text{Ar}$  gas could be used. The irradiation of an enriched gas will also provide a larger induced activity of the desired radioargon isotope with minimal impurities. The additional cost and activity required would need to be considered.

There was also  $^{37}\text{Ar}$  produced through the alternative method of irradiating calcium-containing compounds. The presence of  $^{41}\text{Ar}$  induced through  $^{44}\text{Ca}(n,\alpha)$  pathway,  $^{42}\text{K}$  through the  $^{42}\text{Ca}(n,p)$  pathway,  $^{43}\text{K}$  through the  $^{43}\text{Ca}(n,p)$  pathway and  $^{47}\text{Ca}$  through the  $^{46}\text{Ca}(n,\gamma)$  pathway allowed for the approximation of the  $^{37}\text{Ar}$  and  $^{39}\text{Ar}$  activities produced. The UT TRIGA MCNPX model predicted a  $^{37}\text{Ar}$  activity of  $1.156 \times 10^6$  Bq. Our production ratios with the experimental system estimated activities on the average of  $1.83 \times 10^6$  Bq. The UT TRIGA MCNPX model predicted  $^{39}\text{Ar}$  activity of  $7.68 \times 10^{-2}$  Bq, but the production ratios gave an average estimate of 0.122 Bq.

The lower experimental values are partially attributed to the unusual shape of the quartz sample, which would decrease the detector efficiency. The largest difference between the production ratio derived radioargon activities and the model activities was found using the  $^{41}\text{Ar}$  activity. The quartz ampoule remained sealed, so the distributions of activation products remain unknown. However, a few estimations were made to try to explain the deviation in activities in the generated by the production ratio UT TRIGA model calculations. Since  $^{41}\text{Ar}$  is a gas, it is assumed that the gas moved freely through the quartz ampoule. The potassium and  $^{47}\text{Ca}$  would be more likely to stay in the bottom of the ampoule with the white powder. Therefore, the effective length of the sample is shorter, which would improve the detection efficiency. For sample with different shapes, the efficiency calculation should consider the geometry.

The CINDER90 collapsed cross-section libraries did a better job of predicting the actual activity than the average fission spectrum reaction cross-sections. This can be seen by the closer radioargon activity calculations using  $^{47}\text{Ca}$  and  $^{43}\text{K}$  activities and

CINDDER90 cross-section libraries. This could show that the  $^{40}\text{Ca}(n,\alpha)^{37}\text{Ar}$  reaction cross-section should have the  $1/v$  thermal relationship, which both the ROSFOND and Riedmann and Purtschert (2011) use. It could also show the epithermal neutrons made a significant contribution to the reaction cross-section.

The irradiation of CaO for  $^{37}\text{Ar}$  production is not the optimal method for the UT TRIGA reactor. The 2 hour irradiation time and 500 kW power level used are the maximum time periods allowed for the Cd-lined 3L facility. Also, the radioargon separation procedure would include several liquid steps using nitric acid, which would in turn produce liquid radioactive waste. The waste streams are unnecessary and difficult to store. The irradiation of calcium-containing compounds for radioargon production is a viable method for fast reactors. Future  $^{37}\text{Ar}$  production should avoid this method considering the ease of gas irradiation using the thermal neutron spectra.

The large volume gas irradiation procedure was initially created to produce a 1 mBq sample of  $^{42}\text{Ar}$ . The majority of natural argon gas is  $^{40}\text{Ar}$ , the desired initial isotope, enriched gas was unnecessary. Therefore, there were considerable amounts of  $^{37}\text{Ar}$  and  $^{39}\text{Ar}$  produced due to the small percentage of  $^{36}\text{Ar}$  and  $^{38}\text{Ar}$  in natural argon gas. The initial experimental predictions were extremely low due to the underestimation of the flux by an order of magnitude and assuming only 40% of the gas, the length of the fuel, would experience the neutron fluence. After six months of storage, the shipping canister was shipped out. The induced activity of  $^{39}\text{Ar}$  provided a large enough sample for the use in an experiment. Also, the activity of  $^{37}\text{Ar}$  had reduced significantly; the  $^{41}\text{Ar}$  levels had decayed to levels below detection capabilities available at NETL.

The large volume gas irradiation procedure has also been considered for the production of other high activity samples. The production rates for a 12 hour irradiation in the 3L lead-lined canister at 950 kW was assumed. Also, all of the production methods used an enriched gas to provide the radionuclide of interest with minimal impurities from other isotopes. The production of high activity  $^{37}\text{Ar}$  sample with enriched  $^{36}\text{Ar}$  gas would produce a sample with an activity of  $2.64 \times 10^8$  Bq/L, or 4 mCi/g of argon. This activity per gram value is much lower than the neutrino groups use (Micheal *et al.*, 1984). Using an enriched  $^{38}\text{Ar}$  gas, the activity of the  $^{39}\text{Ar}$  in the sample would be  $5.51 \times 10^5$  Bq, or 5.97  $\mu\text{Ci/g}$  of argon. The production of  $^{127}\text{Xe}$  through the irradiation of  $^{126}\text{Xe}$  enriched gas would a sample with an activity of 743 Bq.

## Appendix A: Double-Ended Shipping Cylinder

### Sample Cylinders

#### Features

- Body made of seamless tubing provides consistent wall thickness, size, and capacity.
- Smooth internal neck transition allows easy cleaning and eliminates trapped fluids.
- Cold-formed female NPT threads provide greater strength.
- Heavy-wall end connections provide strength and resist flaring.
- Full-penetration gas tungsten arc-weld construction provides leak-tight sample containment.
- Swagelok® DOT sample cylinders conform to 49 CFR Part 178, "Specifications for Packagings."
- Swagelok Transport Canada (TC) sample cylinders conform to CAN/CSA B339, "Cylinders, Spheres, and Tubes for the Transportation of Dangerous Goods."

#### Single-Ended Cylinders

- 150, 300, and 500 cm<sup>3</sup> sizes meet a variety of sampling needs.
- 304L stainless steel construction resists intergranular corrosion.

#### Testing

DOT-4B 500 cylinders are hydrostatically proof tested at 1000 psig (69 bar) minimum.



#### Double-Ended Cylinders

- Sizes from 40 to 3785 cm<sup>3</sup> (1 gal)
- Working pressures up to 5000 psig (344 bar)
- 304L and 316L stainless steel materials resist intergranular corrosion.
- 304L and 316L stainless steel double-ended cylinders are available with dual certification to DOT and TC requirements.

#### Testing

Each DOT cylinder is hydrostatically tested to at least 5/3 the working pressure. All testing of DOT cylinders is witnessed by a DOT-approved independent inspection agency.

DOT-3E 1800/TC-3EM 124 cylinders are hydrostatically proof tested at 3050 psig (210 bar). One cylinder of each lot is burst tested.

DOT-3A 1800 and 5000/TC-3ASM 124 and 344 cylinders are marked with a serial number. Volumetric expansion of each cylinder during hydrostatic testing must be within the limits set by DOT Specification 3A and TC Specification 3ASM.

DOT-3A 1800/TC-3ASM 124 cylinders are hydrostatically proof tested at 3000 psig (206 bar) minimum.

DOT-3A 5000/TC-3ASM 344 cylinders are hydrostatically proof tested at 8500 psig (586 bar) minimum.

DOT-SP7458 1800 cylinders are hydrostatically proof tested at 3000 psig (206 bar).

⚠ It is the responsibility of the party filling the cylinder to have it retested by an approved facility, at the required intervals, in accordance with DOT and TC regulations.

### Pressure-Temperature Ratings

Ratings up to 100°F (37°C) are determined by DOT code. Ratings limited to 300°F (148°C) max with PTFE internal coating. Ratings may be limited by individual country government regulations.

Material	316L SS	316L SS, 304L SS	304L SS	Alloy 400	316 SS	304L SS
Specification	DOT-3A 5000 TC-3ASM 344	DOT-3E 1800 TC-3EM 124	DOT-3A 1800 TC-3ASM 124	DOT-SP7458 1800	None	DOT-4B 500
Temperature, °F (°C)	Working Pressure, psig (bar)					
-65 (-53) to 100 (37)	5000 (344)	1800 (124)	1800 (124)	1800 (124)	1000 (68.9)	500 (34.4)
200 (93)	3960 (272)	1360 (93.7)	1360 (93.7)	1580 (108)	840 (57.8)	500 (34.4)
300 (148)	3570 (245)	1230 (84.7)	1230 (84.7)	1490 (102)	760 (52.3)	500 (34.4)
400 (204)	3290 (226)	1130 (77.8)	1130 (77.8)	1430 (98.5)	700 (48.2)	500 (34.4)
500 (260)	3060 (210)	1050 (72.3)	1050 (72.3)	1420 (97.8)	650 (44.7)	500 (34.4)
600 (315)	2920 (201)	1000 (68.9)	1000 (68.9)	1420 (97.8)	620 (42.7)	500 (34.4)
650 (343)	2870 (197)	980 (67.5)	980 (67.5)	1420 (97.8)	610 (42.0)	500 (34.4)
700 (371)	2810 (193)	970 (66.8)	970 (66.8)	1420 (97.8)	590 (40.6)	500 (34.4)
750 (398)	2750 (189)	950 (65.4)	950 (65.4)	1410 (97.1)	580 (39.9)	500 (34.4)
800 (426)	2700 (186)	930 (64.0)	930 (64.0)	—	570 (39.2)	500 (34.4)
850 (454)	2640 (181)	—	—	—	560 (38.5)	—

### Transportable Pressure Equipment Directive (TPED)

The Transportable Pressure Equipment Directive (TPED) provides requirements relating to the design, manufacture, and testing of transportable pressure vessels and accessories, including sample cylinders and rupture discs. The intent of the directive is to provide a uniform level of product safety throughout the European Union countries.

For information about TPED-compliant Swagelok products, see the *Swagelok Products Compliant with the Transportable Pressure Equipment Directive* catalog, MS-02-193.

## APPENDIX B: KNF 4-STAGE TRANSFER PUMP

### Diaphragm Compressors and Vacuum Pumps for Gases and Vapours

#### Pump Principle:

- diaphragm pump

#### Special Pump Feature:

- depending on the type of pump, the components in contact with media are corrosion-resistant

#### Applications:

- transfer, evacuation and compression of air and neutral, slightly aggressive and slightly corrosive gases and vapours.
- Vacuum pump for damp gases with KNF self-drying system, for example with vacuum drying or steam sterilization.

#### Performance Range: Micro Diaphragm Gas Sampling Pumps

- flow rate: from 0.5 l/min up to 4 l/min (at atm. pressure)
- ultimate vacuum: down to 240 mbar abs.
- maximum pressure: up to 1 bar g

#### Diaphragm Compressors and Vacuum Pumps

- flow rate: up to 300 l/min (at atm. pressure)
- ultimate vacuum: down to 0.5 mbar abs.
- maximum pressure: up to 12 bar g



**N 836.3 APE**  
Diaphragm vacuum pump with KNF self-drying system, air- and water-cooled heads for the vacuum drying



**N 813.4 ANE**  
Four head diaphragm vacuum pump e.g. used as roughing pump



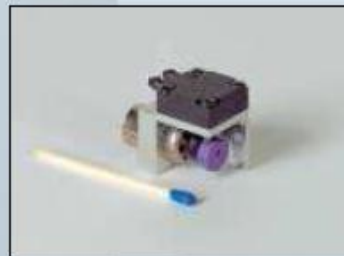
**N 828 KNDC**  
Mini diaphragm vacuum pump e.g. for the medical equipment



**N 96 KNDC**      **N 96 KNE**

**N 95.3 KNDC**

Mini diaphragm pumps – easy installation in to devices, units and plants e. g. medical equipment



**NMP 05M**  
Micro diaphragm gas sampling pump e.g. for the analytical technology



**N813.4ANI Model shown**

## Types: N813.3/.4/.5ANI

### Diaphragm Vacuum Pump and Compressor



**Two, Three or Four-Stage  
Deep Vacuum, High Flow  
OEM Installation Model  
with AC TENV Motor**

Max Free-Flow Capacity (.5 model): 19 liters/minute (.67 SCFM)  
Maximum End Vacuum (.4 model): <0.5 mbar (.375 Torr)  
Maximum Continuous Pressure: 1 bar (15 psig)

#### Description

The N813 series deep vacuum diaphragm pumps from KNF are optimized for efficiency and durability using the latest CAD/FEA methods. Featuring KNF's patented, structured diaphragm and multi-port valve system, they provide the best vacuum performance and reliability available in their size range. The four-head model is configured for either deeper vacuum (.4) or greater flow (.5). These pumps will restart under full vacuum load.

#### Features

- **Advanced Multi-Port Valve System** - KNF's new multi-port valve system consists of a circle of smaller holes covered by an elastomeric disk. Pump capacity is increased, and tolerance to occasional condensate droplets is greatly improved.
- **Patented, Structural Molded Diaphragm** - Using computer analysis, KNF engineers molded a structure into the diaphragm that distributes mechanical stresses over a wide area. This provides precision control of flexibility and power, thus improving performance and lifetime. There is no metal clamping disk, eliminating a source of leaks and corrosion.
- **Flexible Design** - KNF's engineers combine high performance with a small physical package to produce an efficient, compact standard unit. In addition, with KNF's Project Pump program, we can suggest a variety of inexpensive modifications to meet your OEM design requirements. NPT port threads are available. Talk to us about your design requirements.
- **Medium Transfer is Contamination-Free** - KNF's diaphragm design is oil-free and has no sliding seals to wear away. Your pumped medium always stays analytically pure.
- **Low Noise Level** - The enclosed compressor housing minimizes noise transmission and keeps dirt away from critical components. The pump is extremely quiet and smooth running. The totally enclosed (IP-44), non-ventilated (TENV) motor is equipped with ball bearings to assure quiet, trouble-free operation and will restart under full vacuum load.
- **Factory-Mounted & Wired Motor Capacitor** - Unlike others who leave these details to you, KNF pumps are tested completely assembled and install quickly.
- **Variety of Accessories** - Available accessories include mufflers and hose connectors. Contact KNF applications department for details.

#### Applications

- High Vacuum Roughing Pump
- Mass Spectrometers
- Vacuum Drying
- De-gassing of Liquids
- Vacuum Filtration
- Dental Vacuum Ovens
- Residual Gas Analyzers
- Ion Milling Operations

# N813.3/4/5ANI

## KNF Performance Specifications

Model Number	N813.3ANI	N813.4ANI	N813.5ANI
Feature	Moderate End Vacuum	Deep End Vacuum	High Flow, Moderate Vacuum
Head Configuration	Two-Stage	Four-Stage	Three-Stage/Parallel Head
Maximum Flow	13 liters/min. (0.46 SCFM)	13 liters/min. (0.46 SCFM)	19 liters/min. (0.67 SCFM)
Maximum Vacuum	3 mbar abs. (2.25 Torr)	<0.5 mbar (0.375 Torr)	<1 mbar (0.75 Torr)
Maximum Continuous Pressure	1 bar (15 psig)	1 bar (15 psig)	1 bar (15 psig)

## Electrical/Mechanical

Motor Voltage & Frequency	115 VAC (60 Hz)	230 VAC (50 Hz)
Full Load Motor Current	0.8 Amps	0.5 Amps
Motor Type	Totally-Enclosed, Non-Ventilated, Permanent Split-Capacitor Motor	
Motor Protection	Thermal Reset (IP-44)	

## Environmental

Maximum Medium Temperature	40°C (105°F)
Maximum Ambient Temperature	40°C (105°F)
Net Weight	5.9 kg (13 lbs.)      7.5 kg (17 lb.)      7.5 kg (17 lb.)

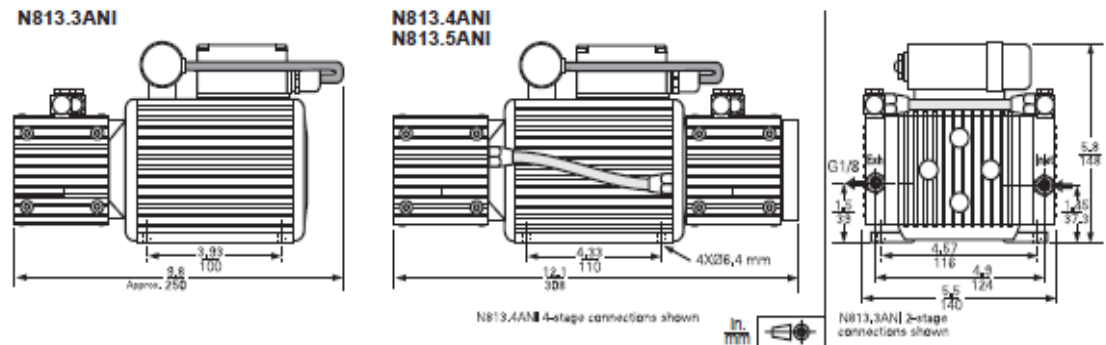
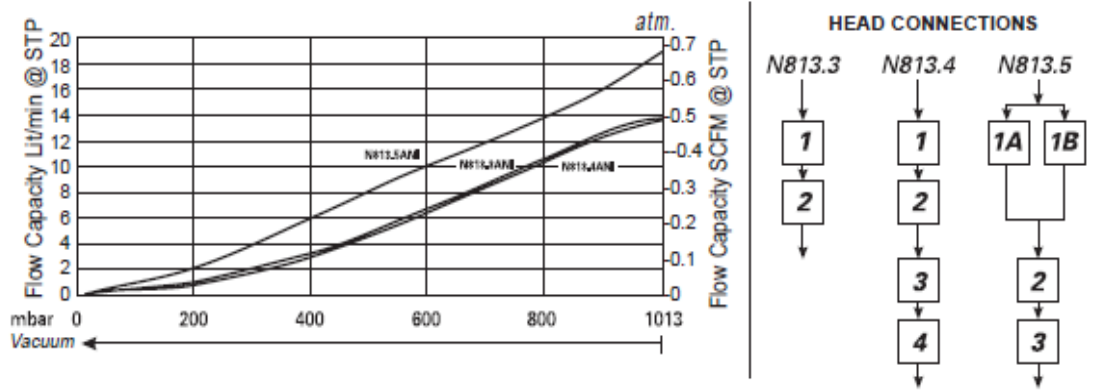
## Materials of Construction

Head	Aluminum
Valves	EPDM
Diaphragm	Neoprene

**Note:** Standard continuous performance ratings are based on technical data and test results of nominal units at sea level with an ambient temperature of 70°F (21°C) and nominal electrical supply are listed above. Dimensions and performance characteristics given are for reference only. Higher performance models, cost efficient OEM modifications, motor options and different materials of construction may be available. Specifications subject to change without notice.

**Accessories:** Hose Connectors, Silencer, Shock Mounts, NPT port threads available.

## Performance Characteristics/Outline Dimensions:



## APPENDIX C: CHECK VALVE



**Part No.**

SS-4C-25

**Part Description:**

SS Poppet Check Valve, Fixed Pressure, 1/4 in. Swagelok Tube Fitting, 25 psig (1.8 bar)

### Product Specifications

General	
Valve Material	316 Stainless Steel
End Connection 1 Size	1/4 in
End Connection 1 Type	Swagelok® tube fitting
End Connection 2 Size	1/4 in
End Connection 2 Type	Swagelok® tube fitting
Approval	No Approval
Cleaning	Swagelok SC-10
Cracking Pressure	25 PSI
Lubricant	Dow Vacuum
Seal Material	Fluorocarbon FKM
Spring Coating	None
Surface Finish	Standard
Testing	No Optional Testing
Max Temperature Pressure Rating	375°F @ 2185 PSIG /190°C @ 150 BAR
Room Temperature Pressure Rating	3000 PSIG @ 100°F /206 @ BAR 37°C

## APPENDIX D: UT TRIGA MCNPX REACTOR MODEL

```

----- UT-TRIGA - Core Model - 12/16/2011 -----
c
c Coordinate origin on core axis at core midplane
c - Experiment tubes, empty beam ports, empty RSR
c - Central thimble fixed and flooded with no sample
c - Core fully fuelled
c
c -----
c Beginning of Cell Card Specification
c -----
c -----
c Core region
c -----
1099 1 -1.0 -202 +206
      -231 +232 -233 +234 -235 +236
      -241 +242 -243 +244 -245 +246
      +5000 +5001 +5002 +5003 +5004 +5005 +5006 +5007 +5008 +5009
      +5010 +5011 +5012 +5013 +5014 +5015 +5016 +5017 +5018 +5019
      +5020 +5021 +5022 +5023 +5024 +5025 +5026 +5027 +5028 +5029
      +5030 +5031 +5032 +5033 +5034 +5035 +5036 +5037 +5038 +5039
      +5040 +5041 +5042 +5043 +5044 +5045 +5046 +5048 +5049
      +5050 +5051 +5052 +5053 +5054 +5055 +5056 +5057 +5058 +5059
      +5060 +5061 +5062 +5063 +5064 +5065 +5066 +5067 +5068 +5069
      +5070 +5071 +5072 +5075 +5076 +5077 +5078 +5079
      +5080 +5081 +5082 +5083 +5084 +5085 +5086 +5087 +5088 +5089
      +5090 +5091 +5092 +5093 +5094 +5095 +5096 +5097 +5098 +5099
      +5100 +5102 +5103 +5104 +5105 +5106 +5107 +5108 +5109
      +5110 +5112 +5113 +5114 +5117 +5119
      +5120
      +1963 +1964 +1965 +1966 $ Mapping experiment
      +1940 $ 3L
      +2000 +2001 +2002 +2003 +2004 +2005 +2006
520 0 -201 +207 -1963 fill=101 (10) $ Flux mapping water cells
521 0 -201 +207 -1964 fill=101 (11)
522 0 -201 +207 -1965 fill=101 (12)
523 0 -201 +207 -1966 fill=101 (13)
600 0 -110 +120 -5000 fill=82 (100) $ A1
601 0 -110 +120 -5001 fill=8 (101) $ B1
602 0 -110 +120 -5002 fill=8 (102) $ B2
603 0 -110 +120 -5003 fill=8 (103) $ B3
604 0 -110 +120 -5004 fill=8 (104) $ B4
605 0 -110 +120 -5005 fill=8 (105) $ B5
606 0 -110 +120 -5006 fill=8 (106) $ B6
607 0 -110 +120 -5007 fill=7 (107) $ C1
608 0 -110 +120 -5008 fill=8 (108) $ C2
609 0 -110 +120 -5009 fill=8 (109) $ C3
610 0 -110 +120 -5010 fill=8 (110) $ C4
611 0 -110 +120 -5011 fill=8 (111) $ C5
612 0 -110 +120 -5012 fill=8 (112) $ C6
613 0 -110 +120 -5013 fill=9 (113) $ C7
614 0 -110 +120 -5014 fill=8 (114) $ C8
615 0 -110 +120 -5015 fill=8 (115) $ C9
616 0 -110 +120 -5016 fill=8 (116) $ C10
617 0 -110 +120 -5017 fill=8 (117) $ C11
618 0 -110 +120 -5018 fill=8 (118) $ C12
619 0 -110 +120 -5019 fill=8 (119) $ D1
620 0 -110 +120 -5020 fill=8 (120) $ D2
621 0 -110 +120 -5021 fill=8 (121) $ D3
622 0 -110 +120 -5022 fill=8 (122) $ D4
623 0 -110 +120 -5023 fill=8 (123) $ D5
624 0 -110 +120 -5024 fill=9 (124) $ D6
625 0 -110 +120 -5025 fill=8 (125) $ D7
626 0 -110 +120 -5026 fill=8 (126) $ D8
627 0 -110 +120 -5027 fill=8 (127) $ D9
628 0 -110 +120 -5028 fill=8 (128) $ D10
629 0 -110 +120 -5029 fill=8 (129) $ D11
630 0 -110 +120 -5030 fill=8 (130) $ D12
631 0 -110 +120 -5031 fill=8 (131) $ D13
632 0 -110 +120 -5032 fill=9 (132) $ D14
633 0 -110 +120 -5033 fill=8 (133) $ D15
634 0 -110 +120 -5034 fill=8 (134) $ D16
635 0 -110 +120 -5035 fill=8 (135) $ D17

```

636 0 -110 +120 -5036 fill=8 (136) \$ D18  
637 0 -110 +120 -5037 fill=8 (137) \$ E1  
638 0 -110 +120 -5038 fill=8 (138) \$ E2  
639 0 -110 +120 -5039 fill=8 (139) \$ E3  
640 0 -110 +120 -5040 fill=8 (140) \$ E4  
641 0 -110 +120 -5041 fill=8 (141) \$ E5  
642 0 -110 +120 -5042 fill=8 (142) \$ E6  
643 0 -110 +120 -5043 fill=8 (143) \$ E7  
644 0 -110 +120 -5044 fill=8 (144) \$ E8  
645 0 -110 +120 -5045 fill=8 (145) \$ E9  
646 0 -110 +120 -5046 fill=8 (146) \$ E10  
648 0 -110 +120 -5048 fill=8 (148) \$ E12  
649 0 -110 +120 -5049 fill=8 (149) \$ E13  
650 0 -110 +120 -5050 fill=8 (150) \$ E14  
651 0 -110 +120 -5051 fill=8 (151) \$ E15  
652 0 -110 +120 -5052 fill=8 (152) \$ E16  
653 0 -110 +120 -5053 fill=8 (153) \$ E17  
654 0 -110 +120 -5054 fill=8 (154) \$ E18  
655 0 -110 +120 -5055 fill=8 (155) \$ E19  
656 0 -110 +120 -5056 fill=8 (156) \$ E20  
657 0 -110 +120 -5057 fill=8 (157) \$ E21  
658 0 -110 +120 -5058 fill=8 (158) \$ E22  
659 0 -110 +120 -5059 fill=8 (159) \$ E23  
660 0 -110 +120 -5060 fill=8 (160) \$ E24  
661 0 -110 +120 -5061 fill=8 (161) \$ F1  
662 0 -110 +120 -5062 fill=8 (162) \$ F2  
663 0 -110 +120 -5063 fill=8 (163) \$ F3  
664 0 -110 +120 -5064 fill=8 (164) \$ F4  
665 0 -110 +120 -5065 fill=8 (165) \$ F5  
666 0 -110 +120 -5066 fill=8 (166) \$ F6  
667 0 -110 +120 -5067 fill=8 (167) \$ F7  
668 0 -110 +120 -5068 fill=8 (168) \$ F8  
669 0 -110 +120 -5069 fill=8 (169) \$ F9  
670 0 -110 +120 -5070 fill=8 (170) \$ F10  
671 0 -110 +120 -5071 fill=8 (171) \$ F11  
672 0 -110 +120 -5072 fill=8 (172) \$ F12  
675 0 -110 +120 -5075 fill=8 (175) \$ F15  
676 0 -110 +120 -5076 fill=8 (176) \$ F16  
677 0 -110 +120 -5077 fill=8 (177) \$ F17  
678 0 -110 +120 -5078 fill=8 (178) \$ F18  
679 0 -110 +120 -5079 fill=8 (179) \$ F19  
680 0 -110 +120 -5080 fill=8 (180) \$ F20  
681 0 -110 +120 -5081 fill=8 (181) \$ F21  
682 0 -110 +120 -5082 fill=8 (182) \$ F22  
683 0 -110 +120 -5083 fill=8 (183) \$ F23  
684 0 -110 +120 -5084 fill=8 (184) \$ F24  
685 0 -110 +120 -5085 fill=8 (185) \$ F25  
686 0 -110 +120 -5086 fill=8 (186) \$ F26  
687 0 -110 +120 -5087 fill=8 (187) \$ F27  
688 0 -110 +120 -5088 fill=8 (188) \$ F28  
689 0 -110 +120 -5089 fill=8 (189) \$ F29  
690 0 -110 +120 -5090 fill=8 (190) \$ F30  
691 0 -110 +120 -5091 fill=6 (191) \$ G2 - Graphite  
692 0 -110 +120 -5092 fill=8 (192) \$ G3  
693 0 -110 +120 -5093 fill=8 (193) \$ G4  
694 0 -110 +120 -5094 fill=8 (194) \$ G5  
695 0 -110 +120 -5095 fill=8 (195) \$ G6  
696 0 -110 +120 -5096 fill=8 (196) \$ G8  
697 0 -110 +120 -5097 fill=8 (197) \$ G9  
698 0 -110 +120 -5098 fill=8 (198) \$ G10  
699 0 -110 +120 -5099 fill=8 (199) \$ G11  
700 0 -110 +120 -5100 fill=8 (200) \$ G12  
702 0 -110 +120 -5102 fill=8 (202) \$ G15  
703 0 -110 +120 -5103 fill=6 (203) \$ G16 - Graphite  
704 0 -110 +120 -5104 fill=8 (204) \$ G17  
705 0 -110 +120 -5105 fill=8 (205) \$ G18  
706 0 -110 +120 -5106 fill=6 (206) \$ G20 - Graphite  
707 0 -110 +120 -5107 fill=8 (207) \$ G21  
708 0 -110 +120 -5108 fill=8 (208) \$ G22  
709 0 -110 +120 -5109 fill=8 (209) \$ G23  
710 0 -110 +120 -5110 fill=6 (210) \$ G24 - Graphite  
712 0 -110 +120 -5112 fill=8 (212) \$ G27  
713 0 -110 +120 -5113 fill=8 (213) \$ G28  
714 0 -110 +120 -5114 fill=8 (214) \$ G29  
717 0 -110 +120 -5117 fill=6 (217) \$ G33 - Graphite  
719 0 -110 +120 -5119 fill=6 (219) \$ G35 - Graphite

```

720 0 -110 +120 -5120 fill=6 (220) $ G36 - Graphite
751 0 -110 +120 -1940 fill=45 (50) $ 3L(Cd) irradiator
c -----
c Lower grid plate region
c -----
1 2 -2.7 -206 +207
    -211 +212 -213 +214 -215 +216
    -221 +222 -223 +224 -225 +226
+5000 +5001 +5002 +5003 +5004 +5005 +5006 +5007 +5008 +5009
+5010 +5011 +5012 +5013 +5014 +5015 +5016 +5017 +5018 +5019
+5020 +5021 +5022 +5023 +5024 +5025 +5026 +5027 +5028 +5029
+5030 +5031 +5032 +5033 +5034 +5035 +5036 +5037 +5038 +5039
+5040 +5041 +5042 +5043 +5044 +5045 +5046 +5048 +5049
+5050 +5051 +5052 +5053 +5054 +5055 +5056 +5057 +5058 +5059
+5060 +5061 +5062 +5063 +5064 +5065 +5066 +5067 +5068 +5069
+5070 +5071 +5072 +5075 +5076 +5077 +5078 +5079
+5080 +5081 +5082 +5083 +5084 +5085 +5086 +5087 +5088 +5089
+5090 +5091 +5092 +5093 +5094 +5095 +5096 +5097 +5098 +5099
+5100 +5102 +5103 +5104 +5105 +5106 +5107 +5108 +5109
+5110 +5112 +5113 +5114 +5117 +5119
+5120
+1963 +1964 +1965 +1966 $ Mapping experiment
+1940 $ 3L
c +5118 $ PNT
c +5111 +5115
c +5039 +5040 +5063 +5064 +5065 +5093 +5094 $ Elements in 6L
c +961 $ 3L
c
c -----
c Upper grid plate region
c -----
2 2 -2.7 -203 -201 +202
+5000 +5001 +5002 +5003 +5004 +5005 +5006 +5007 +5008 +5009
+5010 +5011 +5012 +5013 +5014 +5015 +5016 +5017 +5018 +5019
+5020 +5021 +5022 +5023 +5024 +5025 +5026 +5027 +5028 +5029
+5030 +5031 +5032 +5033 +5034 +5035 +5036 +5037 +5038 +5039
+5040 +5041 +5042 +5043 +5044 +5045 +5046 +5048 +5049
+5050 +5051 +5052 +5053 +5054 +5055 +5056 +5057 +5058 +5059
+5060 +5061 +5062 +5063 +5064 +5065 +5066 +5067 +5068 +5069
+5070 +5071 +5072 +5075 +5076 +5077 +5078 +5079
+5080 +5081 +5082 +5083 +5084 +5085 +5086 +5087 +5088 +5089
+5090 +5091 +5092 +5093 +5094 +5095 +5096 +5097 +5098 +5099
+5100 +5102 +5103 +5104 +5105 +5106 +5107 +5108 +5109
+5110 +5112 +5113 +5114 +5117 +5119
+5120
+1963 +1964 +1965 +1966 $ Mapping experiment
+1940 $ 3L
c
c -----
c Reactor core structure
c -----
c Inner core shroud
c -----
10 2 -2.7 -300 +302 -303 +202 $ Alignment ring
11 2 -2.7 -300 -202 +352 $ Alignment ring
    (+231: -232: +241: -242:
    +233: -234: +243: -244:
    +235: -236: +245: -246)
12 2 -2.7 +305 -306 +307 $ Shroud load ring
    (-311 +312 -321 +322
    -313 +314 -323 +324
    -315 +316 -325 +326)
13 2 -2.7 -301 -352 +304 $ Alignment ring
    (+331: -332: +341: -342:
    +333: -334: +343: -344:
    +335: -336: +345: -346)
14 2 -2.7 +231 -331 -233 +236 $ Reflector plate
    -352 +306
15 2 -2.7 -232 +332 +234 -235 $ Reflector plate
    -352 +306
16 2 -2.7 +241 -341 -343 -345 $ Reflector, bp3
    -352 +306 +363
17 2 -2.7 -242 +342 +344 +346 $ Reflector plate
    -352 +306
18 2 -2.7 +233 -333 -331 -343 $ Reflector plate
    -352 +306

```

19 2 -2.7 -234 +334 +332 +344 \$ Reflector plate  
-352 +306  
20 2 -2.7 +235 -335 +332 -345 \$ Reflector plate  
-352 +306  
21 2 -2.7 -236 +336 -331 +346 \$ Reflector plate  
-352 +306  
22 2 -2.7 +243 -343 -241 -233 \$ Reflector plate  
-352 +306  
23 2 -2.7 -244 +344 +242 +234 \$ Reflector plate  
-352 +306  
24 2 -2.7 +245 -345 -241 -235 \$ Reflector plate  
-352 +306  
25 2 -2.7 -246 +346 +242 +236 \$ Reflector plate  
-352 +306  
26 2 -2.7 +241 -363 +364 -360 \$ Reflector BP3  
27 2 -2.7 -361 +362 -100 \$ Reflector BP1&5  
c  
c -----  
c Reflector outer shroud structure  
c -----  
30 2 -2.7 -355 +361 \$ Reflector cylin  
-350 +351 -352 +353  
31 2 -2.7 +355 +363 \$ Reflector cylin  
-350 +351 -352 +353  
32 2 -2.7 -370 +371 -372 +373 \$ Cylinder, top  
33 2 -2.7 -374 -375 +376 \$ Cylinder, bot  
(+331: -332: +341: -342:  
+333: -334: +343: -344:  
+335: -336: +345: -346)  
34 2 -2.7 -370 +374 -375 +377 \$ Reflector edge ring  
35 2 -2.7 -352 -371 +380 +381 \$ Reflector RSR unit  
36 2 -2.7 -380 +300 +381 -382 \$ Reflector RSR unit  
37 2 -2.7 -352 +301 -300 +381 \$ Reflector RSR unit  
38 1 -1.0 +370 -351 -377 +120 \$ Edge ring error  
c  
c -----  
c Reflector graphite moderator  
c -----  
40 4 -2.25 -400 +401 -402 +403 \$ Reflector graphite  
41 4 -2.25 -400 -403 +375 -404 +361  
(+411: -412: +421: -422:  
+413: -414: +423: -424:  
+415: -416: +425: -426)  
#(-361 +405) \$ Graphite, bp1&5  
42 4 -2.25 (-400 -403 +375 +404 +363  
(+411: -412: +421: -422:  
+413: -414: +423: -424:  
+415: -416: +425: -426))  
#(-406 +408) #(-407 +409) \$ Graphite, bp3  
43 8 -1.15e-3 (+371 -351 -373 +403) #40 \$ Graphite void  
44 8 -1.15e-3 (-351 -403 +375 -404 +361  
(+331: -332: +341: -342:  
+333: -334: +343: -344:  
+335: -336: +345: -346)) #41 \$ graphite void  
45 8 -1.15e-3 (-351 -403 +375 +404 +363  
(+331: -332: +341: -342:  
+333: -334: +343: -344:  
+335: -336: +345: -346)) #42 \$ graphite void  
46 8 -1.15e-3 -304 +403 -301  
(+331: -332: +341: -342:  
+333: -334: +343: -344:  
+335: -336: +345: -346) \$ graphite void  
47 8 -1.15e-3 +301 -371 +403 -381 \$ graphite void  
c  
c -----  
c Pool coolant water  
c -----  
50 1 -1.0 -203 +201 -110 \$ Above upper grid plate  
+5000 +5001 +5002 +5003 +5004 +5005 +5006 +5007 +5008 +5009  
+5010 +5011 +5012 +5013 +5014 +5015 +5016 +5017 +5018 +5019  
+5020 +5021 +5022 +5023 +5024 +5025 +5026 +5027 +5028 +5029  
+5030 +5031 +5032 +5033 +5034 +5035 +5036 +5037 +5038 +5039  
+5040 +5041 +5042 +5043 +5044 +5045 +5046 +5048 +5049  
+5050 +5051 +5052 +5053 +5054 +5055 +5056 +5057 +5058 +5059  
+5060 +5061 +5062 +5063 +5064 +5065 +5066 +5067 +5068 +5069  
+5070 +5071 +5072 +5075 +5076 +5077 +5078 +5079

+5080 +5081 +5082 +5083 +5084 +5085 +5086 +5087 +5088 +5089  
 +5090 +5091 +5092 +5093 +5094 +5095 +5096 +5097 +5098 +5099  
 +5100 +5102 +5103 +5104 +5105 +5106 +5107 +5108 +5109  
 +5110 +5112 +5113 +5114 +5117 +5119  
 +5120  
 +1940 § 3L  
 51 1 -1.0 +203 -302 +202 -110 \$ Upper gridplate  
 52 1 -1.0 +302 -300 +303 -110 \$ Upper gridplate  
 53 1 -1.0 -305 -306 +307 \$ Lower gridplate  
 +5000 +5001 +5002 +5003 +5004 +5005 +5006 +5007 +5008 +5009  
 +5010 +5011 +5012 +5013 +5014 +5015 +5016 +5017 +5018 +5019  
 +5020 +5021 +5022 +5023 +5024 +5025 +5026 +5027 +5028 +5029  
 +5030 +5031 +5032 +5033 +5034 +5035 +5036 +5037 +5038 +5039  
 +5040 +5041 +5042 +5043 +5044 +5045 +5046 +5048 +5049  
 +5050 +5051 +5052 +5053 +5054 +5055 +5056 +5057 +5058 +5059  
 +5060 +5061 +5062 +5063 +5064 +5065 +5066 +5067 +5068 +5069  
 +5070 +5071 +5072 +5075 +5076 +5077 +5078 +5079  
 +5080 +5081 +5082 +5083 +5084 +5085 +5086 +5087 +5088 +5089  
 +5090 +5091 +5092 +5093 +5094 +5095 +5096 +5097 +5098 +5099  
 +5100 +5102 +5103 +5104 +5105 +5106 +5107 +5108 +5109  
 +5110 +5112 +5113 +5114 +5117 +5119  
 +5120  
 +1940 § 3L  
 54 1 -1.0 -307 +120 \$ Lower gridplate  
 (-311 +312 -321 +322  
 -313 +314 -323 +324  
 -315 +316 -325 +326)  
 +5000 +5001 +5002 +5003 +5004 +5005 +5006 +5007 +5008 +5009  
 +5010 +5011 +5012 +5013 +5014 +5015 +5016 +5017 +5018 +5019  
 +5020 +5021 +5022 +5023 +5024 +5025 +5026 +5027 +5028 +5029  
 +5030 +5031 +5032 +5033 +5034 +5035 +5036 +5037 +5038 +5039  
 +5040 +5041 +5042 +5043 +5044 +5045 +5046 +5048 +5049  
 +5050 +5051 +5052 +5053 +5054 +5055 +5056 +5057 +5058 +5059  
 +5060 +5061 +5062 +5063 +5064 +5065 +5066 +5067 +5068 +5069  
 +5070 +5071 +5072 +5075 +5076 +5077 +5078 +5079  
 +5080 +5081 +5082 +5083 +5084 +5085 +5086 +5087 +5088 +5089  
 +5090 +5091 +5092 +5093 +5094 +5095 +5096 +5097 +5098 +5099  
 +5100 +5102 +5103 +5104 +5105 +5106 +5107 +5108 +5109  
 +5110 +5112 +5113 +5114 +5117 +5119  
 +5120  
 +1940 § 3L  
 55 1 -1.0 -207 +306 \$ Lower gridplate  
 (-231 +232 -241 +242  
 -233 +234 -243 +244  
 -235 +236 -245 +246)  
 +5000 +5001 +5002 +5003 +5004 +5005 +5006 +5007 +5008 +5009  
 +5010 +5011 +5012 +5013 +5014 +5015 +5016 +5017 +5018 +5019  
 +5020 +5021 +5022 +5023 +5024 +5025 +5026 +5027 +5028 +5029  
 +5030 +5031 +5032 +5033 +5034 +5035 +5036 +5037 +5038 +5039  
 +5040 +5041 +5042 +5043 +5044 +5045 +5046 +5048 +5049  
 +5050 +5051 +5052 +5053 +5054 +5055 +5056 +5057 +5058 +5059  
 +5060 +5061 +5062 +5063 +5064 +5065 +5066 +5067 +5068 +5069  
 +5070 +5071 +5072 +5075 +5076 +5077 +5078 +5079  
 +5080 +5081 +5082 +5083 +5084 +5085 +5086 +5087 +5088 +5089  
 +5090 +5091 +5092 +5093 +5094 +5095 +5096 +5097 +5098 +5099  
 +5100 +5102 +5103 +5104 +5105 +5106 +5107 +5108 +5109  
 +5110 +5112 +5113 +5114 +5117 +5119  
 +5120  
 +1940 § 3L  
 56 1 -1.0 -206 +207 \$ Lower gridplate  
 (+211: -212: +221: -222:  
 +213: -214: +223: -224:  
 +215: -216: +225: -226)  
 (-231 +232 -241 +242  
 -233 +234 -243 +244  
 -235 +236 -245 +246)  
 57 1 -1.0 -351 +371 +372 -110 \$ Upper reflector  
 58 1 -1.0 -374 -376 +120 \$ Lower reflector  
 (+311: -312: +321: -322:  
 +313: -314: +323: -324:  
 +315: -316: +325: -326)  
 59 1 -1.0 +306 -376 \$ Lower reflector  
 (+331: -332: +341: -342:  
 +333: -334: +343: -344:  
 +335: -336: +345: -346)  
 (-311 +312 -321 +322

```

-313 +314 -323 +324
-315 +316 -325 +326)
c
c -----
c Pool coolant water
c -----
950 8 -1.15e-3 -150 +160 -165
*TRCL (-60.00 00.00 00.00 00 90 90 90 00 90) $NP
951 8 -1.15e-3 -150 +160 -165
*TRCL ( 57.96 -15.53 00.00 00 90 90 90 00 90) $NPP
952 8 -1.15e-3 -150 +160 -165
*TRCL ( 42.43  42.43 00.00 00 90 90 90 00 90) $FC
60 1 -1.0 +350 -355 +361
(-100 -110 +120) #950 #951 $ Beam ports 1&5
61 1 -1.0 +350 +355 +363
(-100 -110 +120) #950 #952
#(-406 +408) #(-407 +409) $ Beam ports 2&4
62 1 -1.0 -363 +364 +360 -100 $ Reflector BP3
63 1 -1.0 -350 +351 +352 -110 $ Reflector cylinder
64 1 -1.0 -350 +351 -353 +120 $ Reflector cylinder
65 1 -1.0 -370 +374 -377 +120 $ Reflector edgering
66 1 -1.0 +300 -371 +303 -110 $ RSR removal
67 2 -2.7 +370 -351 -375 +377 $ edge ring error
68 2 -2.7 -351 +370 -372 +373 $ edge ring error
c -----
c BP2, BP4 structure
c -----
71 2 -2.7 (-406 +430) +350 +355 -100 $ Reflector BP2
72 2 -2.7 (-407 +440) +350 +355 -100 $ Reflector BP4
c -----
c BP3 structure
c -----
73 2 -2.7 +461 -462 -464 $ Reflector BP3
74 2 -2.7 -463 +464 +461 -100 $ Reflector BP3
75 1 -1.0 +241 -364 -461 $ Reflector BP3
76 1 -1.0 +463 -364 +461 -100 $ Reflector BP3
c -----
c BP1, BP3, BP5 cavity
c -----
77 8 -1.15e-3 +450 -362 -451 $ Reflector BP1
78 8 -1.15e-3 +462 -464 -453 $ Reflector BP3
79 8 -1.15e-3 -450 -362 +455
c -----
c BP1, BP2, BP3, BP4, BP5 cavity
c -----
81 8 -1.15e-3 +451 -362 -100 #95 VOL=1 $ Reflector BP1
82 8 -1.15e-3 (-430 +408) +350 -100 #96 VOL=1 $ Reflector BP2
83 8 -1.15e-3 +453 -464 -100 #97 VOL=1 $ Reflector BP3
84 8 -1.15e-3 (-440 +409) +350 -100 #98 VOL=1 $ Reflector BP4
85 8 -1.15e-3 -455 -362 -100 #99 VOL=1 $ Reflector BP5
c -----
95 8 -1.15e-3 -171
96 8 -1.15e-3 -172
97 8 -1.15e-3 -173
98 8 -1.15e-3 -174
99 8 -1.15e-3 -175
c -----
c Rotary specimen rack (RSR) unit
c -----
90 8 -1.15e-3 +300 -303 +352 -371 $ RSR unit
91 8 -1.15e-3 +300 +304 -352 -380 $ RSR unit
92 8 -1.15e-3 +300 -304 -380 +382 $ RSR unit
vol=1
c -----
c Fill universe for reactor core grid
c -----
c Graphite reflector elements, U=6
c -----
100 1 -1.0 #101 #102 #103
#104 #105 #106 u=6
101 2 -2.7 -623 -609 +206 u=6 $ lower fitting

```

```

102 2 -2.7 -605 -620 +621 u=6 $ end closure
103 4 -2.25 -605 -621 +622 u=6 $ graphite
104 2 -2.7 -605 -622 +623 u=6 $ end closure
105 2 -2.7 +620 -609 -201 u=6 $ upper fitting
106 2 -2.7 +605 -607 -620 +623 u=6 $ element clad
c
c -----
c Transient control rod, U=7
c -----
110 1 -1.0 #111 #112 #113 #114
      #115 #116 #117 u=7
111 2 -2.7 -500 -510 +511 u=7 $ end plug
112 2 -2.7 -500 -511 +512 u=7 $ spacer plug
113 6 -2.52 -500 -512 +513 u=7 $ absorber
114 2 -2.7 -500 -513 +514 u=7 $ spacer plug
115 8 -1.15e-3 -500 -514 +515 u=7 $ air follower
116 3 -7.8 -500 -515 +516 u=7 $ end plug
117 3 -7.8 +500 -502 -510 +516 u=7 $ element clad
c
c -----
c Standard triga fuel element, U=8
c -----
c Temperature in fuel rod assumed 600 K at full power
120 1 -1.0 #121 #122 #123
      #124 #125 #126
      #127 #128 #129 u=8 $ element clad
121 3 -7.8 -615 -603 +206 u=8 $ lower fitting
122 3 -7.8 -600 -610 +611 u=8 $ end closure
123 4 -2.25 -600 -611 +612 u=8 $ graphite
124 5 -6.05 -600 -612 +613 +650 u=8 TMP1=5.1702E-8 $ fuel at 600K
125 7 -6.49 -650 -612 +613 u=8 $ Zr rod
126 4 -2.25 -600 -613 +614 u=8 $ graphite
127 3 -7.8 -600 -614 +615 u=8 $ end closure
128 3 -7.8 +610 -603 -201 u=8 $ upper fitting
129 3 -7.8 +600 -602 -610 +615 u=8 $ element clad
c
c -----
c Fuel follower control rods (reg, shim1, shim2), U=9
c -----
c Temperature assumed 300 C at full power
130 1 -1.0 #131 #132 #133 #134 #135
      #136 #137 #138 #139 #140
      #141 #142 #143 u=9
131 3 -7.8 -505 -520 +521 u=9 $ end plug
132 8 -1.15e-3 -505 -521 +522 u=9 $ top space
133 2 -2.7 -505 -522 +523 u=9 $ spacer plug
134 8 -1.15e-3 -505 -523 +524 u=9 $ void gap
135 6 -2.52 -505 -524 +525 u=9 $ absorber
136 2 -2.7 -505 -525 +526 u=9 $ spacer plug
137 8 -1.15e-3 -505 -526 +527 u=9 $ void gap
138 5 -6.05 -505 -527 +528 +550 u=9 TMP1=5.1702E-8 $ fuel follower
139 7 -6.49 -550 -527 +528 u=9 $ Zr rod
140 2 -2.7 -505 -528 +529 u=9 $ spacer plug
141 8 -1.15e-3 -505 -529 +530 u=9 $ bot space
142 3 -7.8 -505 -530 +531 u=9 $ end plug
143 3 -7.8 +505 -507 -520 +531 u=9 $ element clad
c
c -----
c Modifications and experiment components
c -----
c Pneumatic transfer system (PTS) without Cd, U=30 - JDB - 4/13/2007
c -----
300 1 -1.0 #301 #302 #303
      #304 #305 #306
      #307 #308 U=30 $ Water surrounding PTS
301 2 -2.7 -910 +911 +933 U=30 $ Al transport tube
302 8 -1.15e-3 -911 +912 +933 U=30 $ Air gap
303 2 -2.7 -912 +913 +915 U=30 $ Al sample tube
304 8 -1.15e-3 -913 +915 #308 U=30 $ Sample location
305 2 -2.7 -910 +934 -933 U=30 $ Al transport tube bottom
306 2 -2.7 -912 +931 -915 U=30 $ Al sample tube bottom
307 8 -1.15e-3 +933 -931 -912 U=30 $ Air gap beneath sample tube
308 8 -1.15e-3 -908 +909 -907 U=30 $ Sample location for tally
c
c -----
c Pneumatic transfer system (PTS) with Cd, U=35 - JDB - 4/13/2007

```

```

c -----
350 1 -1.0 #351 #352 #353
      #354 #355 #356
      #357 #358 #359 #360 U=35 $ Water surrounding PTS
351 2 -2.7 -910 +911 +933 U=35 $ Al transport tube
352 8 -1.15e-3 -911 +914 +933 U=35 $ Air gap
353 10 -8.65 -914 +912 +931 U=35 $ Cd liner
354 2 -2.7 -912 +913 +915 U=35 $ Al sample tube
355 8 -1.15e-3 -913 +915 #360 U=35 $ Sample location
356 2 -2.7 -910 +934 -933 U=35 $ Al transport tube bottom
357 2 -2.7 -912 +931 -915 U=35 $ Al sample tube bottom
358 10 -8.65 -914 -931 +932 U=35 $ Cd liner beneath sample
359 8 -1.15e-3 +933 -932 -914 U=35 $ Air gap beneath sample tube
360 8 -1.15e-3 -908 +909 -907 U=35 $ Sample location for tally
c
c -----
c 3-element irradiator with Pb, U=40
c -----
400 1 -1.0 #401 #402 #403 #404
      #405 #406 #407 #408
      #409 #410 u=40 $ Water
401 2 -2.7 -920 +921 -958 +959 u=40 $ Al outer
402 8 -1.15e-3 -921 +924 -958 +959 u=40 $ Air gap
403 11 -11.4 -924 +922 -958 +959 u=40 $ Pb liner
404 2 -2.7 -922 +923 -958 +959 u=40 $ Al liner
405 8 -1.15e-3 -923 -963 +965 u=40 $ Air in sample location
406 8 -1.15e-3 -923 -958 +963 u=40 $ Air above sample location
407 2 -2.7 -962 -957 +958 u=40 $ Upper end cap
408 2 -2.7 -920 -959 +960 u=40 $ Lower end cap
409 2 -2.7 -923 -965 +966 u=40
410 11 -11.4 -923 -966 +959 u=40
c
c -----
c 3-element irradiator, U=45
c -----
450 1 -1.0 #451 #452 #453 #454 $ #461 #462 #463 #465
      #455 #456 #457 #458
      #459 #460 U=45 $ Water
451 2 -2.7 -920 +921 -958 +959 U=45 $ Al outer
452 2 -2.7 -922 +923 -958 +959 U=45 $ Al liner
453 11 -11.34 +922 -924 -958 +959 U=45 $ Pb liner
454 8 -1.15e-3 -921 +924 -958 +959 U=45 $ Air gap
455 8 -1.15e-3 -923 -958 +959 U=45 $ Air in sample location
      vol=1452
456 8 -1.15e-3 -923 -958 +963 u=45 $ Air above sample location
457 2 -2.7 -962 -957 +958 u=45 $ Upper end cap
458 2 -2.7 -920 -959 +960 u=45 $ Lower end cap
459 2 -2.7 -923 -965 +966 u=45
460 11 -8.65 -923 -966 +959 u=45 $ Changed to Pb
c
c 461 2 -2.7 +1956 -957 -1941 +1942 U=45 $ Al outer
c 462 11 -11.4 +1955 -958 -1942 +1943 U=45 $ Pb in sleeve
c 463 2 -2.7 +1956 -957 -1943 +1944 u=45 $ Al inner
c 464 2 -2.7 +958 -957 -1942 +1943 u=45 $ Al donut top (lid)
c 465 2 -2.7 +1956 -1955 -1942 +1943 u=45 $ Al donut bottom
c
c -----
c 3-element irradiator (unlined), U=50
c -----
490 8 -1.15e-3 #491 #492 #493 #494 U=50 $
491 2 -2.7 -922 +923 -950 +955 U=50 $ T3 can cylinder
492 2 -2.7 +922 -924 -950 +955 U=50 $ T3 can liner
493 2 -2.7 -923 +950 -951 U=50 $ T3 can upper
494 2 -2.7 -923 -955 +956 U=50 $ T3 can lower
c
c -----
c Water cells for mapping experiment, u=101
c -----
515 1 -1.0 #516 u=101
516 1 -1.0 -754 +782 -750 u=101
c
c -----
c 1-inch detector
c -----
1740 1 -1.0 #1741 #1742 U=81 $ element clad
1741 8 -1.15e-3 -638 -639 +640 #1742 U=81

```

```

1742 8 -1.15e-3 -638 -641 +642      U=81  $ flux tally for 1" dia FC
c -----
c Central thimble (CT), u=82 - JDB
c -----
1750 1 -1.0 #1751 #1752      u=82
1751 2 -2.7 -442 +443 +207  u=82
1752 1 -1.0 -446 +447 -445  u=82
c
c -----
c Photon Radial Profile Holes
c -----
1800 1 -1.0 -2000
1801 1 -1.0 -2001
1802 1 -1.0 -2002
1803 1 -1.0 -2003
1804 1 -1.0 -2004
1805 1 -1.0 -2005
1806 1 -1.0 -2006
c
c -----
c Outside world
c -----
2999 0      +100: +110: -120
c
c -----
c                      End of Cell Card Specification
c -----

c -----
c          Beginning of Surface Card Specification
c -----
c Hexagonal cell lattice surfaces
c -----
101  PX   +2.17678      $ Fuel lattice hex-prism
102  PX   -2.17678      $ Fuel lattice hex-prism
103  P  +1  1.73205  0  +4.35356 $ Fuel lattice hex-prism
104  P  +1  1.73205  0  -4.35356 $ Fuel lattice hex-prism
105  P  -1  1.73205  0  +4.35356 $ Fuel lattice hex-prism
106  P  -1  1.73205  0  -4.35356 $ Fuel lattice hex-prism
107  CZ   +2.51353      $ Maximum lattice diagonal radius
c
108  py   5.65531
109  py  -5.65531
c
c -----
c Axial and radial domain
c -----
100  CZ   +75
110  PZ  +100      $ Upper bound
120  PZ  -75      $ Lower bound
150  CZ   +5.08      $ Detector Cylinder
160  PZ  +10      $ Detector Lower
165  PZ  +30      $ Detector Upper
c
171  s   60.000 -36.000 -6.985 2.5  $ BP1
172  s   60.000 36.000 -6.985 2.5  $ BP2
173  s    0.000 70.000 -6.985 2.5  $ BP3
174  s  -60.000 36.000 -6.985 2.5  $ BP4
175  s  -60.000 -36.000 -6.985 2.5  $ BP5
c
c -----
c Reactor core grid plate surfaces
c -----
200  CZ   1.91135      $ Grid plate element holes
201  PZ  +32.3850      $ Upper grid plate region
202  PZ  +30.7975      $ Upper grid plate region
203  CZ   27.6225      $ Upper grid plate diameter - effective core diameter
205  CZ   1.5875      $ Grid plate coolant holes
206  PZ  -33.17875     $ Lower grid plate region
207  PZ  -36.35375     $ Lower grid plate region
211  PX  +26.1216      $ Lower grid plate edge
212  PX  -26.1216      $ Lower grid plate edge
213  P  +1  0.57735  0  +29.0240 $ Lower grid plate edge
214  P  +1  0.57735  0  -29.0240 $ Lower grid plate edge

```

215 P -1 0.57735 0 +29.0240 \$ Lower grid plate edge  
216 P -1 0.57735 0 -29.0240 \$ Lower grid plate edge  
221 PY +25.1360 \$ Lower grid plate edge  
222 PY -25.1360 \$ Lower grid plate edge  
223 P +1 1.73205 0 +52.2432 \$ Lower grid plate edge  
224 P +1 1.73205 0 -52.2432 \$ Lower grid plate edge  
225 P -1 1.73205 0 +52.2432 \$ Lower grid plate edge  
226 P -1 1.73205 0 -52.2432 \$ Lower grid plate edge  
231 PX +26.6700 \$ Core shroud inside surface  
232 PX -26.6700 \$ Core shroud inside surface  
233 P +1 0.57735 0 +29.2100 \$ Core shroud inside surface  
234 P +1 0.57735 0 -29.2100 \$ Core shroud inside surface  
235 P -1 0.57735 0 +29.2100 \$ Core shroud inside surface  
236 P -1 0.57735 0 -29.2100 \$ Core shroud inside surface  
241 PY +25.4000 \$ Core shroud inside surface  
242 PY -25.4000 \$ Core shroud inside surface  
243 P +1 1.73205 0 +54.9275 \$ Core shroud inside surface  
244 P +1 1.73205 0 -54.9275 \$ Core shroud inside surface  
245 P -1 1.73205 0 +54.9275 \$ Core shroud inside surface  
246 P -1 1.73205 0 -54.9275 \$ Core shroud inside surface  
c  
c -----  
c Core structure surfaces  
c -----  
c Reflector inner shroud  
c -----  
300 CZ 30.083125 \$ Grid plate alignment ring  
301 CZ 29.765625 \$ Grid plate alignment ring  
302 CZ 27.9400 \$ Grid plate alignment ring  
303 PZ +33.9725 \$ Grid plate alignment ring  
304 PZ +26.3525 \$ Grid plate alignment ring  
c  
c -----  
c Shroud load ring  
c -----  
305 CZ 27.9400 \$ Reflector shroud load ring \$ 24.7650  
306 PZ -37.30625 \$ Reflector shroud load ring  
307 PZ -39.52875 \$ Reflector shroud load ring  
c  
311 PX +29.2100 \$ Reflector shroud support  
312 PX -29.2100 \$ Reflector shroud support  
313 P +1 0.57735 0 +32.385 \$ Reflector shroud support  
314 P +1 0.57735 0 -32.385 \$ Reflector shroud support  
315 P -1 0.57735 0 +32.385 \$ Reflector shroud support  
316 P -1 0.57735 0 -32.385 \$ Reflector shroud support  
321 PY +27.9400 \$ Reflector shroud support  
322 PY -27.9400 \$ Reflector shroud support  
323 P +1 1.73205 0 +59.3725 \$ Reflector shroud support  
324 P +1 1.73205 0 -59.3725 \$ Reflector shroud support  
325 P -1 1.73205 0 +59.3725 \$ Reflector shroud support  
326 P -1 1.73205 0 -59.3725 \$ Reflector shroud support  
c  
331 PX +27.3050 \$ Core shroud plate exterior  
332 PX -27.3050 \$ Core shroud plate exterior  
333 P +1 0.57735 0 +29.8450 \$ Core shroud plate exterior  
334 P +1 0.57735 0 -29.8450 \$ Core shroud plate exterior  
335 P -1 0.57735 0 +29.8450 \$ Core shroud plate exterior  
336 P -1 0.57735 0 -29.8450 \$ Core shroud plate exterior  
341 PY +26.0350 \$ Core shroud plate exterior  
342 PY -26.0350 \$ Core shroud plate exterior  
343 P +1 1.73205 0 +56.5150 \$ Core shroud plate exterior  
344 P +1 1.73205 0 -56.5150 \$ Core shroud plate exterior  
345 P -1 1.73205 0 +56.5150 \$ Core shroud plate exterior  
346 P -1 1.73205 0 -56.5150 \$ Core shroud plate exterior  
c  
c -----  
c Reflector outer shroud  
c -----  
350 CZ +54.76875 \$ Reflector outer shroud  
351 CZ +53.49875 \$ Reflector outer shroud  
352 PZ +28.8925 \$ Outer shroud upper edge  
353 PZ -32.0675 \$ Outer shroud lower edge  
355 PY 0.0 \$ Core shroud section plane  
c  
c -----  
c Reflector beam ports

```

c -----
360 PY +55.5625 $ Radial penetrating beam port
361 C/X -35.2552 -6.985 7.62 $ Tangential thru beam port
362 C/X -35.2552 -6.985 6.9088 $ Tangential thru beam port
363 C/Y 0.0 -6.985 10.160 $ Radial penetrating beam port
364 C/Y 0.0 -6.985 9.525 $ Radial penetrating beam port
c
370 CZ 53.3400 $ Reflector top shroud
371 CZ 37.4650 $ Reflector top shroud
372 PZ +29.5275 $ Reflector top shroud
373 PZ +28.2575 $ Reflector top shroud
374 CZ 52.0700 $ Reflector inner shroud base
375 PZ -27.9400 $ Reflector inner shroud base
376 PZ -29.5275 $ Reflector inner shroud base
377 PZ -36.8300 $ Reflector shroud edge ring
c
c -----
c RSR experiment system
c -----
380 CZ +37.1475 $ RSR cavity outer ring
381 PZ +6.9850 $ RSR cavity base
382 PZ +7.3025 $ RSR cavity base
c
c -----
c Graphite reflector surfaces
c -----
400 CZ 53.0225 $ Graphite reflector outer radius
401 CZ 37.7825 $ Graphite reflector inner radius
402 PZ 27.6225 $ Graphite reflector upper section
403 PZ 6.3500 $ Graphite reflector section plane
404 PY -20.32 $ Graphite reflector section plane
405 PY -35.2552 $ Beam port penetration
406 2 CY 7.62 $ Tangential beam port, bp2
407 4 CY 7.62 $ Radial beam port, bp4
408 2 PY 0.0 $ Tangential beam port, bp2
409 4 PY 0.0 $ Radial beam port, bp4
411 PX +27.78125 $ Graphite inner surface
412 PX -27.78125 $ Graphite inner surface
413 P +1 0.57735 0 +31.00875 $ Graphite inner surface +1
414 P +1 0.57735 0 -31.00875 $ Graphite inner surface +1
415 P -1 0.57735 0 +31.00875 $ Graphite inner surface +1
416 P -1 0.57735 0 -31.00875 $ Graphite inner surface +1
421 PY +26.431875 $ Graphite inner surface
422 PY -26.431875 $ Graphite inner surface
423 P +1 1.73205 0 +57.30875 $ Graphite inner surface +1
424 P +1 1.73205 0 -57.30875 $ Graphite inner surface +1
425 P -1 1.73205 0 +57.30875 $ Graphite inner surface +1
426 P -1 1.73205 0 -57.30875 $ Graphite inner surface +1
c
430 2 CY 6.9088 $ Tangential beam port, bp2
440 4 CY 6.9088 $ Radial beam port, bp4
450 PX 0.0 $ BP1&5 origin
c
c -----
c Central thimble
c -----
442 CZ 1.50 $ Central thimble guide rod OD
443 CZ 1.415 $ Central thimble guid rod ID
444 CZ 1.25 $ Central thimble sample holder OD
445 CZ 1.185 $ Central thimble sample holder ID
446 PZ 2.5 $ Central thimble upper sample holder
447 PZ -2.5 $ Central thimble lower sample holder
c beam port tally surfaces bp1&5 and bp3
451 PX +10.16 $ BP1
453 PY +40.90 $ BP3
455 PX -10.16 $ BP5
c pool structure pipe, bp3
461 PY +25.600 $ Radial penetrating beam port, bp3
462 PY +26.235 $ Radial penetrating beam port, bp3
463 C/Y 0.0 -6.985 7.62 $ Radial penetrating beam port, bp3
464 C/Y 0.0 -6.985 6.9088 $ Radial penetrating beam port, bp3
c
c -----
c Control element surfaces
c -----
500 CZ 1.5113 $ Control element - absorber surface, radius

```

502	CZ	1.5875	\$ Control element - clad outer surface
505	CZ	1.6637	\$ Control element - absorber surface, radius
507	CZ	1.7145	\$ Control element - clad outer surface
c			
510	7 PZ	+24.765	\$ Control element - element plug, end
511	7 PZ	+24.13	\$ Control element - magneform plug, upper
512	7 PZ	+19.05	\$ Control element - absorber surface,length/2
513	7 PZ	-19.05	\$ Control element - absorber surface,length/2
514	7 PZ	-21.59	\$ Control element - magneform plug, lower
515	7 PZ	-70.8025	\$ Control element - air follower section
516	7 PZ	-72.7075	\$ Control element - element plug, end
c			
517	pz	+75	
518	pz	-75	
519	cz	1.5875	
532	cz	1.7145	
c			
520	7 PZ	+34.925	\$ Control element - element plug, end
521	7 PZ	+31.115	\$ Control element - void gap
522	7 PZ	+20.6375	\$ Control element - magneform plug, upper
523	7 PZ	+19.3675	\$ Control element - void gap
524	7 PZ	+19.05	\$ Control element - absorber surface,length/2
525	7 PZ	-19.05	\$ Control element - absorber surface,length/2
526	7 PZ	-20.32	\$ Control element - magneform plug, lower
527	7 PZ	-20.955	\$ Control element - void gap
528	7 PZ	-59.055	\$ Control element - fuel follower section
529	7 PZ	-61.595	\$ Control element - void gap
530	7 PZ	-74.93	\$ Control element - magneform plug, bottom
531	7 PZ	-74.99	\$ Control element - element plug, end
c			
550	CZ	0.28575	\$ Zirconium rod
c			
c -----			
c Fuel and moderator element surfaces			
c -----			
600	CZ	1.816	\$ Fuel element - fuel region surface, radius
602	CZ	1.867	\$ Fuel element - clad outer surface
603	CZ	1.5306	\$ Fuel - adapter effective radius, lower
604	CZ	1.9426	\$ Fuel - adapter effective radius, upper
605	CZ	1.816	\$ Graphite element - element surface, radius
606	CZ	1.867	\$ Graphite element - clad outer surface
607	CZ	1.867	\$ Graphite element - clad outer surface
608	CZ	1.9426	\$ Graphite - adapter effective radius, upper
609	CZ	1.5306	\$ Graphite - adapter effective radius, lower
c			
610	PZ	+28.5877	\$ Fuel element - element end region, upper
611	PZ	+27.7368	\$ Fuel element - graphite end region, upper
612	PZ	+19.05	\$ Fuel element - fuel surface, length/2
613	PZ	-19.05	\$ Fuel element - fuel surface, length/2
614	PZ	-27.7368	\$ Fuel element - graphite end region, lower
615	PZ	-28.5877	\$ Fuel element - element end region, lower
c			
620	PZ	+28.5877	\$ Graphite element - element end, upper
621	PZ	+27.7368	\$ Graphite element - graphite end, upper
622	PZ	-27.7368	\$ Graphite element - graphite end, lower
623	PZ	-28.5877	\$ Graphite element - element end, lower
c			
635	PZ	15.24	\$ Flux Tally
636	PZ	-15.24	\$ Flux Tally
637	CZ	0.4	\$ Flux Tally hole for the KSU detector
638	CZ	1.27	
639	PZ	7.7851	
640	PZ	-7.7851	
641	PZ	6.35	
642	PZ	-6.35	
c			
650	CZ	0.28575	\$ Zirconium rod
c			
660	CZ	1.5306	\$ Element adapter effective radius
661	CZ	1.867	\$ Element clad outer surface
662	PZ	+32.3850	\$ Upper grid plate, top
663	PZ	+28.5877	\$ Element end region, upper
664	PZ	-28.5877	\$ Element end region, lower
665	PZ	-33.17875	\$ Lower grid plate, top
666	cz	1.91135	\$ Upper grid plate holes
c			

```

c -----
c Boundaries for large irradiator
c -----
701 PX +8.70712
703 PX +10.8839
708 PX +19.59102
710 PX 21.7678
712 PX 19.59102
717 PX 10.8839
702 P -1 1.73205 0 -26.12136
704 P -1 1.73205 0 -21.7678
705 P 1 1.73205 0 4.35356
706 P -1 1.73205 0 -26.12136
707 P 1 1.73205 0 8.70712
709 P 1 1.73205 0 4.35356
711 P -1 1.73205 0 -43.5356
713 P -1 1.73205 0 -47.88916
714 P 1 1.73205 0 -13.06068
715 P -1 1.73205 0 -43.5356
716 P 1 1.73205 0 -17.41424
718 P 1 1.73205 0 -13.06068
c
c -----
c Reactor core modifications
c -----
c Center tube irradiations
c -----
900 CZ 1.905 $ Center tube outer radius
901 CZ 1.69418 $ Center tube inner radius
905 CZ 1.5 $ Sample radius
907 PZ +0.5 $ Sample length
908 CZ 0.5 $ Sample radius (PTS)
909 PZ -0.5 $ Sample length
c
c -----
c PNT tube dimensions
c -----
910 CZ +1.74625 $ Al transport tube outer radius
911 CZ +1.53543 $ Al transport tube inner radius
912 CZ +1.11125 $ Al sample tube outer radius
913 CZ +0.86995 $ Al sample tube inner radius
914 CZ +1.16205 $ Cd two layer liner
915 PZ -2.07645 $ PTS sample stop
916 PZ -18.89125 $ Cd absorber end
917 PZ -21.1264591 $ Cd absorber disk, upper edge
918 PZ -21.17725 $ Cd absorber disk, lower edge
919 PZ -30.32125 $ PTS bottom section
931 PZ -2.94775 $ Al sample tube bottom
932 PZ -2.99855 $ Bottom of Cd liner
933 PZ -3.37193 $ Top of Al transport tube
934 PZ -3.58275 $ Bottom of Al transport tube
c
c -----
c 3-element irradiator with Cd or Pb
c -----
c Reference to lower grid plate -33.17875
920 c/z 0 0 +2.38125 $ Al can outer radius
921 c/z 0 0 +2.23393 $ Al can inner radius
922 c/z 0 0 +2.06375 $ Al sleeve outer radius
923 c/z 0 0 +1.93929 $ Al sleeve inner radius
924 c/z 0 0 +2.16535 $ Cd liner outer radius
c 930 c/z 0 -0 +0.47625 $ Al structure rod
c 940 PZ -30.xxxx $ Al bearing section
950 PZ +2.54 $ Al upper end cap
951 PZ +2.5908 $ Al upper end cap
955 PZ -2.54 $ Al lower end cap
956 PZ -2.5908 $ Al lower end cap
c
957 pz +99.82125 $ Al upper end cap, top
958 pz +96.82125 $ Al upper end cap, bottom
963 pz +30.7975 $ Bottom of upper grid plate
959 pz -26.19375 $ Al lower end cap, top
960 pz -31.27385 $ Al lower end cap, bottom
962 c/z -15.23746 -8.79856 +3.00000
c
961 c/z -15.23746 -8.79856 +3.0099

```

```

c
965 pz -25.55875    $ Top of Al in Al sleeve
966 pz -26.09215    $ Top of Cd liner in sleeve
967 pz -26.19375    $ Top of lower end cap
c
c -----
c Large irradiator surfaces with cadmium sleeve
c -----
c 1940 c/z 15.23746 -11.31062 5.27939 $ Center of irradiator
c 1940 c/z +10.8839 +8.79856 2.4    $ Center of 3L irradiator
1940 c/z -15.24 -8.80 +2.4    $ Center of 3L irradiator
c
1941 cz 5.08
1942 cz 4.7625
1943 cz 3.81
1944 cz 3.4925
1945 cz 3.175
1946 cz 2.8575
1947 cz 2.0000
c
1950 pz +32.3850    $ Al upper end cap
1951 pz +32.22625    $ Al upper end cap
1955 pz -33.02    $ Al lower end cap
1956 pz -33.17875    $ Al lower end cap
c
c -----
c Surfaces for flux mapping with Ni wire - JDB
c -----
1963 c/z 2.17678 -1.2573 +0.16 $ A
1964 c/z 15.23746 -1.2573 +0.16 $ K
1965 c/z 19.59102 -1.2573 +0.16 $ L
1966 c/z 23.94458 -1.2573 +0.16 $ M
c
750 cz 0.15875
751 cz 0.16
754 pz 32.385
782 pz -36.35375
c
c -----
c Photon Radial Profile Holes
c -----
2000 s +0.0 +2.51353 +0.0 0.3175
2001 s +0.0 +5.020706 +0.0 0.3175
2002 s +0.0 +10.05412 +0.0 0.3175
2003 s +0.0 +12.56765 +0.0 0.3175
2004 s +0.0 +17.59470 +0.0 0.3175
2005 s +0.0 +20.10823 +0.0 0.3175
2006 s +0.0 +25.0 +0.0 0.3175
c
c -----
c Upper grid plate holes
c -----
5000 c/z +0.00000 +0.00000 +1.91135 $ Upper grid plate hole, A1
5001 c/z +4.35356 +0.00000 +1.91135 $ Upper grid plate hole, B1
5002 c/z +2.17678 -3.76936 +1.91135 $ Upper grid plate hole, B2
5003 c/z -2.17678 -3.76936 +1.91135 $ Upper grid plate hole, B3
5004 c/z -4.35356 +0.00000 +1.91135 $ Upper grid plate hole, B4
5005 c/z -2.17678 +3.76936 +1.91135 $ Upper grid plate hole, B5
5006 c/z +2.17678 +3.76936 +1.91135 $ Upper grid plate hole, B6
5007 c/z +8.70712 +0.00000 +1.91135 $ Upper grid plate hole, C1
5008 c/z +6.53034 -3.76936 +1.91135 $ Upper grid plate hole, C2
5009 c/z +4.35356 -7.54126 +1.91135 $ Upper grid plate hole, C3
5010 c/z -0.00000 -7.54126 +1.91135 $ Upper grid plate hole, C4
5011 c/z -4.35356 -7.54126 +1.91135 $ Upper grid plate hole, C5
5012 c/z -6.53034 -3.76936 +1.91135 $ Upper grid plate hole, C6
5013 c/z -8.70712 +0.00000 +1.91135 $ Upper grid plate hole, C7
5014 c/z -6.53034 +3.76936 +1.91135 $ Upper grid plate hole, C8
5015 c/z -4.35356 +7.54126 +1.91135 $ Upper grid plate hole, C9
5016 c/z -0.00000 +7.54126 +1.91135 $ Upper grid plate hole, C10
5017 c/z +4.35356 +7.54126 +1.91135 $ Upper grid plate hole, C11
5018 c/z +6.53034 +3.76936 +1.91135 $ Upper grid plate hole, C12
5019 c/z +13.06068 +0.00000 +1.91135 $ Upper grid plate hole, D1
5020 c/z +10.88390 -3.76936 +1.91135 $ Upper grid plate hole, D2
5021 c/z +8.70712 -7.54126 +1.91135 $ Upper grid plate hole, D3
5022 c/z +6.53034 -11.31062 +1.91135 $ Upper grid plate hole, D4

```

5023 c/z +2.17678 -11.31062 +1.91135 \$ Upper grid plate hole, D5  
5024 c/z -2.17678 -11.31062 +1.91135 \$ Upper grid plate hole, D6  
5025 c/z -6.53034 -11.31062 +1.91135 \$ Upper grid plate hole, D7  
5026 c/z -8.70712 -7.54126 +1.91135 \$ Upper grid plate hole, D8  
5027 c/z -10.88390 -3.76936 +1.91135 \$ Upper grid plate hole, D9  
5028 c/z -13.06068 +0.00000 +1.91135 \$ Upper grid plate hole, D10  
5029 c/z -10.88390 +3.76936 +1.91135 \$ Upper grid plate hole, D11  
5030 c/z -8.70712 +7.54126 +1.91135 \$ Upper grid plate hole, D12  
5031 c/z -6.53034 +11.31062 +1.91135 \$ Upper grid plate hole, D13  
5032 c/z -2.17678 +11.31062 +1.91135 \$ Upper grid plate hole, D14  
5033 c/z +2.17678 +11.31062 +1.91135 \$ Upper grid plate hole, D15  
5034 c/z +6.53034 +11.31062 +1.91135 \$ Upper grid plate hole, D16  
5035 c/z +8.70712 +7.54126 +1.91135 \$ Upper grid plate hole, D17  
5036 c/z +10.88390 +3.76936 +1.91135 \$ Upper grid plate hole, D18  
5037 c/z +17.41424 +0.00000 +1.91135 \$ Upper grid plate hole, E1  
5038 c/z +15.23746 -3.76936 +1.91135 \$ Upper grid plate hole, E2  
5039 c/z +13.06068 -7.54126 +1.91135 \$ Upper grid plate hole, E3  
5040 c/z +10.88390 -11.31062 +1.91135 \$ Upper grid plate hole, E4  
5041 c/z +8.70712 -15.08252 +1.91135 \$ Upper grid plate hole, E5  
5042 c/z +4.35356 -15.08252 +1.91135 \$ Upper grid plate hole, E6  
5043 c/z -0.00000 -15.08252 +1.91135 \$ Upper grid plate hole, E7  
5044 c/z -4.35356 -15.08252 +1.91135 \$ Upper grid plate hole, E8  
5045 c/z -8.70712 -15.08252 +1.91135 \$ Upper grid plate hole, E9  
5046 c/z -10.88390 -11.31062 +1.91135 \$ Upper grid plate hole, E10  
5047 c/z -13.06068 -7.54126 +1.91135 \$ Upper grid plate hole, E11  
5048 c/z -15.23746 -3.76936 +1.91135 \$ Upper grid plate hole, E12  
5049 c/z -17.41424 +0.00000 +1.91135 \$ Upper grid plate hole, E13  
5050 c/z -15.23746 +3.76936 +1.91135 \$ Upper grid plate hole, E14  
5051 c/z -13.06068 +7.54126 +1.91135 \$ Upper grid plate hole, E15  
5052 c/z -10.88390 +11.31062 +1.91135 \$ Upper grid plate hole, E16  
5053 c/z -8.70712 +15.08252 +1.91135 \$ Upper grid plate hole, E17  
5054 c/z -4.35356 +15.08252 +1.91135 \$ Upper grid plate hole, E18  
5055 c/z -0.00000 +15.08252 +1.91135 \$ Upper grid plate hole, E19  
5056 c/z +4.35356 +15.08252 +1.91135 \$ Upper grid plate hole, E20  
5057 c/z +8.70712 +15.08252 +1.91135 \$ Upper grid plate hole, E21  
5058 c/z +10.88390 +11.31062 +1.91135 \$ Upper grid plate hole, E22  
5059 c/z +13.06068 +7.54126 +1.91135 \$ Upper grid plate hole, E23  
5060 c/z +15.23746 +3.76936 +1.91135 \$ Upper grid plate hole, E24  
5061 c/z +21.76780 +0.00000 +1.91135 \$ Upper grid plate hole, F1  
5062 c/z +19.59102 -3.76936 +1.91135 \$ Upper grid plate hole, F2  
5063 c/z +17.41424 -7.54126 +1.91135 \$ Upper grid plate hole, F3  
5064 c/z +15.23746 -11.31062 +1.91135 \$ Upper grid plate hole, F4  
5065 c/z +13.06068 -15.08252 +1.91135 \$ Upper grid plate hole, F5  
5066 c/z +10.88390 -18.85188 +1.91135 \$ Upper grid plate hole, F6  
5067 c/z +6.53034 -18.85188 +1.91135 \$ Upper grid plate hole, F7  
5068 c/z +2.17678 -18.85188 +1.91135 \$ Upper grid plate hole, F8  
5069 c/z -2.17678 -18.85188 +1.91135 \$ Upper grid plate hole, F9  
5070 c/z -6.53034 -18.85188 +1.91135 \$ Upper grid plate hole, F10  
5071 c/z -10.88390 -18.85188 +1.91135 \$ Upper grid plate hole, F11  
5072 c/z -13.06068 -15.08252 +1.91135 \$ Upper grid plate hole, F12  
5073 c/z -15.23746 -11.31062 +1.91135 \$ Upper grid plate hole, F13  
5074 c/z -17.41424 -7.54126 +1.91135 \$ Upper grid plate hole, F14  
5075 c/z -19.59102 -3.76936 +1.91135 \$ Upper grid plate hole, F15  
5076 c/z -21.76780 +0.00000 +1.91135 \$ Upper grid plate hole, F16  
5077 c/z -19.59102 +3.76936 +1.91135 \$ Upper grid plate hole, F17  
5078 c/z -17.41424 +7.54126 +1.91135 \$ Upper grid plate hole, F18  
5079 c/z -15.23746 +11.31062 +1.91135 \$ Upper grid plate hole, F19  
5080 c/z -13.06068 +15.08252 +1.91135 \$ Upper grid plate hole, F20  
5081 c/z -10.88390 +18.85188 +1.91135 \$ Upper grid plate hole, F21  
5082 c/z -6.53034 +18.85188 +1.91135 \$ Upper grid plate hole, F22  
5083 c/z -2.17678 +18.85188 +1.91135 \$ Upper grid plate hole, F23  
5084 c/z +2.17678 +18.85188 +1.91135 \$ Upper grid plate hole, F24  
5085 c/z +6.53034 +18.85188 +1.91135 \$ Upper grid plate hole, F25  
5086 c/z +10.88390 +18.85188 +1.91135 \$ Upper grid plate hole, F26  
5087 c/z +13.06068 +15.08252 +1.91135 \$ Upper grid plate hole, F27  
5088 c/z +15.23746 +11.31062 +1.91135 \$ Upper grid plate hole, F28  
5089 c/z +17.41424 +7.54126 +1.91135 \$ Upper grid plate hole, F29  
5090 c/z +19.59102 +3.76936 +1.91135 \$ Upper grid plate hole, F30  
5091 c/z +23.94458 -3.76936 +1.91135 \$ Upper grid plate hole, G2  
5092 c/z +21.76780 -7.54126 +1.91135 \$ Upper grid plate hole, G3  
5093 c/z +19.59102 -11.31062 +1.91135 \$ Upper grid plate hole, G4  
5094 c/z +17.41424 -15.08252 +1.91135 \$ Upper grid plate hole, G5  
5095 c/z +15.23746 -18.85188 +1.91135 \$ Upper grid plate hole, G6  
5096 c/z +8.70712 -22.62124 +1.91135 \$ Upper grid plate hole, G8  
5097 c/z +4.35356 -22.62124 +1.91135 \$ Upper grid plate hole, G9  
5098 c/z -0.00000 -22.62124 +1.91135 \$ Upper grid plate hole, G10

5099 c/z -4.35356 -22.62124 +1.91135 \$ Upper grid plate hole, G11  
 5100 c/z -8.70712 -22.62124 +1.91135 \$ Upper grid plate hole, G12  
 5101 c/z -15.23746 -18.85188 +1.91135 \$ Upper grid plate hole, G14  
 5102 c/z -17.41424 -15.08252 +1.91135 \$ Upper grid plate hole, G15  
 5103 c/z -19.59102 -11.31062 +1.91135 \$ Upper grid plate hole, G16  
 5104 c/z -21.76780 -7.54126 +1.91135 \$ Upper grid plate hole, G17  
 5105 c/z -23.94458 -3.76936 +1.91135 \$ Upper grid plate hole, G18  
 5106 c/z -23.94458 +3.76936 +1.91135 \$ Upper grid plate hole, G20  
 5107 c/z -21.76780 +7.54126 +1.91135 \$ Upper grid plate hole, G21  
 5108 c/z -19.59102 +11.31062 +1.91135 \$ Upper grid plate hole, G22  
 5109 c/z -17.41424 +15.08252 +1.91135 \$ Upper grid plate hole, G23  
 5110 c/z -15.23746 +18.85188 +1.91135 \$ Upper grid plate hole, G24  
 5111 c/z -8.70712 +22.62124 +1.91135 \$ Upper grid plate hole, G26  
 5112 c/z -4.35356 +22.62124 +1.91135 \$ Upper grid plate hole, G27  
 5113 c/z +4.35356 +22.62124 +1.91135 \$ Upper grid plate hole, G29  
 5114 c/z -0.00000 +22.62124 +1.91135 \$ Upper grid plate hole, G28  
 5115 c/z +8.70712 +22.62124 +1.91135 \$ Upper grid plate hole, G30  
 5116 c/z +15.23746 +18.85188 +1.91135 \$ Upper grid plate hole, G32  
 5117 c/z +17.41424 +15.08252 +1.91135 \$ Upper grid plate hole, G33  
 5118 c/z +19.59102 +11.31062 +1.91135 \$ Upper grid plate hole, G34  
 5119 c/z +21.76780 +7.54126 +1.91135 \$ Upper grid plate hole, G35  
 5120 c/z +23.94458 +3.76936 +1.91135 \$ Upper grid plate hole, G36

c  
 c -----  
 c Cut planes for tallies

c -----  
 6000 pz +32  
 6001 pz +31  
 6002 pz +30  
 6003 pz +29  
 6004 pz +28  
 6005 pz +27  
 6006 pz +26  
 6007 pz +25  
 6008 pz +24  
 6009 pz +23  
 6010 pz +22  
 6011 pz +21  
 6012 pz +20  
 6013 pz +19  
 6014 pz +18  
 6015 pz +17  
 6016 pz +16  
 6017 pz +15  
 6018 pz +14  
 6019 pz +13  
 6020 pz +12  
 6021 pz +11  
 6022 pz +10  
 6023 pz +9  
 6024 pz +8  
 6025 pz +7  
 6026 pz +6  
 6027 pz +5  
 6028 pz +4  
 6029 pz +3  
 6030 pz +2  
 6031 pz +1  
 6032 pz +0  
 6033 pz -1  
 6034 pz -2  
 6035 pz -3  
 6036 pz -4  
 6037 pz -5  
 6038 pz -6  
 6039 pz -7  
 6040 pz -8  
 6041 pz -9  
 6042 pz -10  
 6043 pz -11  
 6044 pz -12  
 6045 pz -13  
 6046 pz -14  
 6047 pz -15  
 6048 pz -16  
 6049 pz -17

6050 pz -18  
6051 pz -19  
6052 pz -20  
6053 pz -21  
6054 pz -22  
6055 pz -23  
6056 pz -24  
6057 pz -25  
6058 pz -26  
6059 pz -27  
6060 pz -28  
6061 pz -29  
6062 pz -30  
6063 pz -31  
6064 pz -32  
6065 pz -33  
6066 pz -34  
6067 pz -35  
6068 pz -36  
c  
7000 pz +30.861  
7001 pz +27.305  
7002 pz +25.781  
7003 pz +22.225  
7004 pz +20.701  
7005 pz +17.145  
7006 pz +15.621  
7007 pz +12.065  
7008 pz +10.541  
7009 pz +6.985  
7010 pz +5.461  
7011 pz +1.905  
7012 pz +0.381  
7013 pz -3.175  
7014 pz -4.699  
7015 pz -8.255  
7016 pz -9.779  
7017 pz -13.335  
7018 pz -14.859  
7019 pz -18.415  
7020 pz -19.939  
7021 pz -23.495  
7022 pz -25.019  
7023 pz -28.575  
7024 pz -30.099  
7025 pz -33.655  
7026 pz -35.179  
c  
8000 pz +30.7975       \$ Bottom of upper grid plate region  
8001 pz +27.7368       \$ Top of graphite region  
8002 pz +19.05         \$ Top of fuel region  
8003 pz -19.05         \$ Bottom of fuel region  
8004 pz -27.7368       \$ Bottom of graphite region  
8005 pz -33.17875       \$ Top of lower grid plate region  
c  
c -----  
c       End of Surface Card Specification  
c -----  
  
c -----  
c       Beginning of Material Card Specification  
c -----  
c -----  
c Beam tube transformations  
c -----  
c tr1: Through port, small, BP1  
c tr2: Tangential port, small, BP2  
c tr3: Radial port, large, BP3  
c tr4: Radial port, small, BP4  
c tr5: Through port, large, BP5  
c  
\*tr1 0.0 -35.255 -6.985 00 90 90 90 00 90  
\*tr2 +35.255 -06.222 -6.985 30 120 90 60 30 90  
\*tr3 0.0 +25.600 -6.985 00 90 90 90 00 90  
\*tr4 -22.871 +13.216 -6.985 60 30 90 150 60 90  
\*tr5 0.0 -35.255 -6.985 00 90 90 90 00 90

```

c
c the '*' just makes the transformation in degrees
c
c -----
c Control rod transformations
c -----
c Shutdown condition - 000 units
c Low power critical - 525 units
c Design high power - 700 units
c Full out condition - 960 units
c
tr6 0 0 00.00 1 0 0 0 1 0
tr7 0 0 15.00 1 0 0 0 1 0      $ Formerly 19.05, 8.33, 12.37
tr8 0 0 27.78 1 0 0 0 1 0
tr9 0 0 38.10 1 0 0 0 1 0
c
c -----
c Mapping experiment transformations
c -----
tr10 +2.17678 -1.2573 0.0
tr11 +15.23746 -1.2573 0.0
tr12 +19.59102 -1.2573 0.0
tr13 +23.94458 -1.2573 0.0
c
c -----
c Irradiation facility transformations
c -----
tr20 -15.23746 -8.79856 0.0      $ Center of 3L irradiator
c tr50 +15.23746 -11.31062 0.0    $ Center of 6L irradiator
c tr50 +10.8839 +8.79856 0.0     $ Center of 3L irradiator
tr50 -15.24 -8.80 0.0           $ Center of 3L irradiator
c
c -----
c Grid plate hole transformations
c -----
tr100 -0.00000 +0.00000 0.0 $ A1
tr101 +4.35356 +0.00000 0.0 $ B1
tr102 +2.17678 -3.76936 0.0 $ B2
tr103 -2.17678 -3.76936 0.0 $ B3
tr104 -4.35356 +0.00000 0.0 $ B4
tr105 -2.17678 +3.76936 0.0 $ B5
tr106 +2.17678 +3.76936 0.0 $ B6
tr107 +8.70712 +0.00000 0.0 $ C1
tr108 +6.53034 -3.76936 0.0 $ C2
tr109 +4.35356 -7.54126 0.0 $ C3
tr110 -0.00000 -7.54126 0.0 $ C4
tr111 -4.35356 -7.54126 0.0 $ C5
tr112 -6.53034 -3.76936 0.0 $ C6
tr113 -8.70712 +0.00000 0.0 $ C7
tr114 -6.53034 +3.76936 0.0 $ C8
tr115 -4.35356 +7.54126 0.0 $ C9
tr116 -0.00000 +7.54126 0.0 $ C10
tr117 +4.35356 +7.54126 0.0 $ C11
tr118 +6.53034 +3.76936 0.0 $ C12
tr119 +13.06068 +0.00000 0.0 $ D1
tr120 +10.88390 -3.76936 0.0 $ D2
tr121 +8.70712 -7.54126 0.0 $ D3
tr122 +6.53034 -11.31062 0.0 $ D4
tr123 +2.17678 -11.31062 0.0 $ D5
tr124 -2.17678 -11.31062 0.0 $ D6
tr125 -6.53034 -11.31062 0.0 $ D7
tr126 -8.70712 -7.54126 0.0 $ D8
tr127 -10.88390 -3.76936 0.0 $ D9
tr128 -13.06068 +0.00000 0.0 $ D10
tr129 -10.88390 +3.76936 0.0 $ D11
tr130 -8.70712 +7.54126 0.0 $ D12
tr131 -6.53034 +11.31062 0.0 $ D13
tr132 -2.17678 +11.31062 0.0 $ D14
tr133 +2.17678 +11.31062 0.0 $ D15
tr134 +6.53034 +11.31062 0.0 $ D16
tr135 +8.70712 +7.54126 0.0 $ D17
tr136 +10.88390 +3.76936 0.0 $ D18
tr137 +17.41424 +0.00000 0.0 $ E1
tr138 +15.23746 -3.76936 0.0 $ E2
tr139 +13.06068 -7.54126 0.0 $ E3
tr140 +10.88390 -11.31062 0.0 $ E4

```

tr141	+8.70712	-15.08252	0.0	\$ E5
tr142	+4.35356	-15.08252	0.0	\$ E6
tr143	-0.00000	-15.08252	0.0	\$ E7
tr144	-4.35356	-15.08252	0.0	\$ E8
tr145	-8.70712	-15.08252	0.0	\$ E9
tr146	-10.88390	-11.31062	0.0	\$ E10
tr147	-13.06068	-7.54126	0.0	\$ E11
tr148	-15.23746	-3.76936	0.0	\$ E12
tr149	-17.41424	+0.00000	0.0	\$ E13
tr150	-15.23746	+3.76936	0.0	\$ E14
tr151	-13.06068	+7.54126	0.0	\$ E15
tr152	-10.88390	+11.31062	0.0	\$ E16
tr153	-8.70712	+15.08252	0.0	\$ E17
tr154	-4.35356	+15.08252	0.0	\$ E18
tr155	-0.00000	+15.08252	0.0	\$ E19
tr156	+4.35356	+15.08252	0.0	\$ E20
tr157	+8.70712	+15.08252	0.0	\$ E21
tr158	+10.88390	+11.31062	0.0	\$ E22
tr159	+13.06068	+7.54126	0.0	\$ E23
tr160	+15.23746	+3.76936	0.0	\$ E24
tr161	+21.76780	+0.00000	0.0	\$ F1
tr162	+19.59102	-3.76936	0.0	\$ F2
tr163	+17.41424	-7.54126	0.0	\$ F3
tr164	+15.23746	-11.31062	0.0	\$ F4
tr165	+13.06068	-15.08252	0.0	\$ F5
tr166	+10.88390	-18.85188	0.0	\$ F6
tr167	+6.53034	-18.85188	0.0	\$ F7
tr168	+2.17678	-18.85188	0.0	\$ F8
tr169	-2.17678	-18.85188	0.0	\$ F9
tr170	-6.53034	-18.85188	0.0	\$ F10
tr171	-10.88390	-18.85188	0.0	\$ F11
tr172	-13.06068	-15.08252	0.0	\$ F12
tr173	-15.23746	-11.31062	0.0	\$ F13
tr174	-17.41424	-7.54126	0.0	\$ F14
tr175	-19.59102	-3.76936	0.0	\$ F15
tr176	-21.76780	+0.00000	0.0	\$ F16
tr177	-19.59102	+3.76936	0.0	\$ F17
tr178	-17.41424	+7.54126	0.0	\$ F18
tr179	-15.23746	+11.31062	0.0	\$ F19
tr180	-13.06068	+15.08252	0.0	\$ F20
tr181	-10.88390	+18.85188	0.0	\$ F21
tr182	-6.53034	+18.85188	0.0	\$ F22
tr183	-2.17678	+18.85188	0.0	\$ F23
tr184	+2.17678	+18.85188	0.0	\$ F24
tr185	+6.53034	+18.85188	0.0	\$ F25
tr186	+10.88390	+18.85188	0.0	\$ F26
tr187	+13.06068	+15.08252	0.0	\$ F27
tr188	+15.23746	+11.31062	0.0	\$ F28
tr189	+17.41424	+7.54126	0.0	\$ F29
tr190	+19.59102	+3.76936	0.0	\$ F30
tr191	+23.94458	-3.76936	0.0	\$ G2
tr192	+21.76780	-7.54126	0.0	\$ G3
tr193	+19.59102	-11.31062	0.0	\$ G4
tr194	+17.41424	-15.08252	0.0	\$ G5
tr195	+15.23746	-18.85188	0.0	\$ G6
tr196	+8.70712	-22.62124	0.0	\$ G8
tr197	+4.35356	-22.62124	0.0	\$ G9
tr198	-0.00000	-22.62124	0.0	\$ G10
tr199	-4.35356	-22.62124	0.0	\$ G11
tr200	-8.70712	-22.62124	0.0	\$ G12
tr201	-15.23746	-18.85188	0.0	\$ G14
tr202	-17.41424	-15.08252	0.0	\$ G15
tr203	-19.59102	-11.31062	0.0	\$ G16
tr204	-21.76780	-7.54126	0.0	\$ G17
tr205	-23.94458	-3.76936	0.0	\$ G18
tr206	-23.94458	+3.76936	0.0	\$ G20
tr207	-21.76780	+7.54126	0.0	\$ G21
tr208	-19.59102	+11.31062	0.0	\$ G22
tr209	-17.41424	+15.08252	0.0	\$ G23
tr210	-15.23746	+18.85188	0.0	\$ G24
tr211	-8.70712	+22.62124	0.0	\$ G26
tr212	-4.35356	+22.62124	0.0	\$ G27
tr213	+4.35356	+22.62124	0.0	\$ G29
tr214	-0.00000	+22.62124	0.0	\$ G28
tr215	+8.70712	+22.62124	0.0	\$ G30
tr216	+15.23746	+18.85188	0.0	\$ G32

```

tr217 +17.41424 +15.08252 0.0 $ G33
tr218 +19.59102 +11.31062 0.0 $ G34
tr219 +21.76780 +7.54126 0.0 $ G35
tr220 +23.94458 +3.76936 0.0 $ G36
c
c -----
c Reactor component materials
c -----
c m1 - water
c m2 - aluminum (structural) type 6061
c m3 - stainless steel (structural) type 304
c m4 - graphite (carbon)
c m5 - fresh U-ZrH fuel
c m6 - B4C (boron carbide)
c m7 - zirconium (rod)
c m8 - air
c m10 - cadmium (neutron absorber liner)
c m11 - lead (neutron absorber liner)
c m54 - ar
m1 1001 0.66667
8016 0.33333
mt1 lwtr.60t $294K cme
c mpn1 0 0
m2 13027 -0.9685
26000.50c -0.0070
29000.50c -0.0025
14000.60c -0.0060
12000.66c -0.0110
24000.50c -0.0035
25055 -0.0015
c mpn2 0 0 0 0 0 0
m3 26000.50c -0.6785
6000 -0.0080
14000.60c -0.0100
24000.50c -0.1800
28000.50c -0.0980
25055 -0.0180
15031 -0.0045
16000.66c -0.0030
c mpn3 0 0 0 0 0 0 0
m4 6000 1.0
mt4 grph.60t $ 294K
c mpn4 0
m5 40090.71c -0.462589265
40091.71c -0.100879525
40092.71c -0.154196422
40094.71c -0.156264362
40096.71c -0.025174926
1001.71c -0.0158955
92238.71c -0.068170
92235.71c -0.016830
c mpn5 0 0 82208 82208
mt5 zr/h.62t $600K
h/zr.62t $600K
m6 5010 0.1584
5011 0.6416
6000 0.2
c mpn6 0 0 0
m7 40090 51.45
40091 11.22
40092 17.15
40094 17.38
40096 2.8
c mpn7 0
m8 8016 -0.23
7014 -0.77
c mpn8 0 0
m10 48000.42c 1.0
c mpn10 0
m11 82000.42c -1.0
c mpn11 0
m12 28058 1 $ nickel (n,p) a/o 68.0
m13 28064 1 $ nickel (n,g) a/o 0.9
m14 79197 1 $ gold (n,g) a/o 100.0
m15 29063 1 $ copper (n,g) a/o 69.1
m16 26058 1 $ iron (n,g) a/o 0.2

```

```

m17 26054 1 $ iron (n,p) a/o 5.8
m18 42098 1 $ molybdenum (n,g) a/o 24.1
m19 27059 1 $ cobalt (n,g) a/o 100.0
m20 13027 1 $ aluminum (n,g) a/o 100.0
c m54 18036 0.003365 $cme
c 18038 0.000632
c 18040 0.996003
c 18037 1e-36
c 18039 1e-36
c 18041 1e-36
c 18042 1e-36
c 18043 1e-36
c 17037 1e-36
c 19039 1e-36
c 19041 1e-36
c
c -----
c Tallies
c -----
c
f24:n (1752<u=82)
fc24 Flux tally for CT spectrum
e24 1.000E-11 5.000E-09 1.000E-08 1.500E-08 2.000E-08 2.500E-08
3.000E-08 3.500E-08 4.200E-08 5.000E-08 5.800E-08 6.700E-08
8.000E-08 1.000E-07 1.520E-07 2.510E-07 4.140E-07 6.830E-07
1.125E-06 1.855E-06 3.059E-06 5.040E-06 8.315E-06 1.371E-05
2.260E-05 3.727E-05 6.144E-05 1.013E-04 1.670E-04 2.754E-04
4.540E-04 7.485E-04 1.234E-03 2.035E-03 2.404E-03 2.840E-03
3.355E-03 5.531E-03 9.119E-03 1.503E-02 1.989E-02 2.554E-02
4.087E-02 6.738E-02 1.111E-01 1.832E-01 3.020E-01 3.887E-01
4.979E-01 6.392E-01 8.208E-01 1.108 1.353 1.737
2.231 2.865 3.678 4.965 6.065 10.0
14.91 16.90 20.00 25.00 T
f84:n (455<u=45) $3L tally
fc84 Flux tally for 3L(Pb) spectrum
c fs84 6002 6007 6012 6017 6022 6027 6032 6037 6042 6047 6052 6057
e84 1.000E-11 5.000E-09 1.000E-08 1.500E-08 2.000E-08 2.500E-08
3.000E-08 3.500E-08 4.200E-08 5.000E-08 5.800E-08 6.700E-08
8.000E-08 1.000E-07 1.520E-07 2.510E-07 4.140E-07 6.830E-07
1.125E-06 1.855E-06 3.059E-06 5.040E-06 8.315E-06 1.371E-05
2.260E-05 3.727E-05 6.144E-05 1.013E-04 1.670E-04 2.754E-04
4.540E-04 7.485E-04 1.234E-03 2.035E-03 2.404E-03 2.840E-03
3.355E-03 5.531E-03 9.119E-03 1.503E-02 1.989E-02 2.554E-02
4.087E-02 6.738E-02 1.111E-01 1.832E-01 3.020E-01 3.887E-01
4.979E-01 6.392E-01 8.208E-01 1.108 1.353 1.737
2.231 2.865 3.678 4.965 6.065 10.0
14.91 16.90 20.00 25.00 T
c
f15:n -15.24 -8.8 -22.0 $Point detector at Flux Wire
fc15 Point detector at middle of 3L
e15 1.000E-11 5.000E-09 1.000E-08 1.500E-08 2.000E-08 2.500E-08
3.000E-08 3.500E-08 4.200E-08 5.000E-08 5.800E-08 6.700E-08
8.000E-08 1.000E-07 1.520E-07 2.510E-07 4.140E-07 6.830E-07
1.125E-06 1.855E-06 3.059E-06 5.040E-06 8.315E-06 1.371E-05
2.260E-05 3.727E-05 6.144E-05 1.013E-04 1.670E-04 2.754E-04
4.540E-04 7.485E-04 1.234E-03 2.035E-03 2.404E-03 2.840E-03
3.355E-03 5.531E-03 9.119E-03 1.503E-02 1.989E-02 2.554E-02
4.087E-02 6.738E-02 1.111E-01 1.832E-01 3.020E-01 3.887E-01
4.979E-01 6.392E-01 8.208E-01 1.108 1.353 1.737
2.231 2.865 3.678 4.965 6.065 10.0
14.91 16.90 20.00 25.00 T
c
f25:n -15.24 -8.8 0 2.4 $Ring detector at middle of 3L
fc25 Ring detector at middle of 3L
c e25 1.000E-11 5.000E-09 1.000E-08 1.500E-08 2.000E-08 2.500E-08
3.000E-08 3.500E-08 4.200E-08 5.000E-08 5.800E-08 6.700E-08
8.000E-08 1.000E-07 1.520E-07 2.510E-07 4.140E-07 6.830E-07
1.125E-06 1.855E-06 3.059E-06 5.040E-06 8.315E-06 1.371E-05
2.260E-05 3.727E-05 6.144E-05 1.013E-04 1.670E-04 2.754E-04
4.540E-04 7.485E-04 1.234E-03 2.035E-03 2.404E-03 2.840E-03
3.355E-03 5.531E-03 9.119E-03 1.503E-02 1.989E-02 2.554E-02
4.087E-02 6.738E-02 1.111E-01 1.832E-01 3.020E-01 3.887E-01
4.979E-01 6.392E-01 8.208E-01 1.108 1.353 1.737
2.231 2.865 3.678 4.965 6.065 10.0
14.91 16.90 20.00 25.00 T
c

```

```

c f35:n -15.24 -8.8 -26.19375 0
c fc35 Point Detector at bottom of 3L
c
c f45:n -15.24 -8.8 -19 0
c fc45 Point detector at bottom of fuel in 3L
c
c f55:n -15.24 -8.8 +19 0
c fc55 Point detector at top of fuel in 3L
c
c f65:n -15.24 -8.8 +30.7975 0
c fc65 Point detector at top of 3L
c fl14:n 92
c fc114 Flux tally for RSR
c fs114 6022
c e114 0.50e-6 1.00e-2 1.50e+1 T
c
fl124:n 92
fc124 Flux tally for RSR spectrum
fs124 6022 $ 2nd segment is approx. sample location
e124 1.000E-11 5.000E-09 1.000E-08 1.500E-08 2.000E-08 2.500E-08
3.000E-08 3.500E-08 4.200E-08 5.000E-08 5.800E-08 6.700E-08
8.000E-08 1.000E-07 1.520E-07 2.510E-07 4.140E-07 6.830E-07
1.125E-06 1.855E-06 3.059E-06 5.040E-06 8.315E-06 1.371E-05
2.260E-05 3.727E-05 6.144E-05 1.013E-04 1.670E-04 2.754E-04
4.540E-04 7.485E-04 1.234E-03 2.035E-03 2.404E-03 2.840E-03
3.355E-03 5.531E-03 9.119E-03 1.503E-02 1.989E-02 2.554E-02
4.087E-02 6.738E-02 1.111E-01 1.832E-01 3.020E-01 3.887E-01
4.979E-01 6.392E-01 8.208E-01 1.108 1.353 1.737
2.231 2.865 3.678 4.965 6.065 10.0
14.91 16.90 20.00 25.00 T
c
fl184:n (124<u=8) STRIGA Fuel
fc184 Flux tally for TRIGA Fuel spectrum
e184 1.000E-11 5.000E-09 1.000E-08 1.500E-08 2.000E-08 2.500E-08
3.000E-08 3.500E-08 4.200E-08 5.000E-08 5.800E-08 6.700E-08
8.000E-08 1.000E-07 1.520E-07 2.510E-07 4.140E-07 6.830E-07
1.125E-06 1.855E-06 3.059E-06 5.040E-06 8.315E-06 1.371E-05
2.260E-05 3.727E-05 6.144E-05 1.013E-04 1.670E-04 2.754E-04
4.540E-04 7.485E-04 1.234E-03 2.035E-03 2.404E-03 2.840E-03
3.355E-03 5.531E-03 9.119E-03 1.503E-02 1.989E-02 2.554E-02
4.087E-02 6.738E-02 1.111E-01 1.832E-01 3.020E-01 3.887E-01
4.979E-01 6.392E-01 8.208E-01 1.108 1.353 1.737
2.231 2.865 3.678 4.965 6.065 10.0
14.91 16.90 20.00 25.00 T
c -----
c Criticality calculation
c -----
c 100000 n/cycle, 1.000 as initial guess, skip 30, total of 50 keff cycles,
c automatic plotting of three combined keff tally
c
kcode 1000000 1.000 10 60 4500 0 6500 1
mplot freq 10 kcode 16 scales 2
ksrc -4.5 21.8 13 0 21.8 13 4.5 21.8 13 -11 18 13
-6.5 18.0 13 -2 18.0 13 2.0 18 13 6.5 18 13
11 18 13 -17.5 14.3 13 -13 14.3 13 -9 14.3 13
-4.5 14.3 13 0 14.3 13 4.5 14.3 13 9 14.3 13
13 14.3 13 -19.5 10.5 13 -15.5 10.5 13 -11 10.5 13
-6.5 10.5 13 2 10.5 13 6.5 10.5 13 11 10.5 13
15.5 10.5 13 19.5 10.5 13 -22 6.8 13 -17.5 6.8 13
-13 6.8 13 -9 6.8 13 -4.5 6.8 13 0 6.8 13
4.5 6.8 13 9 6.8 13 13 6.8 13 17.5 6.8 13
-19.5 2.8 13 -15.5 2.8 13 -11 2.8 13 -6.5 2.8 13
-2 2.8 13 2 2.8 13 6.5 2.8 13 11 2.8 13
15.5 2.8 13 19.5 2.8 13 -22 -0.8 13 -17.5 -0.8 13
-13 -0.8 13 -4.5 -0.8 13 4.5 -0.8 13 13 -0.8 13
17.5 -0.8 13 22 -0.8 13 -24 -4.6 13 -19.5 -4.6 13
-15.5 -4.6 13 -11 -4.6 13 -6.5 -4.6 13 -2 -4.6 13
2 -4.6 13 6.5 -4.6 13 11 -4.6 13 15.5 -4.6 13
19.5 -4.6 13 -22 -8.3 13 -9 -8.3 13 -4.5 -8.3 13
0 -8.3 13 4.5 -8.3 13 9 -8.3 13 13 -8.3 13
17.5 -8.3 13 22 -8.3 13 -11 -12 13 -6.5 -12 13
2 -12 13 6.5 -12 13 11 -12 13 15.5 -12 13
19.5 -12 13 -17.5 -15.9 13 -13 -15.9 13 -9 -15.9 13
-4.5 -15.9 13 0 -15.9 13 4.5 -15.9 13 9 -15.9 13
13 -15.9 13 17.5 -15.9 13 -15.5 -19.7 13 -11 -19.7 13
-6.5 -19.7 13 -2 -19.7 13 2 -19.7 13 6.5 -19.7 13

```

```
11 -19.7 13 -4.5 -23.5 13 0 -23.5 13 4.5 -23.5 13
thtme 0 $ time in shakes (1e-8 sec) at which thermal temperatures...
mode n p
phys:p 100 0 0 0 1 -102 $ -102, Analog sampling, models only, multigroup + line emission
imp:n 1 311r 0
imp:p 1 311r 0
print
```

## REFERENCES

- C.E. Aalseth, A.R. Day, D.A. Haas, E.W. Hoppe, B.J. Hyronimus, M.E. Keillor, E.K. Mace, J.L. Orrell, A. Seifert, V.T. Woods. (2011) "Measurement of  $^{37}\text{Ar}$  to support technology for On-site Inspection under the Comprehensive Nuclear-Test-Ban Treaty," Nuclear Instruments and Methods in Physics Research Section A 652 (1): 58-61.
- D.N. Abdurashitov, E.P. Veretenkin, V.N. Gavrin, V.V. Gorbachev, T.V. Ibragimova, A.V. Kalikhov, I.N. Mirmov, A.A. Shikhim, V.E. Yants, V.I. Barsanov, A.A. Dzhanelidze, S.B. Zlokazov, S.Yu. Markov, Z.N. Shakirov, B.T. Cleveland, (2007) "Measurement of the Activity of an Artificial Neutrino Source Based on  $^{37}\text{Ar}$ ," Physics of Atomic Nuclei 70 (2): 311-318.
- J.N. Abdurashitov, V.N. Gavrin, I.N. Mirmov, E.P. Veretenkin, V.E. Yants, N.N. Oshkanov, A.I. Karpenko, V.V. Maltsev, V.I. Barsanov, K.S. Trubin, S.B. Zlokazov, Yu.S. Khomyakov, V.M. Poplavsky, T.O. Saraeva, B.A. Vasiliev, O.V. Mishin, T.J. Bowles, W.A. Teasdale, K. Lande, P. Wildenhain, B.T. Cleveland, S.R. Elliott, W. Haxton, J.F. Wilkerson, Z. Suzuki, Y. Suzuki, M. Nakahata. (2002) Nuclear Physics B 110: 326-328.
- V.I. Barsanov, A.A. Dzhanelidze, S.B. Zlokazov, N.A. Kotelnikov, S. Yu. Markov, V.V. Selin, Z.N. Shakirov, D.N. Abdurashitov, E.P. Veretenkin, V.N. Gavrin, V.V. Gorbachev, T.V. Ibragimova, A.V. Kalikhov, I.N. Mirmov, A.A. Shikhim, V.E. Yants, Yu.S. Klomyakov, B.T. Cleveland. (2007) "Artificial Neutrino Source Based on the  $^{37}\text{Ar}$  Isotope," Physics of Atomic Nuclei 70 (2): 300-310.
- J.D. Braisted. (2008) "Design and characterization of an irradiation facility with real-time monitoring," Ph.D. Dissertation, The University of Texas at Austin.
- T.W. Bowyer, C. Schlosser, K.H. Abel, M. Auer, J.C. Hayes, T.R. Heimbigner, J.I. McIntyre, M.E. Panisko, P.L. Reeder, H. Satorius, J. Schulze, W. Weiss. (2002) "Detection and analysis of xenon isotopes for the comprehensive nuclear-test-ban treaty international monitoring system," Journal of Environmental Radioactivity, 59(2): 139-151.
- C. Carrigan, "Using OSI [On-Site Inspection] Field Studies and Tests to Define Noble Gas Sampling and Analysis Requirements," (2009) International Noble Gas Experiment Conference, Daejeon, Korea, November 9-14, LLNL-PRES-41961.
- C.R. Carrigan, Y. Sun, "Issues Involving The OSI Concept of Operation for Noble Gas Radionuclide Detection," (2011) LLNL-TR-467731.
- M. Chadwick, P. Oblozinsky, M. Herman, N. Greene, R. McKnight, D. Smith, P. Young, R. MacFarlane, G. Hale, S. Frankle. (2006) "ENDF/B-VII.0: Next Generation Evaluated

Nuclear Data Library for Nuclear Science and Technology,” Nuclear Data Sheets, 107 (12): 2931-3060.

M.B. Chadwick, M. Herman, P. Oblozinsky, M.E. Dunn, Y. Danon, A.C. Kahler, D.L. Smith, B. Pritychenko, G. Arbanas, R. Arcilla, R. Brewer, D.A. Brown, R. Capote, A.D. Carlson, Y.S. Cho, H. Derrien, K. Guber, G.M. Hale, S. Hoblit, S. Holloway, T.D. Johnson, T. Kawano, B.C. Kiedrowski, H. Kim, S. Kunieda, N.M. Larson, L. Leal, J.P. Lestone, R.C. Little, E.A. McCutchan, R.E. MacFarlane, M. MacInnes, C.M. Mattoon, R.D. McKnight, S.F. Mughabghab, G.P.A. Nobre, G. Palmiotti, A. Palumbo, M.T. Pigni, V.G. Pronyaev, R.O. Sayer, A.A. Sonzogni, N.C. Summers, P. Talou, I.J. Thompson, A. Trkov, R.L. Vogt, S.C. van der Marck, A. Wallner, M.C. White, D. Wiarda, P.G. Young. (2011) “ENDF/B-VII.1 Nuclear Data for Science and Technology: Cross Sections, Covariances, Fission Product Yields and Decay Data,” Nuclear Data Sheets, 112 (12): 2887-2996.

“Comprehensive Nuclear Test-Ban-Treaty” (1996) United Nations General Assembly resolution number 50/245, UN. New York, USA.

L. Currie. (1968) “Limits for Qualitative Detection and Quantitative Determination,” Anal. Chem. 40: 586-593.

R.R. Draxler, G.D. Rolph. (2012) HYSPLIT (HYbrid Single-Particle Lagrangian Integrated Trajectory) Model access via NOAA ARL Ready website. <http://ready.arl.noaa.gov/HYSPLIT.php>. NOAA Air Resources Laboratory, Silver Spring, MD.

J.J. Duderstadt, L.J. Hamilton. (1976) Nuclear Reactor Analysis. John Wiley & Sons, New York.

C.M. Egnatuk, J. Lowrey, S.R. Biegalski, T. Bowyer, D. Haas, J. Orrell, V. Woods, M. Keillor. (2012) “Production of  $^{37}\text{Ar}$  in The University of Texas TRIGA reactor facility,” Journal of Radioanalytical and Nuclear Chemistry, 291: 257-260.

A.G. Fay, S.R. Biegalski. (2012) “Contributions to the  $^{37}\text{Ar}$  Background by Research Reactor Operations,” Journal of Radioanalytical and Nuclear Chemistry, in press.

V.A. Fokin. (2000) “Calculation of the size of the blast cavity by underground nuclear explosions,” Atomic Energy, 59: 924-927.

J.A. Formaggio, E. Figueroa-Feliciano, A.J. Anderson (2012) “Sterile neutrinos, coherent scattering, and oscillometry measurements with low-temperature bolometers,” Physical Review D, Vol 85 (1).

- V. Frank, J. Tolgyessy. (1993) "The Chemistry of Soil," Tolgyessy, J. (Ed), Chemistry and Biology of Water, Air and Soil Environmental Aspects. Elsevier, Amsterdam.
- D.A. Haas, S.R. Biegalski, K.M. Foltz Biegalski. (2009) "Radioxenon production through neutron irradiation of stable xenon gas," Journal of Radioanalytical and Nuclear Chemistry, 282 (3) 677-680.
- D. A. Haas, H.S. Miley, J.L. Orrell, C.E. Aalseth, T.W. Bowyer, J.C. Hayes, J.I. McIntyre. (2010) "The Science Case for  $^{37}\text{Ar}$  as a Monitor for Underground Nuclear Explosions," PNNL Document PNNL-19458.
- A. Koning, R. Forrest, M. Kellett, R. Mills, H. Henriksson, Y. Rugama. (2006) "The JEFF-3.1 Nuclear Data Library," Nuclear Energy Agency, Organisation for Economic Co-operation and Development.
- J.D. Lowrey. (2010) "Production and Subsurface Vertical Transport of Radioxenon resulting from Underground Nuclear Explosions," Master's Thesis, The University of Texas at Austin.
- C. Merrihue. (1965) "Trace element determinations and potassium-argon dating by mass spectroscopy of neutron-irradiated samples," Transactions of the American Geophysical Union, V. 46, no. 1.
- H. Michael, R. Wolfe, S.M. Qaim, (1984) "Production of  $^{37}\text{Ar}$ ," The International Journal of Applied Radiation and Isotopes. 35(8) 813-815.
- S.F. Mughabghab, M. Divadeenam, N.E. Holden. (1981) Neutron Cross Sections, Vol. 1, Neutron Resonance Parameters and Thermal Cross Sections, Part A, Z+1-60, Academic Press, New York.
- Purtschert, R, R. Reidmann, (2011) "Argon 37: What is the suspicious threshold activity in soil air?" Comprehensive Nuclear-Test-Ban Treaty: Science and Technology, Vienna, Austria 8-9 June.
- K.J.R. Rosman and P.D.P. Taylor. (1998) "Isotopic Composition of the Elements 1997," Pure Applied Chemistry. 70: 217-235.
- A. Santamarina, D. Bernard, P. Blaise, M. Coste, A. Courcelle, T.D. Huynh, C. Jouanne, P. Leconte, O. Litaize, S. Mengelle, G. Noguere, J-M. Ruggieri, O. Serot, J. Tommasi, C. Vaglio, J-F. Vidal. (2009) "The JEFF-3.1.1 Nuclear Data Library: JEFF report 22: Validation Results from JEF-2.2 to JEFF-3.1.1," Nuclear Energy Agency, Organization for Economic Co-operation and Development.

K. Shibata, T. Kawano, T. Nakagawa, O. Iwamoto, J. Katakura, T. Fukahori, S. Chiba, A. Hasegawa, T. Murata, H. Matsunobu, T. Ohsawa, Y. Nakajima. (2002) "Japanese Evaluated Nuclear Data Library Version 3 Revision 3: JENDL-3.3" *Journal of Nuclear Science and Technology*, 39 (11): 1125-1136.

K. Shibata, O. Iwamoto, T. Nakagawa, N. Iwamoto, A. Ichihara, S. Kunieda, S. Chiba, K. Furutaka, N. Otuka, T. Ohasawa, T. Murata, H. Matsunobu, A. Zukeran, S. Kamada, J. Katakura. (2011) "JENDL-4.0: A New Library for Nuclear Science and Engineering," *Journal of Nuclear Science and Technology*, 48 (1) 1-30.

T. Sigurgeirsson. (1962) "Dating basalt by the potassium-argon method," Report of Physical Laboratory of the University of Iceland.

U. Stoeckler, M. Nikkinen, A. Gheddou. (2011) "Detection of Radionuclides emitted during the Fukushima Nuclear Accident with the CTBT Radionuclide Network," 2011 Monitoring Research Review: Ground-Based Nuclear Explosion Monitoring Technologies, Tucson, Arizona, 13-15 September.

W.M. Stacey. (2001) "Nuclear Reactor Physics," John Wiley & Sons.

H.R. Trellue. (1998) "Development of MonteBurns: A Code That Links MCNPS and ORIGEN2 in an Automated Fashion for Burnup Calculations," Los Alamos National Laboratory document LA-T-13514.

R.M. Ward, S.R.F. Biegalski, D.A. Haas, W. Hennig. (2009) "Comparison of phoswich and ARSA-type detectors for radioxenon measurements," *Journal of Radioanalytical and Nuclear Chemistry*. 282 (3): 693-697.

K.H. Wedepohl, "Handbook of Geochemistry," Springer, Berlin, Heidelberg, NY, Springer, 1969-1978.

L. Wielopolski, Z. Song, I. Orion, A. L. Hanson, G. Hendrey. (2004) "Basic considerations for Monte Carlo calculations in soil," *Applied Radiation and Isotopes* 62: 97-107.

"WISE Uranium Project," (2011) World Information Service on Energy. <http://www.wise-uranium.org/>. Accessed: August 2011.

S.V. Zabrodskaia, A.V. Ignatyuk, V.N. Koscheev, V.N. Manokhin, M.N. Nikolaev, V.G. Pronyaev. (2007) "ROSFOND—Russian National Library of Neutron Data," VANT, Nuclear Constants 1-2 3.

## VITA

Christine Egnatuk graduated in May 2003 with a Bachelor of Arts degree with a double major in mathematical science and physics from The College of Wooster in Wooster, Ohio. She worked under Dr. Jon-Kar Zubieta at the Molecular and Behavioral Neuroscience Research Institute at The University of Michigan.

Egnatuk is a DOE/NNSA Nuclear Nonproliferation and International Safeguards Fellow and Ph.D. candidate in the Nuclear and Radiation Engineering Program at The University of Texas at Austin. She was previously an Alternate Sponsored Fellow conducting research within the Radioanalytical Chemistry Division at Pacific Northwest National Laboratory. Egnatuk was an NGSi summer intern at Oak Ridge National Laboratory in 2010. She was a member of an interdisciplinary group within the Lyndon B. Johnson School of Public Affairs, which investigated the global minimization of highly enriched uranium. Her work examined the feasibility of using the proposed floating nuclear power plant reactor core design within the Russia Nuclear Icebreaker Fleet. Egnatuk also participated in the Nuclear Scholars Initiative through the Center for Strategic and International Studies during 2012.

Permanent address (or email): [cegnatuk@gmail.com](mailto:cegnatuk@gmail.com)

This dissertation was typed by Christine M. Egnatuk.